Growth-induced self-organization in bacterial colonies

You, Z.

Growth-Induced Self-Organization in Bacterial Colonies

Proefschrift

ter verkrijging van
de graad van Doctor aan de Universiteit Leiden,
op gezag van Rector Magnificus prof. mr. C.J.J.M. Stolker,
volgens besluit van het College voor Promoties
te verdedigen op dinsdag 25 juni 2019
klokke 16.15 uur

door

Zhihong You

geboren te Zhangzhou (Fujian), China
in 1989

Promotor:	Prof. dr. H. Schiessel
Co-promotor:	Dr. L. Giomi
Promotiecommissie:	Dr. A. Sengupta (University of Luxembourg)
	Prof. dr. V. Vitelli (University of Chicago)
	Prof. dr. E.R. Eliel
	Dr. D.J. Kraft
	Prof. dr. ir. W. van Saarloos
	Prof. dr. T. Schmidt

Casimir PhD series, Delft-Leiden 2019-18
ISBN 978-90-8593-404-2
An electronic version of this thesis can be found at
https://openaccess.leidenuniv.nl

This work was conducted at the Lorentz Institute, Leiden University. The author was supported by funding from The Netherlands Organization for Scientific Research (NWO/OCW) as part of the Frontiers of Nanoscience program.

The cover shows a growing bacterial colony seeded from a single bacterium as an expanding universe. The number of cells are, from left to right: 2^1, 2^3, 2^5, 2^7, 2^9, and 2^{11}. Cells are color-coded by their orientations. The white lines indicate the exponential expansion of the periphery of the colony.

To My Family and Archimedes

Contents

Chapter 1

Introductions

1.1 Mechanics of cellular systems

Ever since the genius speculations of Erwin Schrödinger on the physical nature of living systems and living processes, including heredity, consciousness, and how living matter evades the decay to thermodynamical equilibrium, in his famous book *What is life* [1], physics has been closely entangled with biological systems. On the one hand, successful applications of physics have greatly advanced our understanding of a plethora of biological phenomena spanning various scales: from the dynamics of protein folding [2, 3] to the mechanics of cell membranes [4, 5], to the collective behavior of animal groups [6–9]. In addition to these, the exciting development of electronic and optical imaging technologies makes it possible to observe and study biological systems at high spatial and temporal resolutions, based on which quantitative relations can be built. Typical examples include the first discovery of DNA's double-helix structure with X-ray radiation by Francis Crick and James Watson in 1953 [10], and the state-of-the-art scanning electron cryomicroscopy that can produce extremely high magnification images (up to 1000000×) with sub-nanometer resolution [11]. On the other hand, the inherent complexity of biological systems makes them excellent platforms for physicists to learn new physics, and expand our knowledge of nature from both the physical and biological perspectives in an integrated way.

In the last few decades, special emphasis has been placed on the mechanics of cellular systems, which exhibit a variety of fascinating phenomena that are interesting to physicists, biologists, and engineers. These studies usually lead to new understanding of the role of mechanics in biological processes [4, 5, 14–18], the discovery of amazing material properties, or extensions of physical laws to living systems [19–23]. Excellent examples are:

- Cell differentiation pathways, usually believed to be a pure biochem-

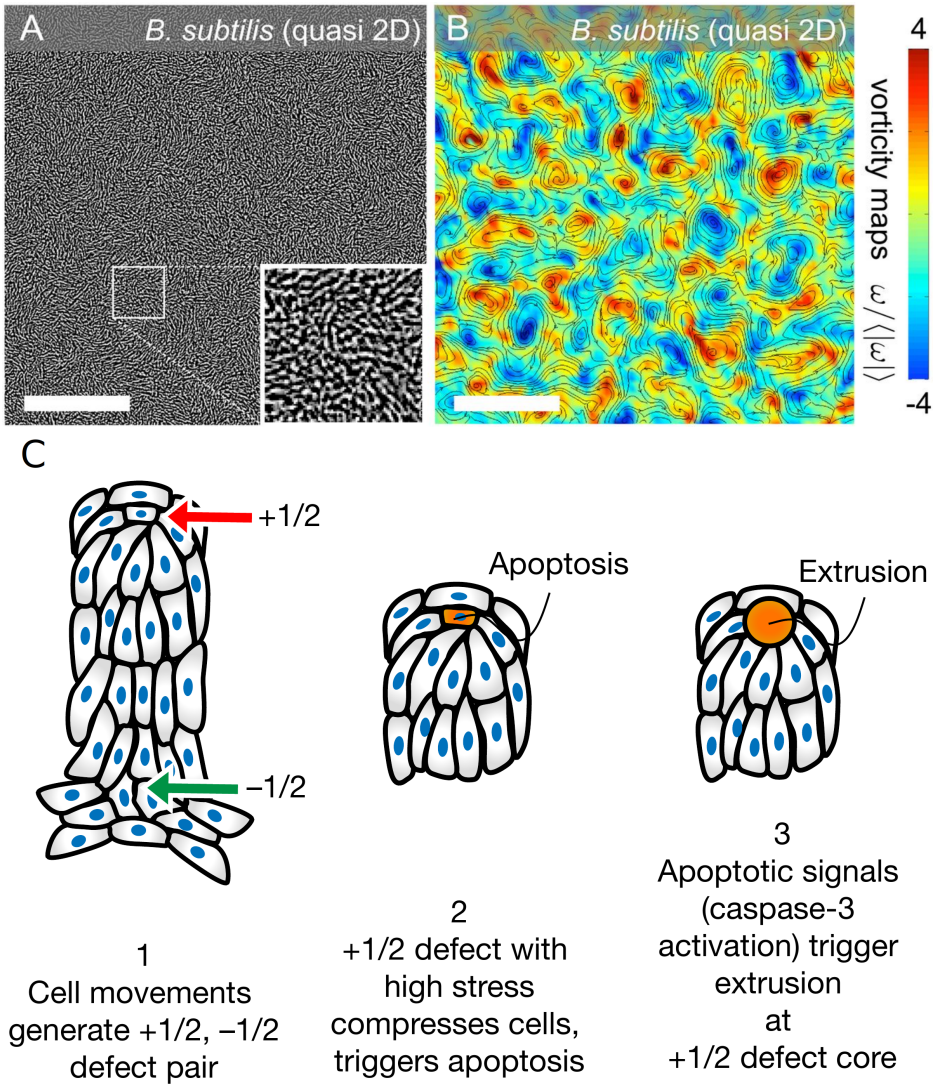

Figure 1.1. Recent discoveries on the mechanics of cellular systems. (A-B) Turbulent flow of bacterial suspension at low Reynolds numbers, adapted from [12]. (A) Experimental snapshot of a highly concentrated, homogeneous quasi-2D bacterial suspension. (B) Flow streamlines v and vorticity fields ω in the turbulent regime (Scale bars, 50 μm). (C) Topological defects in cell orientation can focus mechanics stresses and trigger cell apoptosis and extrusion, adapted from [13].

ical process, can be regulated by mechanical forces [24, 25];

- A suspension of swimming bacteria can effectively reduce the viscosity of the fluid, and can even turn it into a "superfluid" [26];
- Active turbulence: turbulent flow at low Reynolds numbers [12, 27–30] (Figs. 1.1A-B);
- Topological defects of cell orientation in epithelia govern cell death and extrusion [13] (Figs. 1.1C);
- Liquid-solid transition of tissue monolayer, controlled by cell motility and mechanical interactions among cells [31, 32], and fluidization of tissues by cell division and apoptosis [33];
- Motility induced phase separation [34–36].

Despite presenting enormous differences in terms of length and time scales, mechanical interactions, and biological nature, these intriguing phenomena in cellular systems can ultimately be ascribed to a few underlying properties. First of all, unlike normal material, the building blocks of cellular systems usually have complex structures or high internal degrees of freedom [5, 14]. In addition, the interactions among building blocks can be highly complex, involving specific mechanical interactions or cell-cell communications [5, 14, 37], which, collectively, can lead to the emergence of biological functionality. Second, cellular systems are usually heterogeneous (in space) and anisotropic [7, 19, 38]. Heterogeneity and anisotropy can be inherent to the building blocks (their shapes or mechanical interactions), but they can also be triggered by external stimuli. Both properties indicate the breaking of certain symmetry, hence can give rise to nontrivial spatial patterns or anisotropic material properties. Last but not least, cellular systems are living systems, which means that they can actively organize themselves to fulfill certain biological functions or respond to mechanical or biochemical cues. The activity enables the system to harvest energy locally and transfer it into motion or specific mechanical forces, which is fundamentally different from classical nonequilibrium systems where the energy injection is at the macroscopic scale and at the boundary of the system [6, 7]. These properties, individually or collectively, can promote different types of functions or material properties that ultimately distinguish cellular systems from the nonliving world.

These considerations raise a question of special physical interest: what are the general principles that govern the mechanics of cells at different

scales? Or in other words, how certain microscopic dynamics or mechanical interactions can give rise to specific macroscopic mechanical properties? In the past few decades, much has been done to address this question, theoretically and experimentally. Especially, the expanding community of *active matter* has made an enormous effort to connect the microscopic properties, e.g. particle shape or activity like self-propulsion, to macroscopic material properties such as rheology and mechanical stresses [6, 7, 19–23, 39–42]. These advances are very exciting and promising, but there's still a long way to go on the mechanics of biological systems. The research work presented in this thesis is motivated by the same general question and is devoted, specifically, to the problem of growth-induced self-organization in bacterial colonies.

1.2 Mechanics driven self-organization in bacterial colonies

Bacteria successfully colonize a plethora of surfaces by producing hydrated extracellular polymeric matrix, generally composed of proteins, exopolysaccharides and extracellular DNA (Fig. 1.2) [43–47]. The extracel-

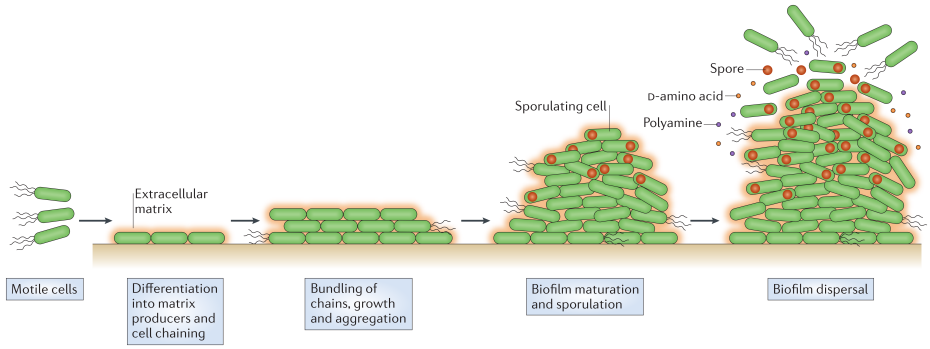

Figure 1.2. The formation of a biofilm occurs in several stages, comprising the development, maturation and disassembly of the bacterial community. At the initiation of biofilm formation, motile cells with flagella differentiate into non-motile, matrix-producing cells that stop separating and form chains that are surrounded by extracellular matrix. In mature biofilms, matrix-producing cells sporulate. In aged biofilms, some cells secrete small molecules such as D-amino acids and polyamines, which break down the extracellular matrix and allow the cells to disperse in the environment. Adapted from [43].

lular matrix (ECM), together with the bacterial cells, forms a slime layer of organism that is usually referred to as *biofilm*. A biofilm is more than a collection of ECM and cells, but a functional ecosystem that can grow, adapt, and actively respond to external stimuli [44–46]. Such surface-associated communities play a crucial role in the pathogenesis of many chronic infections–from benign dental caries in the oral cavity [48, 49] to life-threatening cystic fibrosis and catheter-related endocarditis [50]. For planktonic species (i.e., freely swimming), the life of a biofilm starts with cells undergoing a phenotypic shift whereby motile cells turn sessile (i.e. surface-associated), and thereafter continues growing in size via the formation of an exponentially growing monolayer of tightly packed and partially aligned cells (Fig. 1.2) [43, 51–55]. Colonies originating from a single bacterium initially develop as a flat monolayer and, upon reaching a critical population, invade the third dimension forming multiple layers [43, 51, 56]. After this, the multilayered structure becomes thicker, and the colony undergoes a transition from a planar sheet to a bulk material. As the biofilm becomes mature, some cells at the surface experience a reversed phenotypic shift, become motile again and start to initiate a new cycle.

In contrast to planktonic populations of motile cells (freely swimming, gliding, or swarming), cells in a sessile colony lack motility. Since most bacteria found in nature exist predominantly as surface-associated colonies [57], they are permanently exposed to a range of surface-specific forces [54]: time-varying internal stress due to growth, contact forces due to interactions with the neighboring cells and substrate they are growing on, or shear stresses due to ambient flows in the system. Our understanding of the mechanics of bacterial growth is still in its infancy, specifically in light of the wide range of mechanical cues that single cells overcome to successfully colonize surfaces. Although it has been long known that mechanical forces play a critical role in the development and fitness of eukaryotic cells and, in addition, can regulate key molecular pathways [58], the cornerstones of major discoveries in bacterial communities have relied on biochemical pathways triggered exclusively by chemical stimuli [52]. Only recently has the role of mechanics in the ecophysiology of prokaryotic cells come to the forefront [38, 51, 53–56, 59–62], highlighting the governing biophysical principles that drive colony formation.

A particularly interesting demonstration of the mechanical aspects of bacterial organization was illustrated in Refs. [38, 55, 59, 60], upon con-

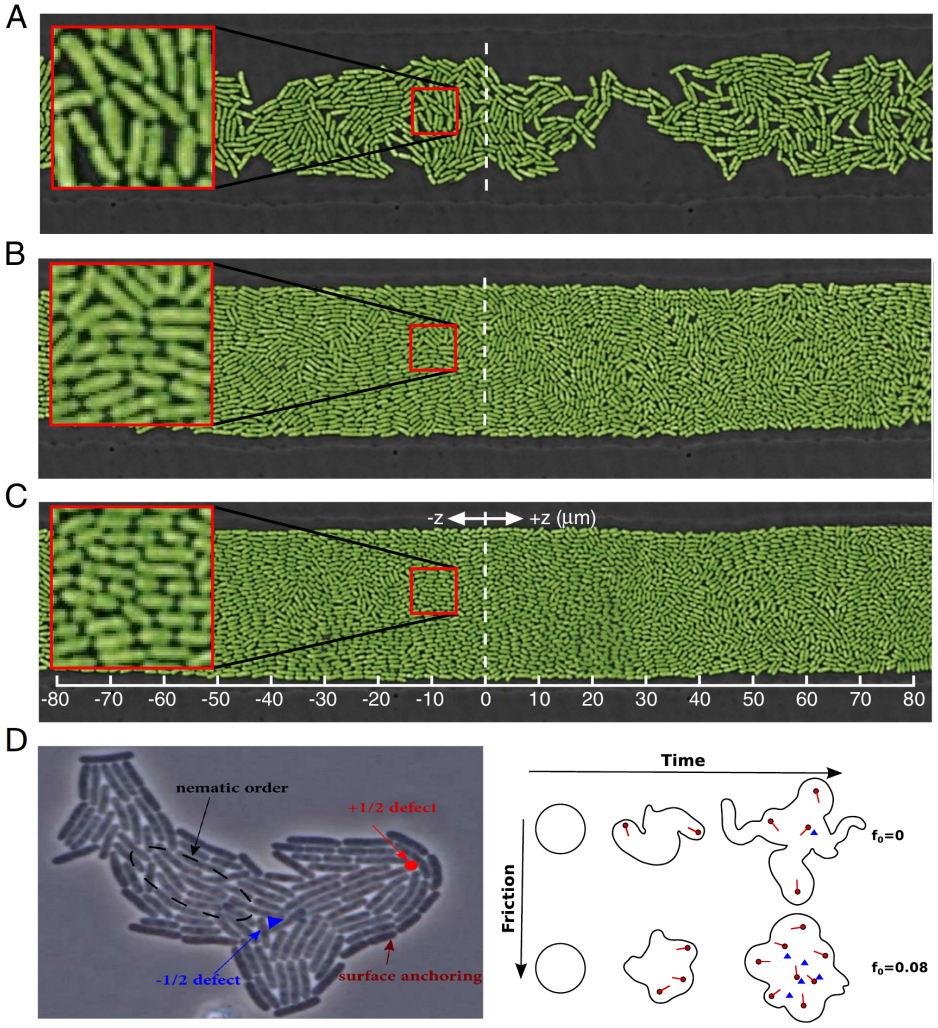

Figure 1.3. (A-C) Snapshots of a growing bacterial colony confined in a microfluidic channel at (A) 60, (B) 90, and (C) 138 minutes from the beginning of the experiment. Adapted from [38]. (D) A growing *E. coli* colony shows nematic ordering, $\pm 1/2$ topological defects, and tangential alignment to the interface (left). (Right) The spatiotemporal evolution of a growing colony is affected by the dynamics of topological defects and by friction with the substrate. With increasing friction, the defect density increases and the average defect velocity drops, resulting in a more isotropic morphology. Adapted from [63].

fining a monolayer of nonmotile duplicating bacteria in a microchannel. Depending on the channel length, the bacterial population was observed to evolve either into a highly ordered colony [38, 55, 60], with all the cells parallel to each other and to the channel wall (Figs. 1.3A-C), or, for longer channels, into disordered structures consisting of multiple domains of aligned cells with no global order [59]. A strikingly similar behavior was identified by Wioland *et al.* in suspensions of swimming bacteria [64]. Theoretical study also revealed that in a monolayered colony without boundary confinement, topological defects in the orientation of cells were created, which were found to regulate the morphological development of the colony (Fig. 1.3D) [63]. The friction between the dividing cells and underlying substrate drives anisotropic colony shapes toward more isotropic morphologies, by mediating the number density and the velocity of topological defects. Indeed, a recent experiment found that increasing the adhesion, i.e. the "effective friction", between cells and the substrate resulted in a more circular colony shape, although it was not clear whether or not this was triggered by the creation of topological defects [65]. In addition, the mechanical interactions among neighboring cells were also found to be responsible for the mono-to-multilayer transition in bacterial colonies, by competing with the vertical restoring forces from the ECM or from the agarose gel on top [56, 65, 66]. More recently, the development of new imaging techniques makes it possible to inspect the internal structure of a three-dimensional growing colony down to the scale of individual bacterium [67, 68]. Compared to the 2D counterparts, the 3D colonies show much richer organizations, in terms of local cellular order and the global biofilm architecture, as a consequence of the intricate mechanical interactions among cells and between cells and the substrate/ECM [67, 68].

When coupled with other factors, mechanical interactions can promote many other interesting phenomena. For example, cell-cell repulsive forces can account for the nonequilibrium transition from circular to branching colonies often observed in the lab (Figs. 1.4A-B), upon tuning the intake of nutrient from the substrate [62]. More interestingly, mechanical interactions can also affect the biological evolution by regulating the relative motion of cells in the colony [69]. Specifically, a mutation arising at the colony's frontier can either die out and extinct, or survive and persist, and the probability distributions of the two fates are determined by the mechanical properties of the system, such as the cell aspect ratio, the cell

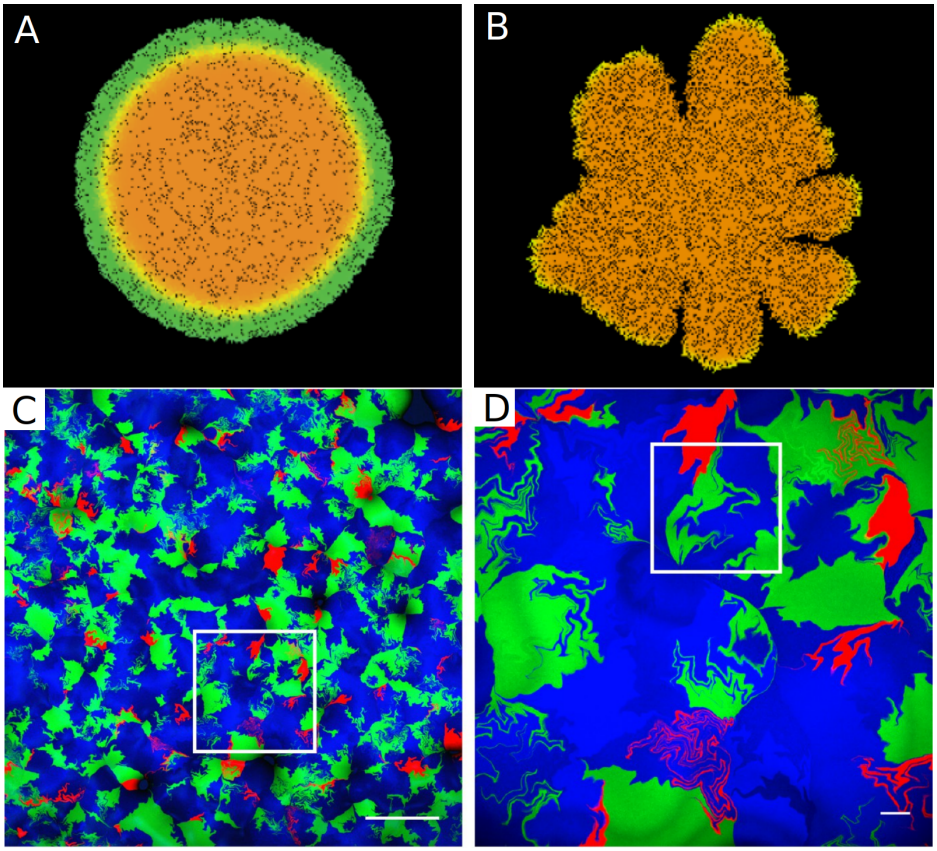

Figure 1.4. (A-B) Snapshots of growing bacterial colonies from the simulation of $N \sim 10^5$ cells, showing the mechanics-driven circular-to-branching transition. Panels (A) and (B) have, respectively, low and high values of branching parameter β, which depends on cell growth rate, the initial concentration of nutrient, and the consumption rate of nutrient. The green (orange) color corresponds to a high (low) local nutrient concentration. Adapted from [62]. (C-D) Fractal patterns in growing multi-species bacterial colonies. Different species are labeled with three different fluorescent proteins: mTurquoise2 (in blue), mRFP1 (in red) and sfGFP (in green). Scale bars, 1 mm in (C), 100 μm in (D). Adapted from [53].

orientation, and the friction from the substrate [69]. Moreover, in the case of multi-species biofilm, the buckling instability at the interface of different species can trigger the formation of striking fractal patterns with jagged, self-similar shapes (Figs. 1.4C-D) [53].

These works have greatly advanced our understanding of how mechanical interactions can drive diverse types of self-organizations in growing bacterial colonies. However, a general understanding of the underlying physics that govern different stages of the colonization process is still lacking. Specifically: what mechanical effects play a dominant role in the system dynamics? How to characterize them using the language of physics? And how do they originate from the microscopic dynamics of bacterial cells? Among these, a key problem is to understand the mechanical effects of cell growth. This is particularly important because of three reasons. First of all, a good knowledge of the role of cell growth is crucial to our comprehension of the morphological developments of growing cellular systems such as tissues or microbial colonies. Second, previous studies have shown that the activity of cells, e.g. self-propulsion or active alignment, can give rise to very specific mechanical properties at the macroscopic scale [6, 7, 19, 41]. Conversely, the effects of cell growth on the macroscopic organization of a bacterial colony have not been investigated with an equally systematic approach. Third, in sessile bacterial colonies, cell growth is the ultimate driving force of cell motion and colony expansion. Without cell growth, the frictional and adhesive forces from the substrate will quickly damp any cell motion and leave the system in a stationary state. It is thus important to understand how various mechanical interactions can arise as a consequence of cell growth.

In this thesis, we address these problems theoretically, with computer

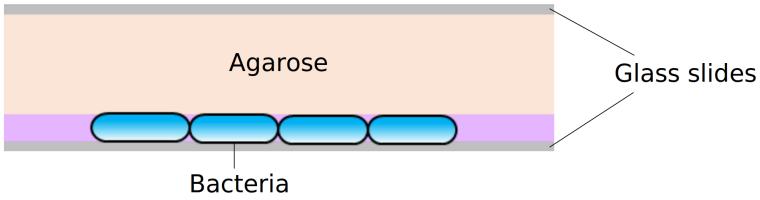

Figure 1.5. Sketch of the model system we used in the thesis. A growing colony of non-motile, rod-shaped bacteria is sandwiched between a hard glass slide and a relatively soft agarose gel. Cells take up nutrient from the agarose, and then grow, divide, and push each other away as they elongate.

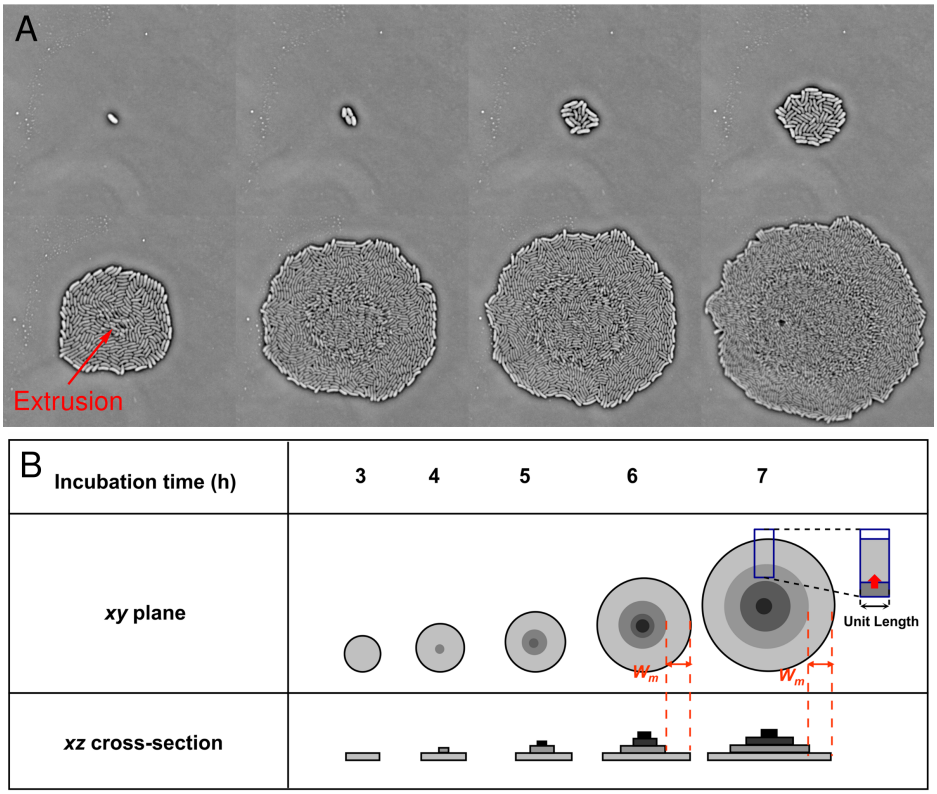

Figure 1.6. (A) Snapshots at different time points of a growing bacterial colony sandwiched between an agarose gel and a glass slide. Monolayer expansion was found at the initial stage (top images). At certain colony size, a second layer was formed through cell extrusion at the center of the colony (bottom, left), and then both layers expanded simultaneously. Images provided by Anupam Sengupta. (B) Illustration of a micro-colony development by viewing at different planes. Even though the diameter and layers of the bacterial micro-colony were increasingly expanding, the average width of the outermost monolayer reached a constant value after approximately 6 h of growth. The red arrow indicates the constant outward force per unit length. Adapted from [61].

simulations of discrete and continuum models. We use a rather simple model system that has been frequently used to study growing bacterial colonies [56, 61, 65], where a growing colony of nonmotile rod-shaped bacteria is sandwiched between a glass slide and an agarose gel (Fig. 1.5). Cells take up nutrient from the agarose and then grow and divide. In such a setup, cell motion can be instantaneously damped by frictional and adhesive forces, due to the interaction with the glass and the agarose gel [56, 65]. Nevertheless, the elongation of cells enables them to persistently push away their neighbors along their axes. These mutually pushing forces between neighboring cells can then help them overcome the damping forces, and drive continuous motion of cells in the whole colony. In addition, since the agarose on top is relatively soft compared to the glass side, cells are allowed to deform the agarose gel, at a cost of certain elastic energy. For this reason, the colony expands as a monolayer first (Fig. 1.6). Then, upon reaching a certain colony size, the in-plane stress can induce normal lifting forces to cells that outweigh the agarose compression, squeezing them out of the monolayer, and initiate the second layer of the colony (Fig. 1.6) [56, 61]. After this, more and more cells are transported from the first to the second layer, but at the same time, cells on the second layers are also growing and duplicating. This expanding second layer can then initiate the third layer, and subsequently more and more layers (Fig. 1.6) [61]. There are many interesting phenomena that we can dig into during this process, including the dynamics of the monolayer expansion, the mono-to-multilayer transition, and the dynamics of the mulitlayer expansion, where adjacent layers actively interact with each other through mechanical forces and mass transfer. Here in this thesis, we are interested in the initial stages, more specifically the monolayer expansion and the mono-to-multilayer transition. We focus on the mechanical effects of cell growth, and how their competition/collaboration with other mechanical interactions can give rise to self-organizations at different stages of the biofilm formation.

1.3 Outline of the thesis

Before discussing the main results, in chapter 2, we introduce the discrete and continuum models we used to characterize growing bacterial colonies. To perform "experiments" of growing bacteria *in silico*, we employ a molecular dynamics model of elongating hard rods. From the dis-

crete model, we are able to identify the self-organized patterns of growing bacterial colonies, and measure the mechanical properties of the system, which can not be easily done in experiments. In addition, in order to understand intuitively the results from our molecular dynamics simulations and gain further insights, we also describe our growing colony in the realm of continuum mechanics, more specifically the continuum theory of active nematics, with suitable extensions that are specific to the growing bacterial colonies.

With the models at hand, in chapter 3, we discuss the geometrical and mechanical properties of a freely expanding monolayer. We demonstrate that such an expanding colony self-organizes into a "mosaic" of microdomains consisting of highly aligned cells. The emergence of microdomains is mediated by two competing forces: the steric forces between neighboring cells, which favor cell alignment, and the extensile stresses due to cell growth that tend to reduce the local orientational order and thereby distort the system. This interplay results in an exponential distribution of the domain areas and sets a characteristic length scale proportional to the square root of the ratio between the system orientational stiffness and the magnitude of the extensile active stress. Based on these results, we develop a continuum theory for growing bacterial colonies by suitably extending the hydrodynamic equations of active nematics, and the simulations show the same qualitative results as we found in the discrete model. Our theoretical predictions are finally compared with experiments with freely growing *E. coli* micro-colonies, finding quantitative agreement.

In chapter 4, we study the self-organization of growing monolayer under lateral confinement. Whereas a freely expanding colony shows chaotic dynamics, where nematic domains are randomly forming and breaking, upon confinement, the colony exhibits a dramatically different behavior: it develops a global nematic order. To be specific, after a transient process of "chaotic" expansion, the growing bacterial colony develops a globally ordered state where the nematic director is normal to the direction of confinement. With computer simulations of the hard-rod model, we demonstrate a complex interplay among cell orientation, cell growth, and mechanical stresses. Especially, the combined effects of confinement and cell growth result in a globally anisotropic stress, where the stress components parallel to the direction of confinement are larger than their orthogonal counterparts. This anisotropic stress can drive cell to align along the direction of minimal stress (i.e. perpendicular to the direction

of confinement), and promote a global nematic order in the whole colony.

In chapter 5, we discuss how growth-induced stress can trigger the mono-to-multilayer transition in a bacterial colony. Using a combination of numerical simulations and analytical modeling, we demonstrate that the transition originates from the competition between growth-induced in-plane stresses and vertical restoring forces, due to the cell-substrate interactions. The mechanistic picture of this transition can be captured by a simple model of a chain-like colony of laterally confined cells. Mechanically, the transition is triggered by the mechanical instability of individual cell, thus it is localized and mechanically deterministic. Asynchronous cell division renders the process stochastic, so that all the critical parameters that control the onset of the transition are continuously distributed random variables. Upon modeling the transition as a Poisson process, we can approximately calculate the probability distribution functions of the position and time associated with the first extrusion. The rate of such a Poisson process can be identified as the order parameter of the transition, thus highlighting its mixed deterministic/stochastic nature.

Finally, we conclude our study with an outlook in chapter 6.

Chapter 2

Models

2.1 Discrete model

A growing bacterial colony is a typical complex system. Even in a simple setup (e.g. Fig. 1.5), there could be plenty of biochemical and mechanical interactions involved. Depending on the local arrangement of cells, mechanical interactions between neighboring cells may include steric repulsion if squeezing each other, cell-cell adhesion resulting especially from the molecular complexes known as *adhesins*, and frictional forces due to the relative motion [56, 65]. Similar types of forces can be found between cells and substrate [56, 65]. All these mechanical interactions originate from elastic contacts between soft bodies, i.e. cells and substrates, making it even more difficult to determine the magnitude and direction of the forces. In addition, cell growth, as the ultimate driving force, not only depends on the metabolic state of each cell, but also the local concentration of nutrient, which has its own spatial-temporal pattern controlled by the diffusive dynamics [62]. Modeling the system in its full complexity, would be far beyond the capabilities of simple models with few control parameters.

Here, we use a minimal model including only the ingredients that are essential to the dynamics of the system. Each bacterium is modeled as a spherocylinder with a fixed diameter d_0 and a time-dependent length l (excluding the caps on both ends, Fig. 2.1) [62]. The model is in general three-dimensional, but one can enforce it to be quasi-1D or quasi-2D by suppressing specific degrees of freedom. Each cell has a position $\boldsymbol{r}_i$ (the center of mass) and an orientation $\boldsymbol{p}_i$, which is a unit vector pointing from the cell center to either end of the cell. Although the two ends of the cell might have different biochemical or mechanical properties [65, 70], here in this thesis, we assume the cell to be symmetric, and hence $\boldsymbol{p}_i = -\boldsymbol{p}_i$.

Cell growth and division are modeled as following. The length l_i in-

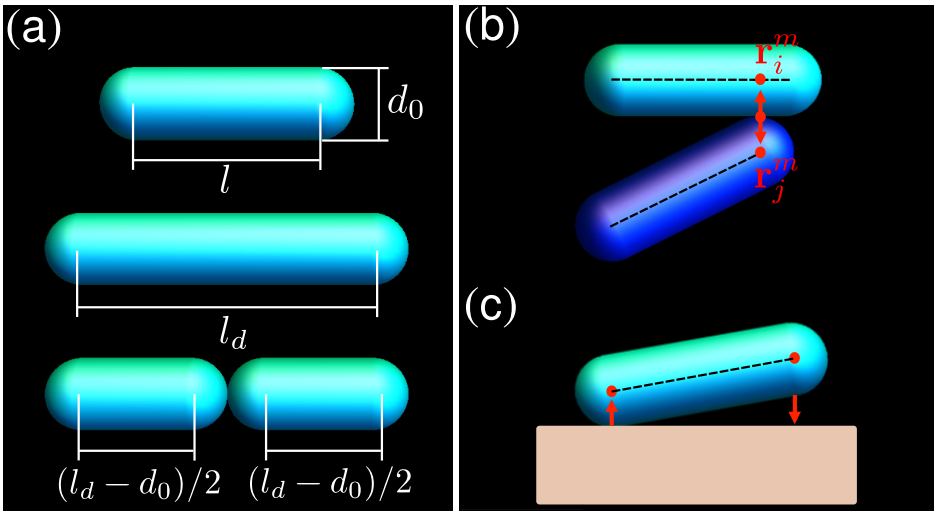

Figure 2.1. Schematics of the hard-rod model. (a) Each cell has a fixed diameter d_0 and a time-dependent length l (excluding the two caps) that increases linearly in time as demanded in Eq. 2.1. Once they reach the division length l_d, they divide into two identical daughter cells. (b) The steric interaction between neighboring cells is modeled as the Hertzian repulsion between two spheres of diameter d_0, centered respectively at $\boldsymbol{r}_i^m$ and $\boldsymbol{r}_i^m$, which minimize the distance between the cell axes (i.e. the two black dashed lines). (c) Each cell interact with the substrate through their caps. The forces on the two caps are calculated independently. They could be repulsive in case of penetration (left end), or attractive in presence of gap (right end).

creases linearly in time,

$$\frac{\mathrm{d}l_i}{\mathrm{d}t} = g_i, \tag{2.1}$$

where g_i is the growth rate of the ith cell. After it reaches the division length l_d, the cell divides into two identical daughter cells. In order to avoid synchronization of divisions, the growth rate of each cell is randomly drawn from a uniform distribution in the interval $[g/2, 3g/2]$, hence g is the average growth rate. Immediately after duplication, the daughter cells have the same orientation as the mother cell but independent growth rates. The rate of cell division can vary over time, with the increase of growth-induced local pressure [71, 72]. In bacterial colonies, however, such an effect takes place only at pressure values that are significantly larger than those experienced by the cells in a microcolony [73, 56] and has, therefore, been neglected in our model.

Neighboring cells, when overlap, interact stericly through a Hertzian-like contact force. To determine the direction and magnitude of the repulsion force, we first find the two points on the major axes of the two cells (black dashed lines in Fig. 2.1b), $\boldsymbol{r}_i^m$ and $\boldsymbol{r}_j^m$, which minimize the distance between the two major axes, hence maximize the overlap of the two cells. The force between the two rods is approximated as a force between two spheres of diameter d_0, centered at $\boldsymbol{r}_i^m$ and $\boldsymbol{r}_j^m$, respectively [62]. Specifically, the force from the jth cell to the ith is $\boldsymbol{F}_{ij}^c = Y_c d_0^{1/2} h_{ij}^{3/2} \boldsymbol{N}_{ij}$, where Y_c is proportional to the Young's modulus of the cell, $h_{ij} = d_0 - |\boldsymbol{r}_i^m - \boldsymbol{r}_j^m|$ is the overlap distance between the two cells, and $\boldsymbol{N}_{ij} = (\boldsymbol{r}_i^m - \boldsymbol{r}_j^m)/|\boldsymbol{r}_i^m - \boldsymbol{r}_j^m|$ the unit vector from $\boldsymbol{r}_j^m$ to $\boldsymbol{r}_i^m$. The point of contact is assumed to be at $\boldsymbol{r}_{ij} = (\boldsymbol{r}_i^m + \boldsymbol{r}_j^m)/2$.

Mechanical forces from the substrates, including the glass slide and the agarose gel on top, can be modeled implicitly, as if they were exerted from an imaginary plane spanning in the x and y directions, at $z = 0$. From now on, we refer to this imaginary plane as the "substrate" for convenience. Cells interact with the substrate through their caps, at positions $\boldsymbol{r}_{i\alpha} = \alpha l_i \boldsymbol{p}_i/2$ ($\alpha = \pm 1$) with respect to the cell center $\boldsymbol{r}_i$, and the force on each cap from the substrate is calculated independently (Fig. 2.1c). This force can be either repulsive or attractive, depending on the positions of the cap centroids, in such a way to model the impenetrability of the glass slide as well as the vertical repulsive force from the agarose gel. If $z_{i\alpha} < d_0/2$, where $z_{i\alpha}$ is the $z-$coordinate of the caps, the cell cap overlaps the substrate, hence is repelled with a Hertzian force $\boldsymbol{F}_{i\alpha}^s = Y_s d_0^{1/2}(d_0/2 - z_{i\alpha})^{3/2}\hat{\boldsymbol{z}}$, where Y_s is an effective elastic constant depending on the Young's modulus of the cell and the substrate. If on the other hand, there's a gap between the cell cap and the substrate, i.e. $d_0/2 < z_{i\alpha} < d_0/2 + r_a$, a vertical restoring force $\boldsymbol{F}_{i\alpha}^s = k_a l_i (d_0/2 - z_{i\alpha})\hat{\boldsymbol{z}}$ will be applied to the cell cap, with r_a the range of the restoring force (Fig. 2.1c). Here, the vertical restoring force can represent either the compression force from the agarose gel on top, or the adhesive forces from the glass/ECM, or a combination of both [56, 65, 66]. In presence of rigid wall confinement in the lateral direction, the repulsive force (no attractive force in this case) from the rigid wall can be calculated in the same way, but the magnitude of the force is proportional to Y_c instead of Y_s.

Since the system is highly overdamped, inertia plays a minor role here. Hence, the motion of cells is governed by the over-damped Newton equa-

tions for a rigid body [74], namely,

$$\frac{\mathrm{d}\boldsymbol{r}_i}{\mathrm{d}t} = \frac{1}{\zeta l_i}\left(\sum_{j=1}^{N_i^c} \boldsymbol{F}_{ij}^c + \sum_{\alpha=\pm 1} \boldsymbol{F}_{i\alpha}^s + \boldsymbol{\eta}_i\right), \tag{2.2a}$$

$$\frac{\mathrm{d}\boldsymbol{p}_i}{\mathrm{d}t} = \frac{12}{\zeta l_i^3}\boldsymbol{M}_i \times \boldsymbol{p}_i \tag{2.2b}$$

$$\boldsymbol{M}_i = \sum_{j=1}^{N_i^c}(\boldsymbol{r}_{ij} \times \boldsymbol{F}_{ij}^c) + \sum_{\alpha=\pm 1}(\boldsymbol{r}_{i\alpha} \times \boldsymbol{F}_{i\alpha}^s). \tag{2.2c}$$

The first term on the right-hand side of Eq. 2.2a represents the repulsive forces from neighboring cells, where the summation runs over all the cells in contact with the ith cell. The second term on the right-hand side of Eq. 2.2a represents the forces associated with the interaction between the cell caps and the substrate/confinement wall. $\boldsymbol{\eta}_i$ is a random kick to the ith cell whose components are randomly drawn from the uniform distribution in the interval $[-10^{-6}\mathrm{N}, 10^{-6}\mathrm{N}]$. $\boldsymbol{M}_i$ in Eq. 2.2c is the torque on the cell with respect to the cell centroid. Finally, Eqs. 2.2a and 2.2b represent respectively the displacement and rotation of the cell in response to the forces and the torques. The constant ζ is a drag per unit length, which is assumed to be independent of the cell orientation. Possible origins of this drag are adhesive or frictional forces from the substrates, or from the ECM produced by cells during the colonization [62, 65, 66].

2.2 Continuum theory

Previous studies as well as our results from the molecular dynamics simulations have suggested that a growing colony exhibits orientational order but no positional order [38, 51, 59, 63, 65], hence is a nematic liquid crystal. In addition, we also find that cell growth collectively gives rise to a deviatoric stress reminiscing the famous *active nematics* [7, 75]. For this reason, we will use the continuum theory of active nematics to characterize a growing bacterial colony. Detailed discussion on the connections between growing bacterial colonies and active nematics will be shown in chapter 3. Here, we will introduce the general hydrodynamic equations of active nematics.

A nematic liquid crystal, or nematics, is a state of matter where the system shows orientational order but no positional order [76, 77]. This

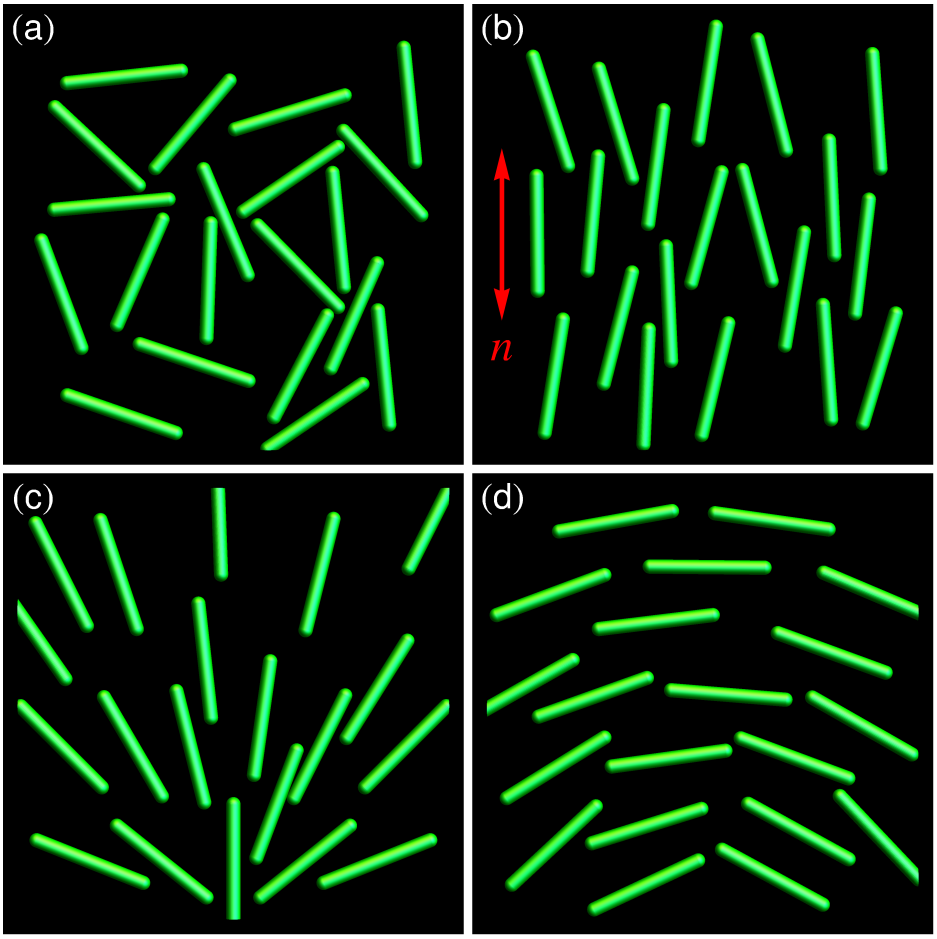

Figure 2.2. Orientational orders in nematic liquid crystals. (a) Isotropic state corresponding to an order parameter $S = 0$, and (b) highly aligned state with $S \approx 1$. The red arrow in (b) indicates the average orientation $\boldsymbol{n}$ of the particles. Note that $\boldsymbol{n} = -\boldsymbol{n}$. (c) Splay and (d) bending distortions of a two dimensional nematic liquid crystal.

orientational order can be driven either by excluded volume interactions between anisotropic-shaped particles, or anisotropic interactions between particles with arbitrary shape, and the resulting nematic phases are called lyotropic nematics and thermotropic nematics, respectively [76]. The orientational state of a nematics can be characterized by the so-called nematic order tensor $\boldsymbol{Q}$, which in a two-dimensional space is of the form:

$$\boldsymbol{Q} = S\left(\boldsymbol{nn} - \frac{1}{2}\boldsymbol{I}\right). \tag{2.3}$$

In Eq. 2.3, S is called the nematic order parameter, which quantifies the degree of orientational order and has a value continuously distributed from $S = 0$ (no orientational order, Fig. 2.2a) to $S = 1$ (perfectly aligned, Fig. 2.2b). $\boldsymbol{n}$ is a unit vector representing the average orientation of particles. Note that $\boldsymbol{n}$ and $-\boldsymbol{n}$ represent the same orientational state. $\boldsymbol{I}$ is the identity matrix.

In addition to $\boldsymbol{Q}$, we can also use the density field ρ and the velocity field $\boldsymbol{v}$ to characterize the mechanical state of a nematic liquid crystal. The dynamics of these material fields are then governed by the following hydrodynamic equations [76–78]:

$$\frac{D\rho}{Dt} = \mathcal{D}\nabla^2\rho\,, \tag{2.4a}$$

$$\frac{D(\rho\boldsymbol{v})}{Dt} = \nabla\cdot\boldsymbol{\sigma} - \xi\rho\boldsymbol{v}\,, \tag{2.4b}$$

$$\frac{D\boldsymbol{Q}}{Dt} = \lambda S\boldsymbol{u} + \boldsymbol{Q}\cdot\boldsymbol{\omega} - \boldsymbol{\omega}\cdot\boldsymbol{Q} + \gamma^{-1}\boldsymbol{H}\,, \tag{2.4c}$$

where $D/Dt = \partial_t + \boldsymbol{v}\cdot\nabla + (\nabla\cdot\boldsymbol{v})$ is the material derivative. Equation 2.4a describes the conservation of mass of the particles, when transported across the system by convective currents. An additional diffusive term, with $\mathcal{D}$ a small diffusion coefficient, is introduced for regularization, i.e. to smooth the sharp gradient of ρ during the simulations. The particles' momentum density $\rho\boldsymbol{v}$ is subject to the internal elastic stresses $\boldsymbol{\sigma}$ as well as the frictional force $-\xi\rho\boldsymbol{v}$ from the substrate. The former can, in turn, be expressed as

$$\boldsymbol{\sigma} = -p\boldsymbol{I} - \lambda S\boldsymbol{H} + \boldsymbol{Q}\cdot\boldsymbol{H} - \boldsymbol{H}\cdot\boldsymbol{Q}\,, \tag{2.5}$$

where the first term represents the isotropic pressure of magnitude p. The remaining terms describe the elastic stresses arising from the aligning

interactions between the particles. The molecular tensor field $\boldsymbol{H}$ in Eqs. 2.4c and 2.5 can be defined starting from the Landau–de Gennes free-energy density:

$$f_{\mathrm{LdG}} = \frac{1}{2}L_1|\nabla \boldsymbol{Q}|^2 + \frac{1}{2}A_2\mathrm{Tr}\boldsymbol{Q}^2 + \frac{1}{4}A_4\left(\mathrm{Tr}\boldsymbol{Q}^2\right)^2 \ , \tag{2.6}$$

as $\boldsymbol{H} = -\delta/\delta\boldsymbol{Q}\int \mathrm{d}A\, f_{\mathrm{LdG}}$. The first term in Eq. 2.6 promotes a homogeneous nematic order, for any gradient of the nematic tensor $\boldsymbol{Q}$, either from the order parameter S or from the director $\boldsymbol{n}$, will cost certain amount of free energy. In a two-dimensional nematics, possible distortions of $\boldsymbol{n}$ are splay (Fig. 2.2c) and bending (Fig. 2.2d), and $L_1 > 0$ is an orientational stiffness penalizing, in equal amounts of the two deformations. The last two terms in Eq. 2.6 describe a continuous phase transition between the isotropic ($S = 0$) and the nematic ($S > 0$) phases, where the boundary is set by functions A_2 and A_4 ($A_4 > 0$). At equilibrium, $\boldsymbol{H} = \boldsymbol{0}$ and we have

$$S = \begin{cases} 0, & \text{for } A_2 > 0, \\ \sqrt{-2A_2/A_4}, & \text{for } A_2 < 0. \end{cases} \tag{2.7}$$

If the nematic tensor $\boldsymbol{Q}$ deviates from the equilibrium configuration, $\boldsymbol{H} \neq \boldsymbol{0}$, and it will try to drive the $\boldsymbol{Q}$ tensor back to equilibrium through the following ways. First of all, a nonzero $\boldsymbol{H}$ will generate an orientational elastic stress as listed in the last three terms of Eq. 2.5. This stress can cause a material flow (the so-called backflow effect), which can then restore the $\boldsymbol{Q}$ field. Second, the molecular tensor $\boldsymbol{H}$ also plays the role of restoring torque which, according to the last term of Eq. 2.4c, can reorient the nematic tensor directly toward the equilibrium configuration, with a rotational viscosity γ. Finally, the particles also rotate as a consequence of the flow gradient. This effect is embodied in the first three terms of Eq. 2.4c, with $u_{ij} = (\partial_i v_j + \partial_j v_i - \delta_{ij}\nabla\cdot\boldsymbol{v})/2$ and $\omega_{ij} = (\partial_i v_j - \partial_j v_i)/2$ representing the strain rate and the vorticity tensor, respectively, and λ the flow-alignment parameter [78, 79].

Equations 2.4 can also be used to described active materials, and such systems are usually referred to as *active nematics* [7, 29, 75]. These have been successfully used in the past decade to describe a variety of active fluids, typically of biological origin, consisting of self-propelled or mutually propelled apolar building blocks, such as *in vitro* suspensions of microtubules and kinesin [29, 40, 80–86], microswimmers [41], and cellular monolayers [23, 75, 87]. Recently, attempts have been made to describe

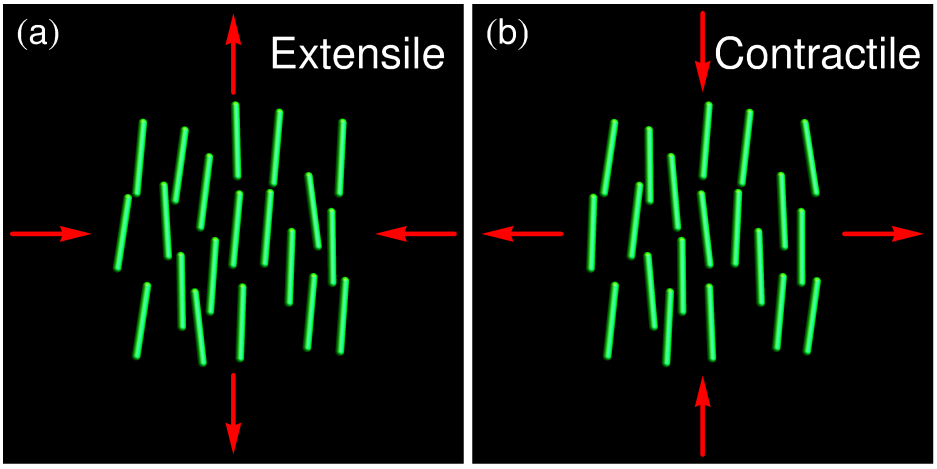

Figure 2.3. Sketches of (a) extensile and (b) contractile active stresses. The arrows show the stresses that the volume element exerts on the surroundings.

sessile bacteria, in the language of nematic liquid crystals [38, 63]. A common feature of these systems is that the activity of the cells or other building blocks collectively generates a deviatoric active stress [7, 29, 75]

$$\boldsymbol{\sigma}^{\mathrm{a}} = \alpha \boldsymbol{Q}. \tag{2.8}$$

Equation 2.8 describes a force dipole of a magnitude proportional to $|\alpha|$ and the nematic order parameter S, and with an axis parallel to the nematic director $\boldsymbol{n}$. The stress is called extensile if $\alpha < 0$ (Fig. 2.3a), and contractile if $\alpha > 0$ (Fig. 2.3b) [7, 29, 42, 75]. In the case of extensile active stress, the stress that a volume element exerts on its surroundings is extensile along the director $\boldsymbol{n}$ and contractile in the perpendicular direction. The contractile active stress has the same structure, but the forces are of the opposite directions. Experiments and simulations have shown that the active stress can drive the system far from thermal equilibrium, and can dramatically alter the dynamics of the system [7, 19, 29, 82, 86]. For example, the extensile active stress can destabilize a homogeneous director through bending, and lead to the proliferation of $\pm 1/2$ defect pairs [82]. It can also propel the $+1/2$ defects, and this can drive the flow into the turbulent region, creating the so-called *active turbulence* [7, 29, 86]. We shall see in the following chapters that the growth of bacteria will generate an extensile active stress and the colony can be well described by the hydrodynamics equations of active nematics with suitable modifications.

Chapter 3

Geometry and mechanics of freely expanding colonies

The ability of forming biofilms is a robust and widely observed property across different bacterial species [50]. Despite the extraordinary diversity within prokaryotic microorganisms, nearly all bacteria, either as single species or in a community, possess the necessary biomolecular "toolkit" to colonize a range of natural or synthetic surfaces through autonomous production of extracellular matrix (ECM) [47]. Starting from a single bacterium, the colony gradually colonize the surroundings through a series of well-regulated protocols. The first step is to extend its territory with a monolayer expansion. With a solid ground, it invades the third dimension by squeezing cells out of the monolayer, and subsequently forms a multilayered structure and then a mature biofilm [43–47]. In all these processes, mechanical forces play a very important role.

In this chapter, we will explore the spatial organization and mechanical properties in a freely expanding monolayer–the "childhood" of a biofilm. Using molecular dynamics simulations and continuous modeling, we demonstrate that the dynamics of the freely expanding monolayer is dominated by the competing effects of cell slenderness and cell growth. On the one hand, passive steric repulsion between the rod-shaped cells tends to align the cell axes, and promotes local nematic order. On the other hand, cell elongation along the axis generates an extensile active stress in the colony, which can bend the director and create a distortion. The competition between the passive and growth-induced active forces results in a complex internal dynamics as well as the emergence of coherent structures (Figs. 3.1a–d) reminiscent of those observed in active liquid crystals [29, 88–91]. Especially, the expanding colony self-organizes into a "mosaic" of nematic microdomains, whose sizes are exponentially distributed, with a characteristic length scale proportional to the square root of the ratio between the system orientational stiffness and the magnitude of the extensile active

stress. Both active and passive forces scale linearly with the cell density. Therefore, despite the colony being denser in the center than at the periphery, such an inherent length scale remains uniform throughout the system. Finally, to assess the significance of our theoretical model, we compare our predictions with experiments on freely growing *E. coli* microcolonies (Fig. 3.1). Whereas the statistics of our experiments are not sufficient to make conclusive statements, we do not find obvious discrepancies with our theoretical model. In contrast, the agreement between theory and experiments justifies some degree of optimism and creates promising ground for future experimental research.

3.1 Stochastic geometry

We use the hard-rod model introduced in section 2.1 to simulate the freely expanding monolayer. We assume the colony to be perfectly quasi-two-dimensional, i.e. cells only move in the xy-plane, and the force components in the third dimension have no effects on the in-plane dynamics. To do so, we manually set $z_i = d_0/2$ and $q_{iz} = 0$ for all cells and at all times. Equations 2.1 and 2.2 have been numerically integrated using the following set of parameter values: $d_0 = 1\,\mu$m, $Y_c = 4$ MPa, and $\zeta = 200$ Pa h [62]. The division length l_d varies from $2\,\mu$m to $5\,\mu$m, and the growth rate varies from $1\,\mu$m/h to $10\,\mu$m/h. The integration is performed with a time step $\Delta t = 0.5 \times 10^{-6}$ h. Each simulation starts with one randomly oriented cell and stops when the total length of the cells in the colony, i.e., $\mathcal{L} = \sum_i^N (l_i + d_0)$, reaches the value $37500\,d_0$, such that colonies with different l_d values have approximately the same colony area at the end of the simulation. We can rescale the length by the cell diameter d_0 and the time by ζ/Y_c. In these units, our hard-rod model has only two free parameters: l_d/d_0, which represents the cell slenderness or aspect ratio, and the rescaled growth rate $g\zeta/(Y_c d_0)$. In the remainder of this chapter, all results are presented in terms of dimensionless quantities, unless otherwise specified.

Figure 3.1 shows the typical configurations observed at the early stages of colonization both *in vitro* and *in silico*. Along the colony boundary, cells are predominantly tangentially aligned, as a consequence of torque balance. As the forces experienced by the peripheral cells are radial, these cells must orient either tangentially or normally with respect to the boundary in order for the torque acting on them to vanish. Normal alignment

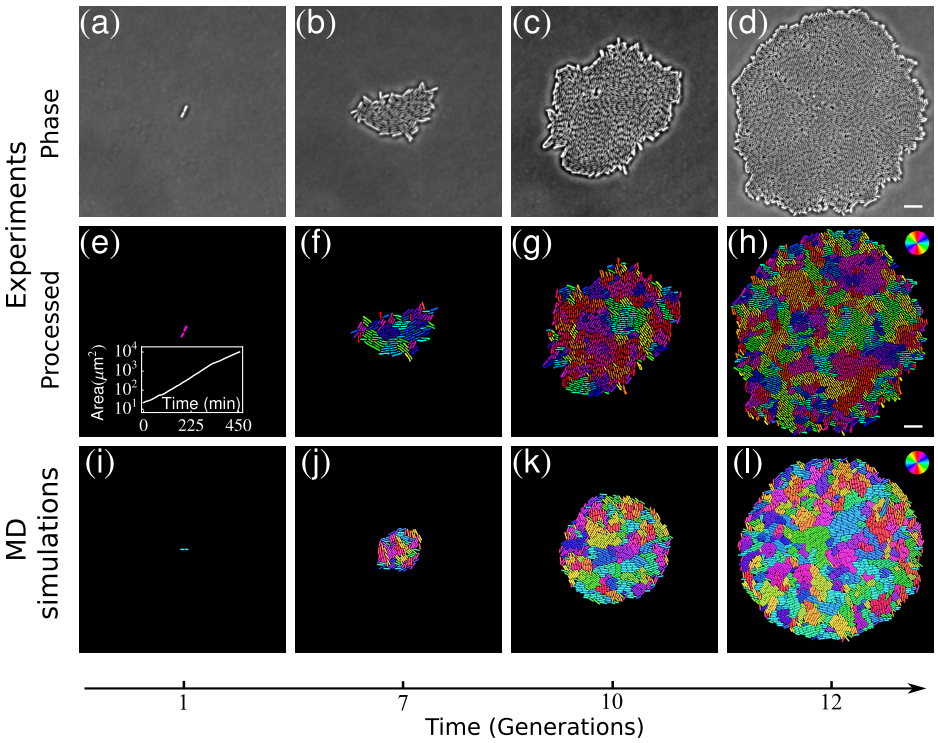

Figure 3.1. Growth of a bacterial colony. (a)–(d) Phase-contrast micrographs at different time points capture the growth of a single cell of nonmotile strain of *Escherichia coli* (strain NCM 3722 delta-motA) to a two-dimensional colony under free boundary conditions. The scale bar corresponds to 10 μm. The cell doubling time was 43.5 ± 2.2 minutes. After 12 generations (d), the colony was observed to escape into the third dimension and form a second bacterial layer. (e)–(h) Image analyzed snapshots of (a)–(d), capturing the emergence of local orientational order within the growing bacterial colony, represented by differently colored microdomains. Cells are color-coded by the orientation of the domains they belong to, as described in the color wheel in panel (h). The inset in panel (e) plots the area of the growing bacterial colony over time, showing the exponential growth of cells in the colony. (i)–(l) The corresponding time points during the growth of the bacterial colony obtained using molecular dynamics simulations. Cells are color-coded with the same method as in panels (e)–(h). By varying the aspect ratio of the cells (length/width) between 1.5 and 4, different physiological states were simulated.

is, however, unstable; therefore, most of the peripheral cells are oriented tangentially. This tangential alignment has also been observed in several other studies [63, 65]. In bulk of the colony, the emergence of local nematic order is conspicuous throughout the system; however, this does not propagate across the colony but remains confined to a set of microscopic domains. These nematic domains, or "patches," are separated from each other by fracture lines reminiscent of grain boundaries in crystals [92, 93]. We can then use these domains to characterize the geometrical properties of a growing bacterial colony and, hopefully can also infer the mechanical properties of such systems.

At first glance, these nematic domains show very complicated spatial-temporal dynamics. As the colony evolves, the domains grow, merge, buckle, and break apart, in a complex sequence of morphological and topological transformations. These phenomena suggest a chaotic nature of the freely expanding monolayer. Despite the complex dynamics, these domains exhibit very robust statistical properties. Figure 3.2 shows three examples of proliferating colonies of cells, each with different l_d values and, hence, different cell aspect ratios. The typical domain area, as we can see, increases with the cell aspect ratio. Although the microdomains possess local orientational order, no preferential orientation was observed at the scale of the colony, suggesting that the colony itself is globally isotropic. The absence of the global orientational order can be ascribed to the inherent instability of the domains, which continuously deform and fracture under the effect of growth-induced stress. The typical domain area then represents not only the coherent length scale of orientational order but also the length scale at which the internal stresses compromise.

To quantify the emergent geometry of microdomains in a colony, we apply a customized domain segmentation algorithm. Two cells are considered to belong in the same domain if they are in contact, and their relative orientation differed by less than 3%. Although decomposition of a colony depends on the chosen threshold, the overall nature of the geometry and the emergent trends identified through different quantifiable parameters are generally robust and independent of the chosen threshold. By using this algorithm, we can then identify domains; measure their positions, orientations, areas *et al.*; and get statistics of these quantities.

A central quantity to characterize the geometry of a colony is the probability density of the area of these microdomains, $P(A)$. This is shown in Fig. 3.3a for colonies with different l_d values. The frequency of

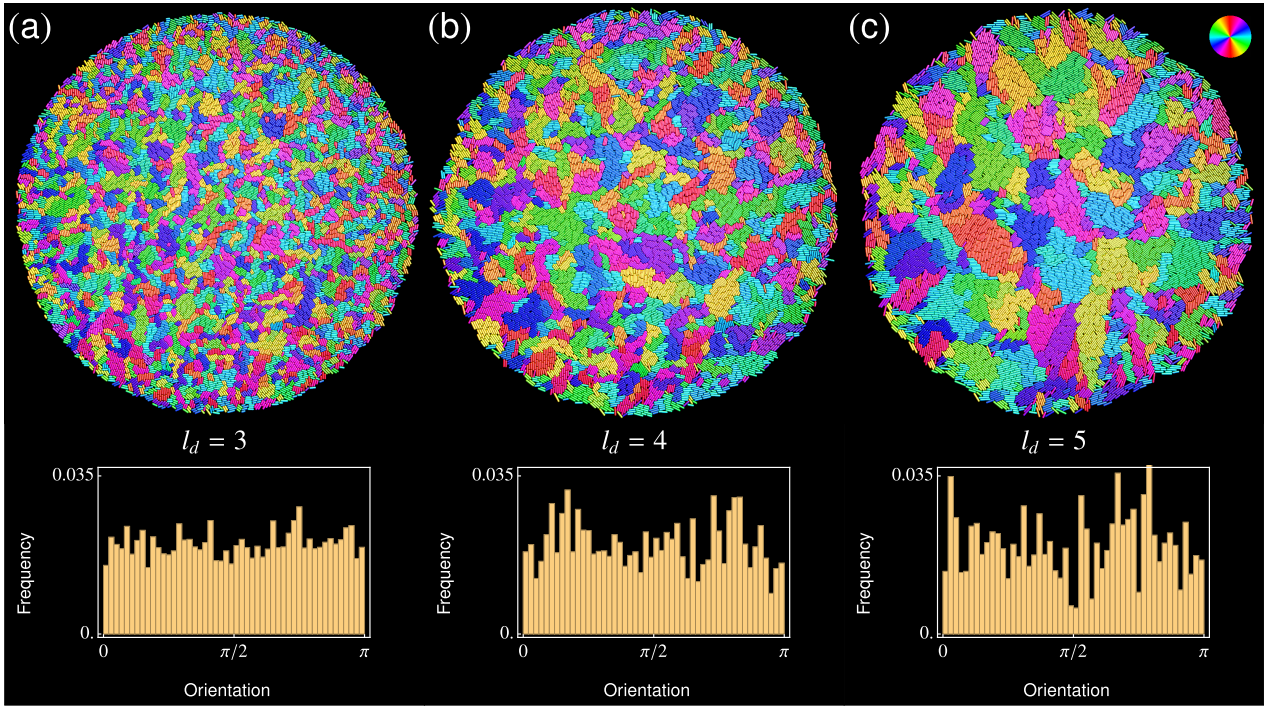

Figure 3.2. Emergence of nematic domains in proliferating bacterial colonies. (a)–(c) Examples of nematic microdomains in simulated bacterial colonies for various division lengths (l_d = 3, 4, 5, in units of the cell diameter d_0). Cells are colored with the same method as in Fig. 3.1. Upon increasing the division length, the typical area of the domains increases progressively. Inside a domain, the cells are highly aligned, while there is no preferential orientation at the scale of the entire colony, as confirmed by the probability distribution of cell orientations (corresponding panels in the lower row).

domains with area A decreases with A and, for sufficiently large A values, $P(A)$ approaches the exponential distribution:

$$P(A) \sim \exp\left(-\frac{A}{A^*}\right) , \tag{3.1}$$

where A^* is a characteristic area scale proportional to the average domain area. For small A values, the distribution slightly deviates from the exponential form. This range corresponds to the boundary of the colony where, because of the sudden drop in packing fraction, domains are very small or consist of single cells. Although small domains seem to be outnumbered large domains in the exponential region, they actually occupy relatively small area in the whole colony, as can be obviously seen in Fig. 3.2. This is because a large domain typically is as large as tens or even hundreds of small domains altogether. For this reason, it's fair to say that the domain size is exponentially distributed in a growing colony.

We will now quantify the spatial dependence of the domains. First of all, we notice that a sufficiently large colony has a rotational symmetry about the colony center. This rotational symmetry is commonly shared by all geometrical and mechanical quantities, which then depend exclusively on r, the distance from the colony center. We calculate the average domain area restricted to an annular strip, of width $5d_0$, and located at distance r from the center of the colony, i.e., $\langle A \rangle_r$ (Fig. 3.3b). The local domain area is uniform in the bulk of the colony, for a given cell aspect ratio, before dropping to zero at the boundary, where the colony is more disordered. In turn, the average domain area in the bulk $\langle A \rangle$ is strongly affected by the division length l_d. This is visibly conspicuous in Fig. 3.2. Increasing l_d makes the cells, on average, more slender, resulting in larger and more stable domains, as revealed by the plot in Fig. 3.3c. More interestingly, increasing the growth rate g has the opposite effect and causes a drop in the domain area (Fig. 3.3d). All data in Fig. 3.3, as well as those in Figs. 3.4, 3.5, 3.6, and 3.7 are obtained by averaging over 480 runs. All simulation results in this chapter are obtained by analyzing the configurations of the colonies at which the simulations stop, unless otherwise specified. The error bars show the standard deviations of the 480 samples with respect to the mean values.

The results reported in this section quantitatively demonstrate that the spatial organization of the microdomains in expanding bacterial colonies is regulated by the competing effects of the cell aspect ratio and the growth rate. These effects can ultimately be ascribed to the mechanical proper-

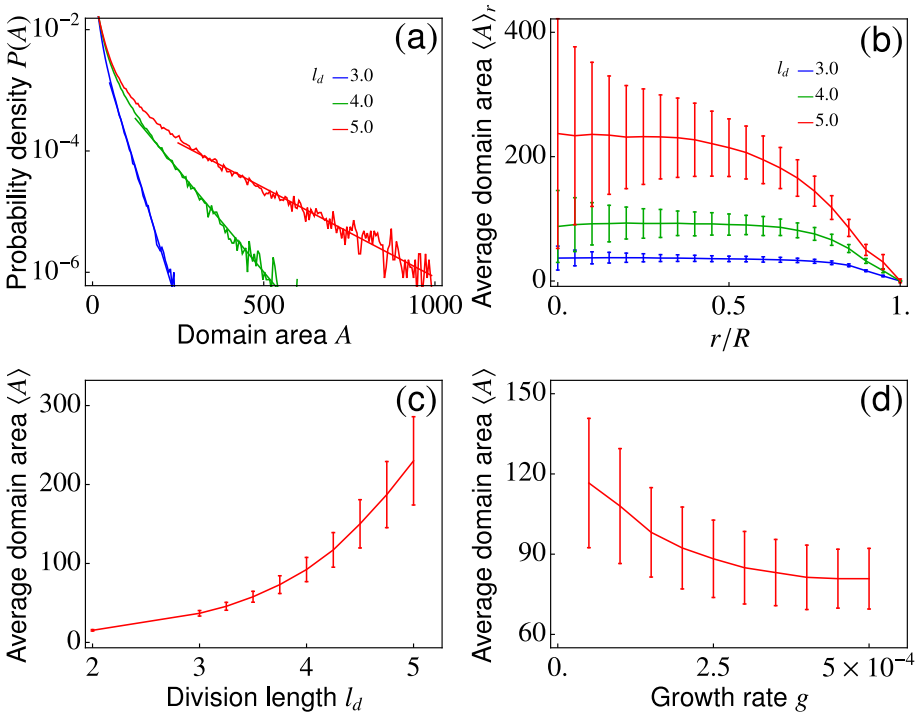

Figure 3.3. Geometry of nematic microdomains in bacterial colonies. (a) Probability distributions of domain area, $P(A)$, for various division length l_d. The domain area follows the exponential distribution $P(A) \sim \exp(-A/A^*)$, with $A^* = 54.3$, 148.2, and 338.8, respectively, which increases with the division length l_d. (b) The average domain area at a distance r from the center of the colony, showing that the area of the domains is found to be constant in the bulk of the colony and drops to zero at the boundary. (c,d) The bulk domain area $\langle A \rangle$ (c) increases with the division length l_d and (d) decreases with the growth rate g. Here, $\langle A \rangle$ is calculated by averaging the areas of all domains within the range $0 \leq r \leq R/2$, with R the colony radius. All results shown in panels (a)–(c) correspond to a fixed growth rate of $g = 0.0002$ (or 4μm/h in physical units), while panel (d) represents simulation results with a fixed division length $l_d = 4$.

ties of the system, as we explain in the next section. We stress here that our approach does not aim to faithfully reproduce all the experimental details but rather to provide a conceptual key for understanding certain geometrical and mechanical properties, with the help of a minimal model comprising a single fitting parameter: i.e., the timescale $\tau = \zeta/Y$. Other properties, such as the roughness of the colony edge and smoother variation in the orientation of neighboring domains, are not well captured by our simple model and would require a more sophisticated construction, accounting for the adhesive interaction between neighboring cells, the flexibility of the cell membrane, and more specific cell-substrate interactions [65]. Unfortunately, this would imply a cost in terms of free parameters and reduced simplicity in the interpretation of the numerical results.

3.2 Mechanics

The domain geometry in a proliferating bacterial colony is determined by the interplay between two competing forces: steric repulsion between neighboring cells and the extensile stresses due to cell growth. While cell-cell steric repulsion favors alignment, the emergent extensile stresses due to the growth within a restricted environment (i.e., the space delimited by the neighboring domains) tend to deform and eventually fracture a domain. Both of these effects are due to contact forces and are, therefore, enhanced by the local packing fraction ϕ.

To clarify this concept, we measure the local packing fraction $\phi(r,t) = \sum_i a_i(t)/\mathcal{A}_r$, where $a_i(t)$ is the area of the ith cell, located at time t inside a thin annulus of radius r, width $5d_0$, and area $\mathcal{A}_r$, centered at the colony center. As mentioned before, the colony has a radial symmetry; hence, the local packing fraction depends exclusively on the distance r from the center. Figure 3.4a shows that at any given time, the packing fraction decreases monotonically with r. As bacteria duplicate and progressively colonize the surrounding space, the local packing fraction increases with time throughout the system while maintaining a characteristic spatial profile that smoothly interpolates between a time-dependent maximum $\phi(0,t) = \phi_{\max}(t)$, at the center of the colony, and a time-independent minimum, $\phi(R,t) = \phi_c$, at the edge (R being the colony radius). The quantity $\phi_c \approx 1$ is the critical packing fraction at which the cells first start to compress each other. In close proximity of the edge of the colony, $\phi < \phi_c$, and the contact forces tend to reorient the cells with-

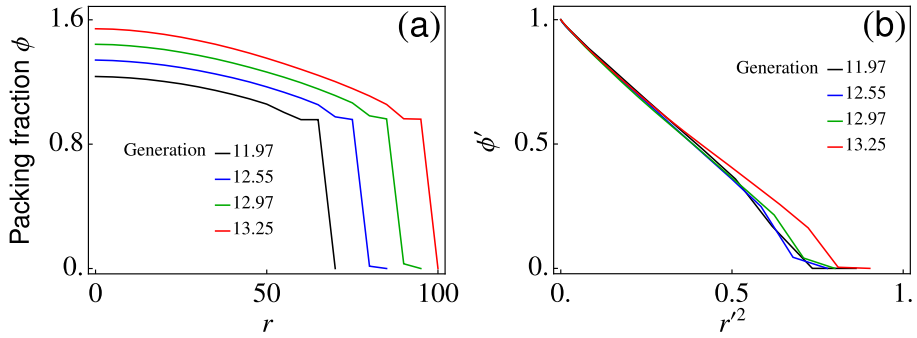

Figure 3.4. (a) Spatial dependence of the packing fraction for different ages of colonies. (b) The rescaled packing fraction $\phi' = [\phi(r) - \phi(R)]/[\phi(0) - \phi(R)]$ versus $r'^2 = (r/R)^2$. All the curves collapse on the same line as demanded by Eq. 3.2. The growth rate and the division length are fixed, i.e., $g = 0.0002$ and $l_d = 4$. The packing fraction ϕ is averaged over a thin annulus of radius r and width $5d_0$, centered at the colony center. In all results presented, the length is expressed in units of the cell width, d_0, and time in units of the timescale ζ/Y_c defined in Eqs. 2.2.

out compressing them, leading to an abrupt drop in the packing fraction. Upon rescaling the packing fraction by $\phi(0) - \phi(R)$ and the distance r by the colony radius R, the spatial dependence of the pacing fraction can be described, at any time, by a simple quadratic law:

$$\frac{\phi(r) - \phi(R)}{\phi(0) - \phi(R)} = 1 - \left(\frac{r}{R}\right)^2 , \tag{3.2}$$

as illustrated in Fig. 3.4b. As we analytically prove in section 3.3, such a density profile originates from the balance between growth-induced pressure and drag from the substrate.

The tendency of the cells to align with each other is driven by the local steric interactions and can be conceptualized in the framework of Frank elasticity [77], starting from the free-energy density:

$$f_F = \frac{1}{2} k_F |\nabla \boldsymbol{n}|^2 . \tag{3.3}$$

Here, k_F is an orientational stiffness penalizing, in equal amounts, splay and bending deformations, and $\boldsymbol{n}$ is the local nematic director corresponding to the average orientation of the bacteria in a local region. Any departure from the uniformly aligned configuration causes restoring forces

proportional to the field $\boldsymbol{h} = -\delta/\delta\boldsymbol{n} \int \mathrm{d}A\, f_F = k_F \nabla^2 \boldsymbol{n}$ [77]. As a consequence of growth, each cell further acts as an extensile force dipole that pushes away its neighbors along the $\pm\boldsymbol{n}$ direction. This collectively gives rise to an internal stress of the form

$$\boldsymbol{\sigma} = -p\boldsymbol{I} + \alpha \left(\boldsymbol{nn} - \frac{1}{2}\boldsymbol{I} \right) , \tag{3.4}$$

where p is the pressure, $\boldsymbol{I}$ the identity matrix, and α the deviatoric active stress [94, 39]. In the most general case, the three quantities k_F, p, and α, appearing in Eqs. 3.3 and 3.4, are functions of the local packing fraction and the nematic order parameter, in addition to the cell aspect ratio and the growth rate.

Equations 3.3 and 3.4 identify a fundamental length scale $\ell_\mathrm{a} = \sqrt{k_F/|\alpha|}$, proportional to the distance at which the passive restoring forces arising in the system, in response to a local distortion, balance the active forces that cause the nematic director to rotate [29]. This length scale plays a pivotal role in the mechanics of active nematic liquid crystals [95–98, 78] and, as we clarify later, determines their collective behavior and mechanical properties. In the following, we demonstrate that, in a growing colony of nonmotile cells, the inherent length scale ℓ_a determines the geometrical properties of the microdomains in such a way that $\langle A \rangle \sim \ell_\mathrm{a}^2$. For this purpose, we measure the orientational stiffness k_F and the stresses $\boldsymbol{\sigma}$ exerted inside the colony. The stress experienced by the ith cell, $\boldsymbol{\sigma}_i$, can be calculated from the virial expansion [38]:

$$\boldsymbol{\sigma}_i = \frac{1}{a_i'} \sum_j \boldsymbol{r}_{ij}\, \boldsymbol{F}_{ij} , \tag{3.5}$$

where $a_i' = a_i/\phi$ is the effective area occupied by the ith cell. We express the tensor in the basis of the nematic director and its normal $\boldsymbol{n}^\perp = (-n_y, n_x)$, namely,

$$\boldsymbol{\sigma} = \sigma_\parallel \boldsymbol{nn} + \sigma_\perp \boldsymbol{n}^\perp \boldsymbol{n}^\perp + \tau(\boldsymbol{nn}^\perp + \boldsymbol{n}^\perp \boldsymbol{n}) . \tag{3.6}$$

Figure 3.5a shows a plot of the various components of the stress tensor versus the packing fraction, given by Eq. 3.5. As expected, the normal stresses $\sigma_\parallel$ and $\sigma_\perp$ increase with the packing fraction and, at any finite packing fraction, are such that $|\sigma_\parallel| > |\sigma_\perp|$, as a consequence of the anisotropic cell growth. The shear stress τ, on the other hand, is always negligible because of the absence of lateral friction between the cells.

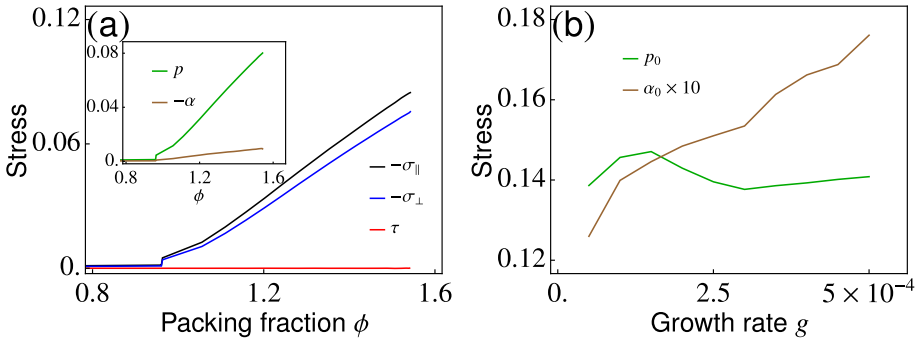

Figure 3.5. (a) Different components of the internal stress $\boldsymbol{\sigma}$ as functions of packing fraction ϕ. The normal stress parallel to the director $\boldsymbol{n}$, $|\sigma_\parallel|$, is larger than that perpendicular to it, i.e., $|\sigma_\perp|$. Both $|\sigma_\parallel|$ and $|\sigma_\perp|$ are piecewise linear functions of ϕ, while the shear component τ vanishes. The normal components of stress can be rearranged into a hydrostatic pressure p and an extensile active stress α, and both increase linearly with the packing fraction (inset). The simulation parameters are the same as those in Fig. 3.4. Again, $\boldsymbol{\sigma}$ is averaged over a thin annulus of radius r and width $5d_0$, centered at the colony center. (b) The pressure is independent of growth rate g, while the active stress increases with g. Here, $l_d = 4$ is fixed.

Note that both $\sigma_\parallel$ and $\sigma_\perp$ are negative because of the extensile nature of the growth-induced forces. The dependence of the normal stresses on the packing fraction is piecewise linear: For $\phi < \phi_c$, the contact forces can be relieved by rotations and repositioning of the cells, and $\sigma_\parallel \approx \sigma_\perp \approx 0$; however, for $\phi > \phi_c$, the cells in the bulk are tightly packed, and internal stresses build up as the packing fraction increases. Setting $\tau = 0$ in Eq. 5.28 and taking $\boldsymbol{n}^\perp\boldsymbol{n}^\perp = \boldsymbol{I} - \boldsymbol{nn}$, one can rearrange the stress tensor in the form

$$\boldsymbol{\sigma} = -\frac{|\sigma_\parallel + \sigma_\perp|}{2}\,\boldsymbol{I} + (\sigma_\parallel - \sigma_\perp)\left(\boldsymbol{nn} - \frac{1}{2}\,\boldsymbol{I}\right) . \tag{3.7}$$

Comparing this with Eq. 3.4 straightforwardly yields $p = (|\sigma_\parallel + \sigma_\perp|)/2$ and $\alpha = \sigma_\parallel - \sigma_\perp$. Together with the numerical results summarized in Figs. 3.5a–b, this implies

$$p = p_0(\phi - \phi_c) , \qquad \alpha = -\alpha_0|\phi - \phi_c| , \tag{3.8}$$

as long as $\phi > \phi_c$. Not unexpectedly, the longitudinal growth of the cells gives rise to an extensile (i.e., $\alpha < 0$) active stress that decreases monotonically with the distance from the center of the colony. The prefactors

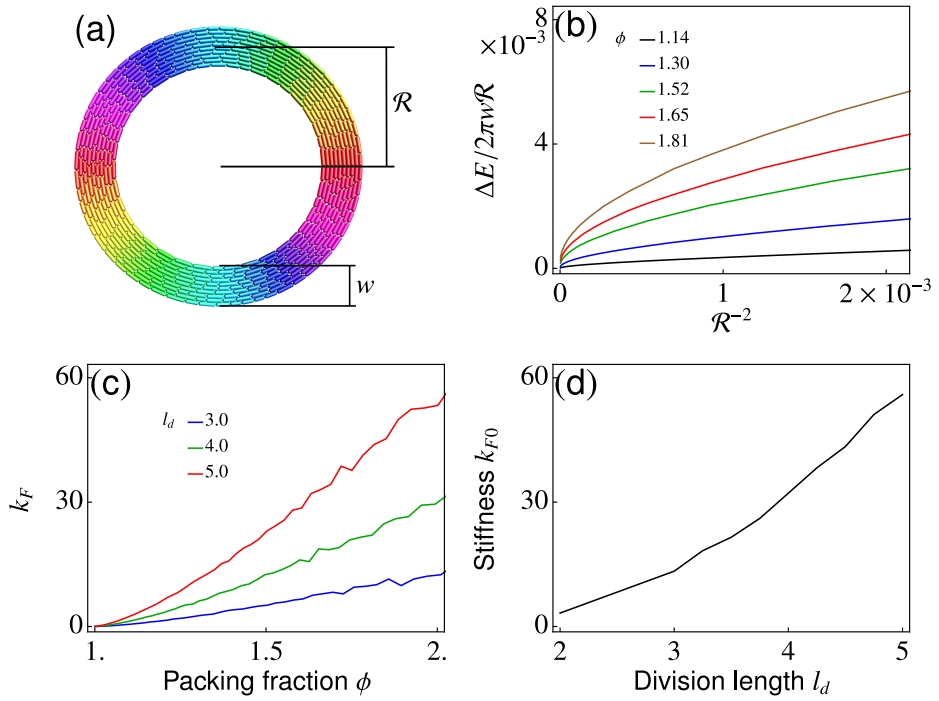

Figure 3.6. (a) The ring-shaped colony we used to measure the bending stiffness k_F. It has a radius $\mathcal{R}$ and a width w. Cells are colored by their orientations according to the color wheel in Fig. 3.1. (b) Difference of energy density (energy per unit area) between the straight channel and a ring-shaped channel of radius $\mathcal{R}$, as a function of $\mathcal{R}^{-2}$. (c) The orientational stiffness k_F increases linearly with the packing fraction at fixed l_d. (d) The prefactor of the linear fit, k_{F0}, increases with the division length l_d.

p_0 and α_0 are plotted in Fig. 3.5b as a function of the growth rate g. The active stress α_0 increases monotonically with g, while p_0 is essentially independent.

In order to estimate the orientational stiffness k_F, we manually arrange our *in silico* bacterial colony inside an annular channel of width $w = 10d_0$ and radius $\mathcal{R}$ (Fig. 3.6a, $w \ll \mathcal{R}$), as well as in a straight one of the same width and lengthed $2\pi\mathcal{R}$. In both configurations, the energy associated with the Hertzian contacts can be measured as: $E = (2/5)\, Y_c d_0^{1/2} \sum_{\langle ij \rangle} h_{ij}^{5/2}$, where the summation runs over all the pairs of cells in contact with each other. By comparing how the energy den-

sity changes with the curvature of the channel, we can infer the orientational stiffness. Figure 3.6b shows a plot of the difference $\Delta E = E(\phi, \mathcal{R}) - E(\phi, \infty)$ between the energy of a bent channel with radius $\mathcal{R}$ and a straight channel (both have a length $2\pi\mathcal{R}$), normalized by the area $2\pi w\mathcal{R}$ of the channel, as a function of the squared curvature $\kappa^2 = 1/\mathcal{R}^2$. From Eq. 3.3, it follows that $k_F = \partial_{\kappa^2}\Delta E/(2\pi w\mathcal{R})|_{\kappa=0}$. As shown in Fig. 3.6c, at fixed division length, the orientational stiffness k_F increases linearly with the packing fraction, i.e., $k_F = k_{F0}(\phi - \phi_c)$. Furthermore, increasing the slenderness of the cells makes the colony orientationally stiffer (Fig. 3.6d).

Combining the measurements of the extensile active stress and the orientational stiffness, we are finally able to formulate a scaling law for

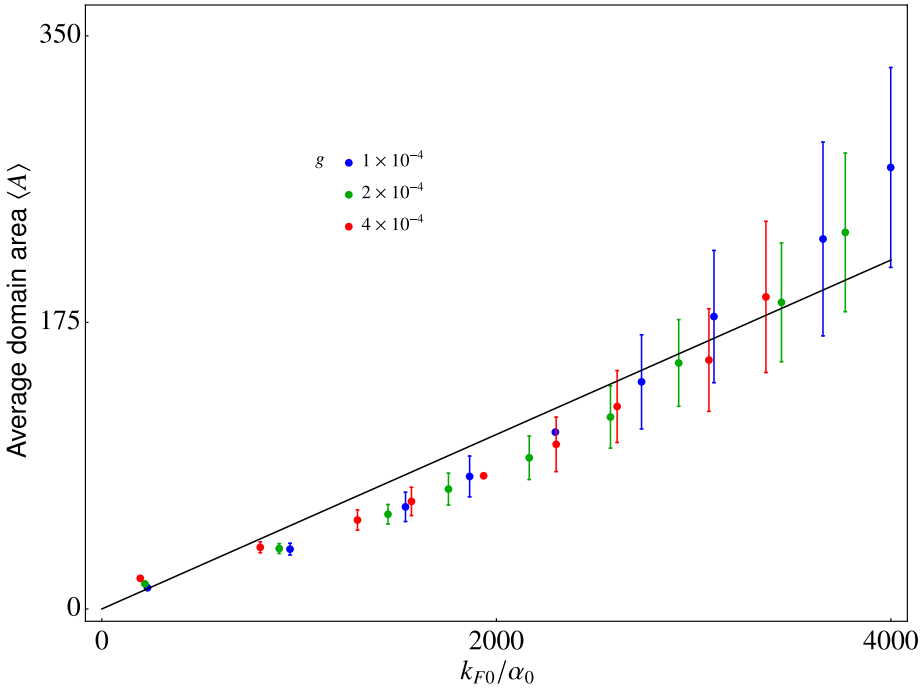

Figure 3.7. The average domain area $\langle A \rangle$ is approximately proportional to k_{F0}/α_0, for various combinations of growth rate and division length. We choose three growth rates (identified by colors), and for each growth rate, we gradually increase the division length from $l_d = 2$ to $l_d = 5$, corresponding to different data points with the same color.

the area of the nematic microdomains comprising our simulated bacterial colonies. Namely,

$$\langle A \rangle \sim \frac{k_F}{|\alpha|} \,, \tag{3.9}$$

in agreement with our numerical data (Fig. 3.7). In summary, bacterial colonies freely growing on a two-dimensional frictional substrate spontaneously organize into a "mosaic" of microdomains consisting of highly aligned cells. The domains are randomly oriented so that the colony is globally isotropic and circularly symmetric at the global scale, while their areas are exponentially distributed, as indicated in Eq. 3.1. Such a distribution results from the competition between passive steric forces, which favor local alignment, and the extensile active forces originating from the cell growth. These forces balance at the length $\ell_{\mathrm{a}} = \sqrt{k_F/|\alpha|}$, resulting in a characteristic domain area that scales as ℓ_{a}^2. Remarkably, both the orientational stiffness k_F and the extensile active stress α scale linearly with the packing fraction ϕ. Consequently, $k_F/\alpha = k_{F0}/\alpha_0$, so the average domain area is uniform throughout the colony (Fig. 3.3b). Such a cancellation of the dependence is intriguing: It is presumably specific to the type of interactions chosen here, which we do not expect to hold in general. Including the bending elasticity of the cells could, for instance, change the packing fraction dependence of k_F and α, resulting in a space-dependent active length scale. Yet, the mechanism described here and summarized by Eq. 3.9 is general and does not depend on the details of the model.

3.3 Continuum theory

In this section, we demonstrate that much of the behavior previously described can be quantitatively captured in the realm of continuum mechanics by means of a suitable extension to the hydrodynamic equations of active nematic liquid crystals. Here, we introduce a comprehensive hydrodynamic framework, incorporating the density effects described in the previous section as well as the deviatoric active stresses in the colonization dynamics.

An expanding bacterial colony can be described in terms of the material fields ρ, $\boldsymbol{v}$, and $\boldsymbol{Q}$, representing, respectively, the cell density, velocity, and the nematic order. The dynamics of these fields is then governed by

the following hydrodynamic equations:

$$\frac{D\rho}{Dt} = k_g\rho + \mathcal{D}\nabla^2\rho \,, \tag{3.10a}$$

$$\frac{D(\rho\boldsymbol{v})}{Dt} = \nabla\cdot\boldsymbol{\sigma} - \xi\rho\boldsymbol{v} \,, \tag{3.10b}$$

$$\frac{D\boldsymbol{Q}}{Dt} = \lambda S\boldsymbol{u} + \boldsymbol{Q}\cdot\boldsymbol{\omega} - \boldsymbol{\omega}\cdot\boldsymbol{Q} + \gamma^{-1}\boldsymbol{H} \,, \tag{3.10c}$$

modified from Eqs. 2.4, with an additional term $k_g\rho$ (in Eq. 3.10a) representing an exponential growth of the colony total mass at a rate k_g (proportional to the length extension rate g used in section 3.1). Further details of the continuum theory can be found in section 2.2. The internal stresses $\boldsymbol{\sigma}$ is similar to that of an active nematics:

$$\boldsymbol{\sigma} = -p\boldsymbol{I} + \alpha\boldsymbol{Q} - \lambda S\boldsymbol{H} + \boldsymbol{Q}\cdot\boldsymbol{H} - \boldsymbol{H}\cdot\boldsymbol{Q} \,, \tag{3.11}$$

where the second term represents the extensile active stress introduced by the cell growth. Now, consistent with the results of our hard-rod model presented in section 3.2, we encode a specific density dependence in the quantities p, α, and $L_1 \sim k_F$. We introduce the packing fraction $\phi = \rho/\rho_c$, where ρ_c is the density at which cells become closely packed and start to transmit stress. Based on these considerations, we set

$$p = p_0\,(\phi - 1) \,, \quad \alpha = -\alpha_0\,(\phi - 1) \,, \quad L_1 = k_{F0}\,(\phi - 1) \,,$$

where p_0, α_0, and k_{F0} are positive constants. Furthermore, we take $\alpha_0 \sim k_g$ and keep p_0 independent of k_g, based on the results summarized in Fig. 3.5b. In our system of growing cells, orientational order is driven uniquely by the steric repulsion, and the system transitions to a nematic phase for large enough densities. We set $A_2 = A_0(\rho^* - \rho)/2$ and $A_4 = A_0\rho$, so the system has an equilibrium order parameter $S = \sqrt{1 - \rho^*/\rho}$, with a critical density ρ^*; hence, the colony is disordered for densities $\rho < \rho^*$, and it is nematic for $\rho > \rho^*$. In the following, we assume $\rho_c > \rho^*$ to reflect the earlier observation that, at very low density (i.e., at the boundary of the colony), the contact forces tend to reorient cells rather than compress them.

Equations 3.10 have been numerically solved using a finite difference approach on a 351×351 collocated grid. Figure 3.8 shows a typical configuration obtained for sufficiently large growth rates, in terms of the nematic

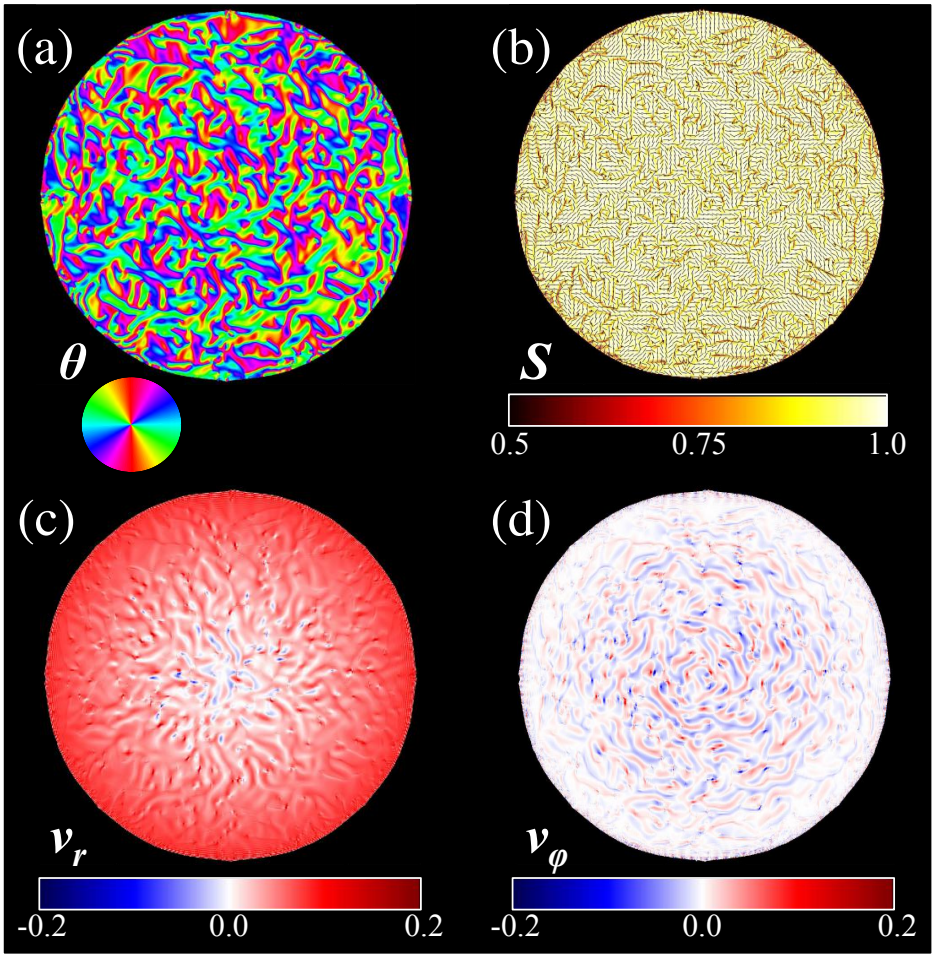

Figure 3.8. Continuous Model. (a) Snapshot of a typical configuration obtained from a numerical integration of Eqs. 3.10. Displayed here is the angle between the nematic director and the x axis, colored using the same color scheme as in Fig. 3.1. (b) Director field (lines) superimposed on a color map of the nematic order parameter S. As for the hard-rod model, nematic order is approximatively uniform except at the boundary of the domains. (c) Radial and (d) tangent components of the velocity field, v_r and v_φ. Along the radial direction, the flow is predominantly expansive because of the cell growth. On the other hand, there is no net circulation along the tangential direction.

director and order parameter (Fig. 3.8a and 3.8b) and velocity field (Fig. 3.8c and 3.8d). As for our hard-rod models, these consist of an ensemble of randomly oriented nematic domains, whose characteristic area remains uniform in the bulk of the colony. In order to make a quantitative comparison between our discrete and continuous models, we reconstruct the geometrical properties of the microdomains based on the following criterion. Given the orientation $\theta = \arctan(Q_{xy}/Q_{xx})/2$ of the nematic director, we define Θ as the coarse-grained θ field in which all values are sorted into bins; e.g., $2(n-1)\pi/m \leq \theta < 2n\pi/m \implies \Theta = (2n-1)\pi/m$ for $n = 1, 2, \ldots, m$ (with n and m both integers). This divides the colony into domains that can then be identified by labeling the connected components of the resulting two-dimensional matrix. We use a value of $m = 6$ here to reflect a typical θ change between two boundaries in the hard-rod model.

Figure 3.9 summarizes the results obtained from a numerical integration of Eqs. 3.10. As for the hard-rod model, the density decreases monotonically from the center of the colony, consistent with the quadratic law given by Eq. 3.2 (Fig. 3.9a). Here, we demonstrate that such a property originates from the interplay between growth-induced pressure and drag from the substrate. Under this hypothesis and assuming low Reynolds number, from Eq. 3.10b, one can approximate the momentum density in the Darcy-like form $\rho\boldsymbol{v} = -\mu\nabla\rho$, where $\mu = p_0/(\xi\rho_c)$ is a mobility coefficient. Using this relation in Eq. 3.10a yields the following moving boundary value problem for the colony density:

$$\partial_t\rho = \mu\nabla^2\rho + k_g\rho\ , \qquad |\boldsymbol{r}| < |\boldsymbol{R}|\ , \tag{3.12a}$$

$$\rho(\boldsymbol{R}, t) = \rho_c\ , \tag{3.12b}$$

$$\dot{\boldsymbol{R}} = -\mu\rho^{-1}\nabla\rho|_{\boldsymbol{r}=\boldsymbol{R}}\ , \tag{3.12c}$$

where we indicate with $\boldsymbol{R}$ the position of the boundary of the colony and with $\dot{\boldsymbol{R}} = \boldsymbol{v}(\boldsymbol{R})$ its velocity. Because of the circular symmetry of the colony at long times, $\boldsymbol{R} = R\hat{\boldsymbol{r}}$, and Eqs. 3.12 reduce to a Stefan problem with one spatial and one temporal variable [99]. At short times, density and pressure are still roughly uniform across the system, and growth results mainly in a radial expanding flow. Consistent with Eq. 3.10a, if $\rho(r,t) \approx$ const, then $\nabla\cdot\boldsymbol{v} = k_g$. Thus, assuming $v_\varphi = 0$, we get $v_r = k_g r/2$ and $R(t) = R(0)\exp(k_g t/2)$. The long time dynamics, on the other hand, is dominated by the internal diffusive currents. In this regime, $\rho(0,t) \gg \rho_c$

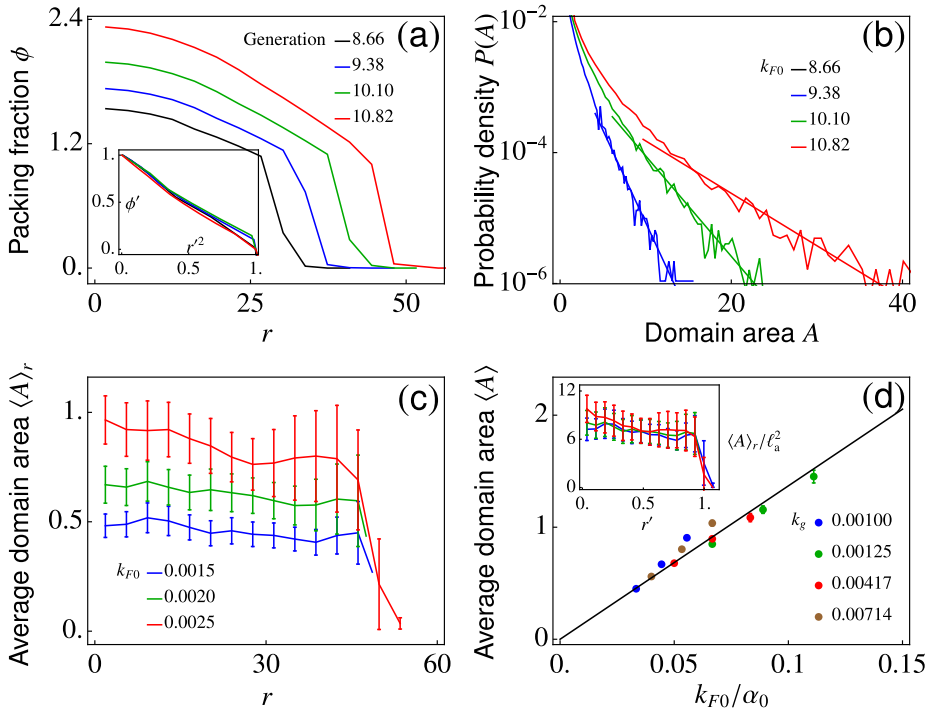

Figure 3.9. Geometrical properties of continuous colonies. (a) Spatial distribution of the packing fraction ($\phi = \rho/\rho_c$) for colonies of different ages, given by their generation. Similar to the hard-rod model, the inset shows that all curves collapse to a single line when ϕ and r are rescaled by $\phi' = [\phi(r) - \phi(R)]/[\phi(0) - \phi(R)]$ and $r' = r/R$. (b) Probability density of the domain area, $P(A)$, for various values of the orientational stiffness k_{F0}. (c) The average domain area at a distance r from the center of the colony. As in the hard-rod model, the typical domain area is uniform across the colony. (d) The average domain area for a colony scales linearly with the squared active length scale $\ell_a^2 = k_F/|\alpha|$. The inset shows that the radial distribution of domain areas can be rescaled by the squared active length scale to the same value. In presenting the results, we use $l = 1/\sqrt{\rho_c}$ as our units of length. We interpret the doubling time $t_g = \log(2)/k_g$ as the time per generation. The simulations were run on a 351×351 grid with the spacing set to 1. They start from a circle of bacteria with density $\rho_0 = 0.1$ and radius 6 grid points and grow to a given total mass, at which point the simulation ends. The (unscaled) parameters used were $\rho^* = 0.005$, $A_0 = 50$, $\rho_c = 0.1$, $\xi = 5$, $P_0 = 10$, $\lambda = 0.1$, and $\zeta = 10$. The two variable parameters are $\alpha_0 =$ (a) 0.225, (b) 0.45, (c) 0.225, and (d) $[0.225, 0.45]$, $k_{F0} =$ (a) 0.25, (b-c) $[0.15, 0.35]$, with $k_g = \alpha_0/25 - 0.0075$. Results presented are based on the average of 50 simulated colonies.

and $R \gg \sqrt{\mu/\kappa_g}$, which is the characteristic length scale associated with Eq. 3.12a. Thus, taking $\rho_c \to 0$ and $R \to \infty$, one can find an analytical solution of Eqs. 3.12 of the form

$$\rho(r,t) = \frac{M_0}{4\pi\mu t} \exp\left(k_g t - \frac{r^2}{4\mu t}\right) , \tag{3.13}$$

under the assumption that $\rho(\boldsymbol{r},0) = M_0\delta(\boldsymbol{r})$. Thus, in agreement with Eq. 3.2, we have

$$\frac{\rho(r,t)}{\rho(0,t)} \approx 1 - \left(\frac{r}{R}\right)^2 , \tag{3.14}$$

where, consistently with Eq. 3.12c, we have taken $R = 2\sqrt{\mu t}$. For generic ρ_c and R values, Eqs. 3.12 become analytically intractable; nonetheless, our numerical simulations (Fig. 3.9a) indicate that even the short time dynamics of the density ρ is ultimately dominated by a similar competition between growth and drag.

The geometrical properties of the nematic microdomains are summarized in Figs. 3.9b–d. The area of the domains is exponentially distributed (Fig. 3.9b), and its average $\langle A \rangle_r$ is uniform across the colony (Fig. 3.9c) and proportional to the squared active length scale as demanded by Eq. 3.9 (Fig. 3.9d). The agreement between our discrete and continuous models not only validates our interpretation of the results presented in Secs. 3.1 and 3.2 but also demonstrates that the a growing bacterial colony can be described by the hydrodynamics theory of active nematics. On the one hand, this provides an efficient method to simulate growing bacterial colonies. Unlike discrete particle methods (including that used in section 3.1), our hydrodynamic approach does not suffer from the prohibitive slowdown caused by the exponential increase in the particle number, and it can be naturally generalized to other geometries and boundary conditions. On the other hand, this approach offers another prototype, i.e., growing bacterial colonies, for the experimental and theoretical study of active matter.

3.4 Experiment on *E. Coli* microcolony

To further test the significance of our results, we compare our theoretical predictions with experiments on a nonmotile strain of *E coli* NCM 3722 delta-motA. The cell-to-colony growth was observed on a 2-mm-thick layer of agarose gel uniformly mixed with LB, a nutritionally rich

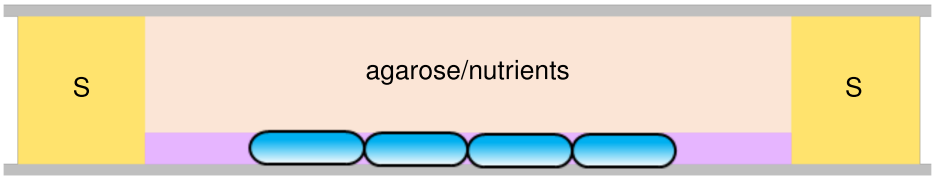

Figure 3.10. Lateral view of the micro-environment used in the bacterial growth experiments. *Escherichia coli* was grown on an agarose layer (pale pink) replete with Lysogeny broth (LB). The nutrient-rich agarose layer was sandwiched between two glass slides (grey hue) and enclosed with a 2-mm-thick neoprene spacer (marked as "S" in yellow). The cells (shown in blue) were imaged from below using time-lapse phase-contrast microscopy.

medium commonly used for growing bacteria (Fig. 3.10). The nutrient layer was sandwiched between two glass slides and enclosed within a 2-mm-thick neoprene spacer. The cells were imaged from below using time-lapse phase-contrast microscopy. For each experiment, we cultured the cells overnight in the LB medium. A dilute concentration of this culture was used to spot single bacterium on the agarose surface, which subsequently grew into colonies. For each experiment, *E. coli* was cultured overnight in the LB medium at 25 °C. A dilute concentration of this culture was then used to spot single bacterium on the agarose surface, which served as nucleating sites for subsequent colonies.

Under the given experimental conditions, the average doubling time of bacteria was 43.5 ± 2.2 minutes (doubling time for each replicate in minutes was 42.86, 45.89, 44.42, and 40.76). Cells in the colony were 0.9 ± 0.1 μm wide, while the average cell length varied among different colonies. The four replicates considered here were obtained under room-temperature conditions, which was stable at approximately 22° during the course of the measurements. The variability in the cell division lengths is frequently observed within colonies growing under similar conditions, potentially because of the inherent variability in the probability of growth itself (also known as phenotypic heterogeneity) [100]. Statistics were measured over four independent colonies. The nutrient-rich agarose layer was thus sufficiently thicker than the bacterial monolayer ($\simeq 1$ μm), which ensured constant availability of nutrients during the entire duration of the experiments.

We used time-lapse phase-contrast microscopy to visualize the growth of two-dimensional bacterial colonies (Fig. 3.1a–d). Images were acquired

using an Andor iXon Ultra 897 camera (8 μm/px) coupled to an inverted microscope (Nikon TE2000) with a 40$\times$ air objective (additional 1.5$\times$ magnification was used in some cases). This gave us a resolution of 0.2 μm (0.13 μm with additional 1.5$\times$ magnification). For a 4-μm-long cell, this resulted in a resolution of 20 pixels/cell. Using subpixel resolution (achieved by Gaussian interpolation), we could further improve this by a factor 2, which provided us with sufficient resolution to reliably detect and segment single cells. As checks, we analyzed the correct segmentation area over the entire segmented area (true positive rate) and, as a complementary parameter, looked at the false-positive rates. Prior to time-lapse image acquisition, we identified and recorded multiple spots on the agarose layer where single bacterium was present. The microscope was automated to scan these prerecorded coordinates and to acquire, every 3 minutes, the images of gradually growing bacterial colonies. By recording the phase-contrast images over hours, we acquired the necessary data for quantifying growing bacterial colonies. We analyzed the phase contrast images to extract the dimensions (length and width), position (centroid), and the orientation of each cell using intensity thresholding routines available through open source image analysis software ImageJ. Upon extraction of the cell dimensions, and the corresponding centroids and orientations, we generated orientation maps of the colony using MATLAB (MathWorks). All experiments were designed and conducted by Anupam Sengupta, while analyses of experimental data were done by Zhihong You.

Four independent colonies were cultured under the same experimental conditions as specified in the previous section. Despite their approximately similar doubling time, variance in their growth rates (rate of elongation) was quite significant, as was the variance in their division lengths. Figures 3.11a and 3.11b show two examples of proliferating colonies of cells, each with different division lengths and, hence, different cell aspect ratios. Like in the simulations, cells self-organize into nematic domains of different sizes and shapes, and the typical domain area increases with the cell aspect ratio. Along the colony boundary, the cells are preferentially oriented along the tangential direction, whereas in the bulk, the domains are isotropically oriented (insets in Fig. 3.11).

For the strain of bacteria we used, the division rate (or doubling time) is constant at a given temperature; hence, the growth rate (rate of elongation) is approximately proportional to the cell aspect ratio [55]. It is thus difficult to vary the growth rate and the cell aspect ratio independently

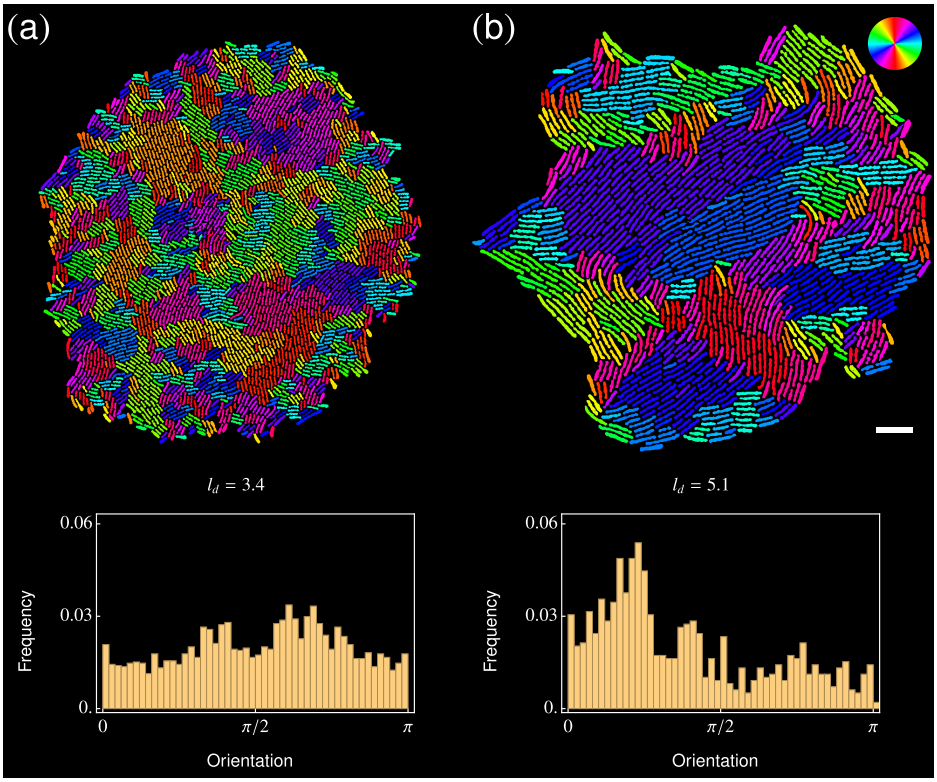

Figure 3.11. Snapshots of two-dimensional bacterial colonies with division lengths (a) $l_d = 3.4$ and (b) $l_d = 5.1$. Cells are color-coded with the same method as in Fig. 3.1, and the scale bar corresponds to 10 μm. The insets show the normalized frequencies of cell orientations of the corresponding colonies.

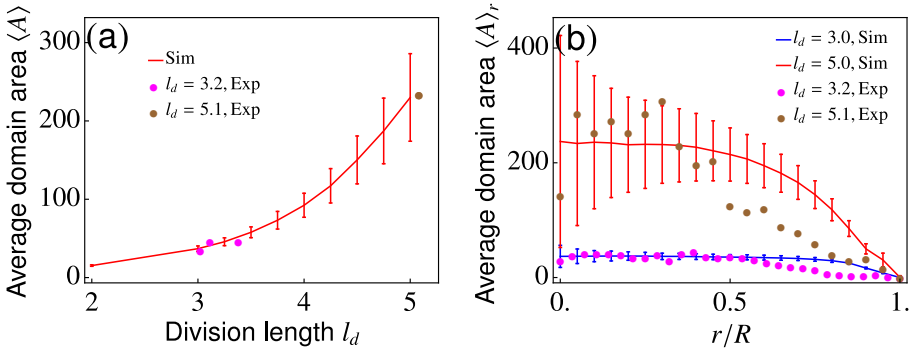

Figure 3.12. Comparisons between the experiments and the simulations in (a) average domain area $\langle A \rangle$ as a function of division length l_d, (b) spatial distribution of domain area $\langle A \rangle_r$. Data from four independent colonies in the experiment are analyzed, each corresponding to a dot in panel (a). Magenta dots represent results from three experimental colonies ($l_d = 3.4, 3.1, 3.0$ and $g = 3.1\mu$m/h, 2.9μm/h, 2.8μm/h in physical units) with an average division length $l_d = 3.2$, and the brown dots are from one experimental colony with division length $l_d = 5.1$ and growth rate $g = 4.2\mu$m/h in physical units. The simulation data, represented by solid lines, are the same as those shown in Figs. 3.3a–c, i.e., with a growth rate $g = 0.0002$ (or 4μm/h in physical units).

in our experiment, as done in the simulations. However, as we can see from Figs. 3.3c and 3.3d, the variation of domain size is more sensitive to the division length l_d, if l_d and g are linearly related. For this reason, we compare the experimental results with those of a fixed growth rate from the MD simulations.

Figure 3.12a shows the average domain sizes of the four colonies (each represented by a dot) as a function of the division length l_d. We can see that the average domain sizes $\langle A \rangle$ in experiments fall well within the region predicted by our simulations. The spatial distribution of domain size, i.e., $\langle A \rangle_r$, is approximately constant for $l_d = 3.2$ (magenta dots in Fig. 3.12b), and overlaps well with that for $l_d = 3.0$ from the simulations. Here, $\langle A \rangle_r$ for $l_d = 5.1$ (brown dots in Fig. 3.12b) is also in the expected region. Note that $\langle A \rangle_r$ drops at a smaller r/R in the experiments. This is because the colony radius R is smaller in the experiment, and the relative thickness of the boundary layer, which contains smaller domains, is larger.

Because of the limited statistics, our experimental results do not allows us to formulate conclusive statements. However, the quantitative agree-

ment between the experiment and theory, is encouraging in suggesting that some of the geometrical and mechanical aspects of bacterial microcolonies can indeed be conceptualized in the framework of active liquid crystals.

3.5 Discussion and conclusion

Sessile bacteria communities have the extraordinary ability to colonize a variety of surfaces, even in the presence of nonoptimal environmental conditions. Such a process typically starts from a few or even a single cell that elongates and eventually divides at a constant rate, and this gives rise to highly complex two-dimensional and three-dimensional structures consisting of tightly packed and partially ordered cells. Colonies originating from a single bacterium initially develop in the form of a flat and circularly symmetric monolayer and, after reaching a critical population, invade the three-dimensional space forming stacks of concentric disk-shaped layers [61, 56]. While in the monolayer form, bacterial colonies exhibit prominent nematic order; however, this does not propagate across the colony, and it remains confined to a set of microscopic domains of coaligned cells. Using molecular dynamics simulations, continuous modeling and, to a limited extent, experiments on *E. coli* microcolonies, we have demonstrated that these domains originate from the interplay of two competing forces. On the one hand, the steric forces between neighboring cells favor alignment. On the other hand, the extensile active stresses due to growth tend to distort the system and disrupt the local orientational order. This results in an exponential distribution of the domain area, with a characteristic length scale $\ell_{\mathrm{a}} = \sqrt{k_F/|\alpha|}$, where k_F is the orientational stiffness of the nematic domains and α the magnitude of the deviatoric active stress.

Previous studies have shown theoretically that random cell division in cellular monolayers can potentially induce an extensile active stress [63, 87]. By modeling the growing cellular monolayers as nematic liquid crystals, and coupling the nematic tensor $\boldsymbol{Q}$ with the local cell concentration c, they demonstrated that random cell division could locally increase the cell concentration and, through the $\boldsymbol{Q}$ coupling, drive a corresponding increase in the local nematic order. Changes in the local nematic order lead to the variations in the molecular field $\boldsymbol{H}$, and subsequently generate an extensile active stress of the form $\alpha\boldsymbol{Q}$. These results, though interesting, are grounded on the specifically designed yet unjustified coupling

between $\boldsymbol{Q}$ and the cell concentration c, as well as the fact that cell division has to be randomized in both space and time. In addition, works on sessile bacterial colony also revealed, in a qualitative picture, that cell growth could lead to an axial compression of cells, which could trigger a buckling instability of cell orientation, either in colonies confined in a straight channel [59], or at the interface between different species [53]. Here in this chapter, we systematically study the mechanical effects of cell growth in a freely expanding monolayer. With quantitative measurements and mathematical derivations, we demonstrate that cell growth can differentiate the normal components of the internal stress which, upon rearrangement, contains explicitly an extensile active stress $\alpha\boldsymbol{Q}$. The hydrodynamic theory introduced here, can then be used as a comprehensive framework to study the interplay among mechanical stresses, cell orientation, and the flow of cells, in growing bacterial colonies.

In addition, the present work allows an accurate description of the chaotic dynamics with a number of experimentally testable predictions, such as the exponential distribution of the domain area, summarized by Eq. 3.1, and the dependence of the average domain area on the cell aspect ratio and growth rate (Figs. 3.3c and 3.3d). The identification of the active length scale ℓ_{a} offers a coherent interpretation of the collective behavior of the freely expanding monolayer. As active nematic liquid crystals, colonies of nonmotile duplicating bacteria are expected to be found in either an ordered or disordered state depending on the ratio between ℓ_{a} and the colony size R. During the initial expansion ($R \ll \ell_{\mathrm{a}}$), the colony develops a highly aligned state, as the restoring forces arising in response to the elastic distortions outweigh the growth-induced active forces. Consequently, the collective growth of cells along the aligned direction results in an elongated shape of the colony (Figs. 3.1f and 3.1j). For a large colony ($R \gg \ell_{\mathrm{a}}$), on the other hand, the system is orientationally disordered and dynamically chaotic. The absence of preferred orientation renders the colony morphology isotropic (Figs. 3.1h and 3.1l).

Even though cell morphology is one of the most well-documented phenotypic traits of microorganisms, its role as a functional trait in microbial ecology and evolution has received little attention [101]. The spontaneous creation of microdomains during the initial stages of colony growth presents a remarkable setting, one in which *nonmotile* bacterial cells collectively lead to *emergent motility* within the colony, as visualized in the chaotic fracture and coarsening dynamics of the nematic domains. Con-

sequently, this interplay between growth-induced stresses and phenotypic stiffness of the participating cells introduces a novel angle to the transport and material attributes of such biologically active matter. Future studies on emergent motility within colonies of nonmotile cells, both in experiments and theory, are expected to contribute to a comprehensive biomechanical picture, highlighting the activity-driven cell-cell communications that precede biofilm formation. Finally, the results presented here are general and can be extended beyond bacterial communities, for instance, to study mammalian cells, many of which exist as nonmotile elongated phenotypes [102].

Chapter 4

Confinement-induced self-organization

In chapter 3, we have seen that in freely expanding bacterial colonies, competition between the growth-induced active stress and the passive elastic forces originating from cell-cell steric repulsion dominates the dynamics of the system and gives rise to randomly oriented nematic domains as well as turbulent cellular flows. In contrast, when the monolayered colony is confined laterally, this wild, chaotic behavior is replaced by a disciplined and ordered arrangement: cells collectively align with the confinement wall and a laminar-like flow emerges as a consequence of cell growth. This has been observed in various experiments and computer simulations [38, 51, 55, 59, 60]. A beautiful experiment was performed by Volfson *et al.*, where non-motile, rod-shaped bacteria were grown in a straight microfluidic channel with an outlet on both ends (Fig. 1.3) [38]. Initially, a few cells are placed at random locations in the channel. As the cells grow and duplicate, various micro-colonies arise, in which local nematic order can be found, but the system is globally isotropic (Fig. 1.3A). Immediately after the colony fills the channel, a global nematic order is developed, where cells collectively align with the channel wall (Figs. 1.3C and 4.1A).

This global alignment of cells with the confinement walls has very important biological implications [51]. If cells are randomly oriented, cell elongation toward the wall will generate large mechanical stress, which can significantly reduce the fitness of the cells [51]. In the case of collective alignment with the wall, all cells are pushing their neighbors toward the outlets. By doing so, not only can the growth-induced stress be released efficiently, but also a strong outward flow of cells is generated from the collective pushing, allowing cells to efficiently escape from the trap, and reduce the crowdedness of the whole colony [51]. In addition, the strong anisotropy in the globally aligned state can lead to a dramatic reduction of its tortuosity and enhance the nutrient diffusion in the preferred direction,

thus facilitating the nutrient intake of cells in bulk of the colony [51].

In a long channel, however, this globally ordered state becomes unstable through a buckling transition, where disordered nematic domains are created at the center of the channel and the system becomes partially ordered (Figs. 4.1C and 4.1D) [38, 59, 60]. This buckling instability was found to be triggered by the growth-induced axial compression, and can be captured by an elegant theory where the colony is modeled as a continuum uniaxial elastic medium [59]. Computer simulations of proliferating rods also revealed more sophisticated dynamics during the buckling transition, and how the transition was mediated by the cell growth rate, the cell aspect ratio, and the sliding friction from the substrate [60].

Whereas the understanding of the transition from global alignment to partial order is well, the mechanism of the development of global nematic order in the initial stage is still not very conclusive, despite of the crucial influence it has on the fitness of the bacterial colony. Two theories have been proposed to explain this phenomenon. Volfson *et al.* found that the global alignment of cells appeared simutaneously with the growth-induced expansion flow toward the outlets [38]. In addition, the global orientation of cells coincides with the direction of the expansion flow, i.e., parallel to the chamber wall (Figs. 4.1A and 4.1B). Based on these findings, they conjectured that the global alignment was driven by the expansion flow. A phenomenological theory was developed based on the hydrodynamic equations of nematic liquid crystals, where the nematic order parameter S was coupled to the flow gradient, which, when nonzero, favored perfect nematic order, i.e. $S = 1$. This theory can qualitatively reproduce the results from the experiments and the simulations, but no reasoning was provided to justify the coupling between the flow and the nematic order parameter S, which was the core of the theory. Most recently, a stochastic theory was proposed to explain the global alignment [103]. The authors modeled cell growth in a rectangular microfluidic trap as a spatial Moran process, and concluded that the wall alignment could drive the whole colony to align with the long axis of the trap. However, these results were based on two premises–asymmetric cell growth and the specific spatial dependence of cell growth rate. Specifically, a cell tends to grow more toward the nearest boundary than the opposite direction (asymmetry), and the grow rate of a cell decreases with its distance to the boundary (spatial dependence). These assumptions, if realistic, are by no means indispensable, according to the previous experiments and simulations [38,

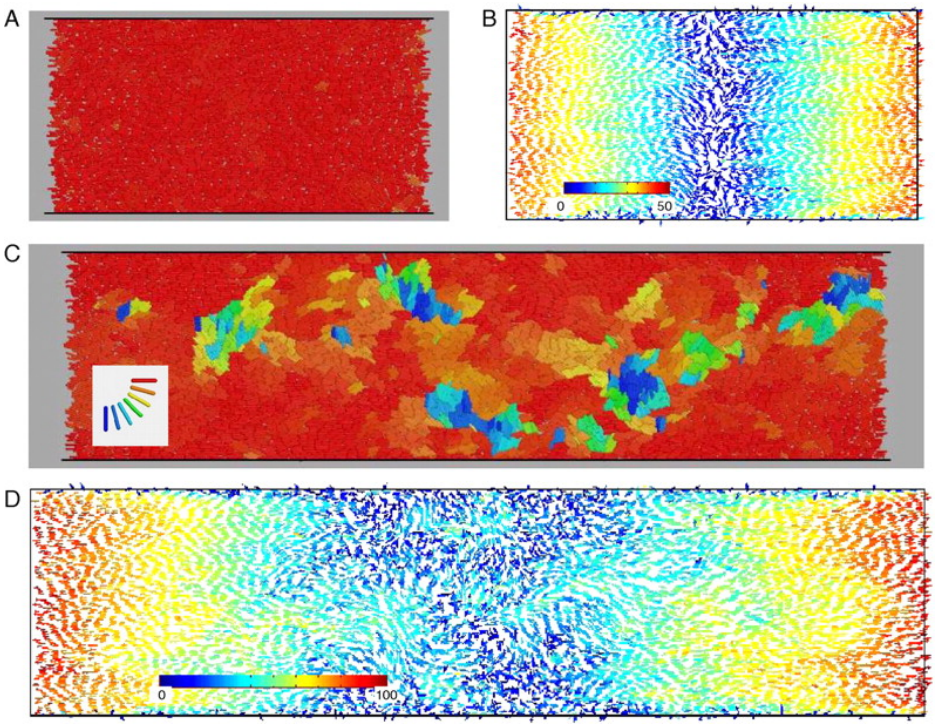

Figure 4.1. Discrete element simulations of the ordering dynamics in channels with different aspect ratios. (A) Orientation of individual cells (color-coded) in a short channel. (B) Velocity field for the same case as in A, where unit velocity vectors show the velocity direction for each cell and colors (from blue to red) correspond to the velocity magnitude (from low to high). (C) The same as A, but for a twice longer channel. Disordered nematic domains are constantly created in the middle of the channel and advected by the flow toward the open boundaries. (D) Velocity field for the long channel. The flow is no longer laminar, and there is no apparent correlation between orientation and velocity magnitude. Adapted from [38].

51, 55, 59, 60].

In this chapter, we demonstrate that the global alignment of cells is not triggered by either of these mechanisms, but instead is driven by the globally anisotropic stress emerging as a consequence of cell growth and confinement. Using computer simulations of the hard-rod model, we find that cell growth gives rise to a persistent accumulation of internal stress. While the stress components in the free direction can be efficiently released due to the expansion flow of cells toward the outlets, the presence of confinement prohibits cell motion in the confined direction, and leads to a build up of the corresponding stress components. As a consequence, a globally anisotropic stress emerges, where the stress components in the confined direction are larger than their orthogonal counterparts. This anisotropic stress can destabilize the vertical alignment (i.e. cells being vertical to the confinement walls), while making the horizontal alignment more stable and, therefore, drives cells to align with the direction of minimal stress which, in the case of a straight channel, is parallel to the wall. These discoveries not only shed new light on the roles of confinement and mechanical stress on the self-organization of growing bacterial colonies and more generally the interplay between orientation and stress in nematic liquid crystals, but also provide a potential way to control growing bacterial colonies with confinement.

4.1 Phenomena

We use the hard-rod model introduced in section 2.1 and constrain the colony in the xy–plane as we did in chapter 3. All control parameters in chapter 3 apply to this chapter as well: $d_0 = 1\,\mu$m, $Y_c = 4$ MPa, and $\zeta = 200$ Pa h. We confine the growing colony with a rectangular box of dimension $L_x \times L_y$, and centered at the origin $[0, 0]$. Specifically, two horizontal confinement boundaries of length L_x are placed at $[0, -L_y/2]$ and $[0, L_y/2]$, respectively. The horizontal boundaries can represent either impenetrable rigid walls, interacting stericly with the cells or, periodic boundaries, which make the system periodic in the y direction. Similar to the previous studies [38, 51, 55, 59, 60], we arrange two vertical absorbing boundaries at $[-L_x/2, 0]$ and $[L_x/2, 0]$, as the outlets of the channel. Cells overlapping with the absorbing boundaries will be removed from the system. This allows continuous growth of cells in the channel without overcrowding and jamming of cell motion. We call the extent of channel

in x, L_x, the width of the channel, and that in y, L_y, the channel height. In all snapshots shown in this chapter, we use solid white lines to represent the rigid walls, dashed white lines the periodic boundaries, and red solid lines the absorbing boundaries. All simulations start with a cell at the origin, with random orientation. In this chapter, we fix the cell growth rate at $g = 2\mu$m/h and the division length at $l_d = 2\mu$m, and focus on the effects of boundary condition and channel geometry on the colony dynamics. SI units are used in this chapter.

We first study growing bacterial colonies confined by rigid walls. Figures 4.2a–i show snapshots at typical stages of a growing colony under this confinement. As expected, a steady state of global nematic order is finally reached, where cells mostly align in the horizontal direction. An obvious conjecture is that the global alignment is driven by boundary anchoring,

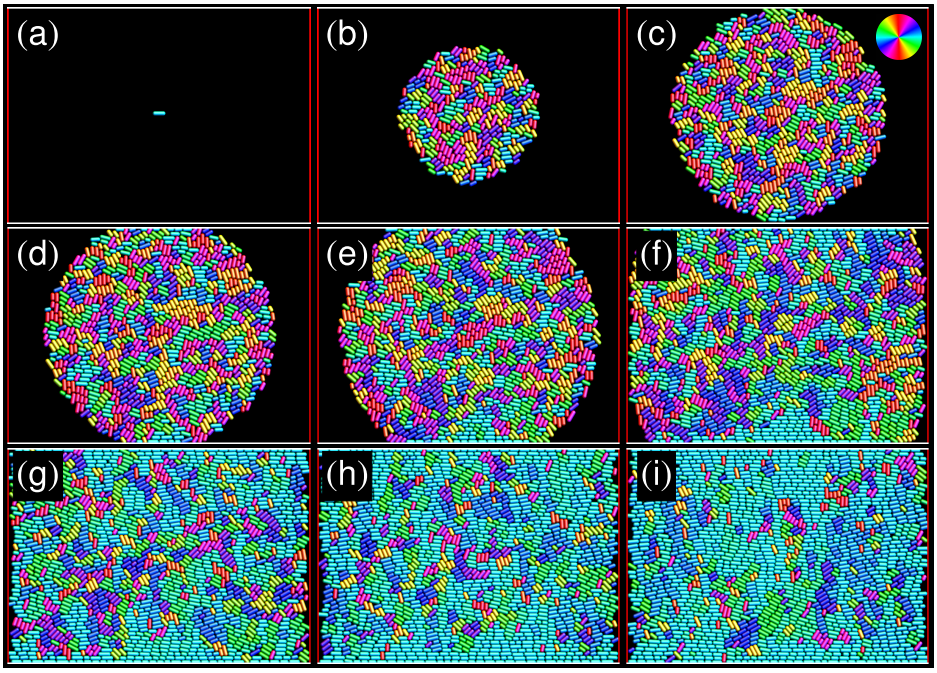

Figure 4.2. Snapshots at different time points of a growing colony subject to rigid wall confinement in the y direction. The horizontal white lines represent the rigid walls, and the vertical red lines the absorbing boundaries. Cells are color coded by their orientation, as indicated by the color wheel in (c). The simulation parameters are: $L_x = 70$ μm, $L_y = 50$ μm.

as proposed in Ref. [103]. Indeed, steric repulsion from the rigid walls can generate net torques on cells nearby, and enforce them to be parallel to the wall. This effect is usually referred to as *parallel boundary anchoring* in the theory of liquid crystal [76]. In addition, neighboring cells also tend to align with each other as we showed in chapter 3. The parallel anchoring can then propagate into the bulk of the colony, and enforce the whole colony to be aligned with the wall. This boundary driven alignment is commonly seen in nematic systems [76], and was also observed recently in cellular monolayers (Fig. 4.3) [102, 104].

Although simple and intuitive, this explanation turns out to be inadequate. As shown in Ref. [104], the boundary anchoring can only propagate toward the bulk up to a distance that is proportional to the orientation correlation length. Hence, the global alignment can only appear when

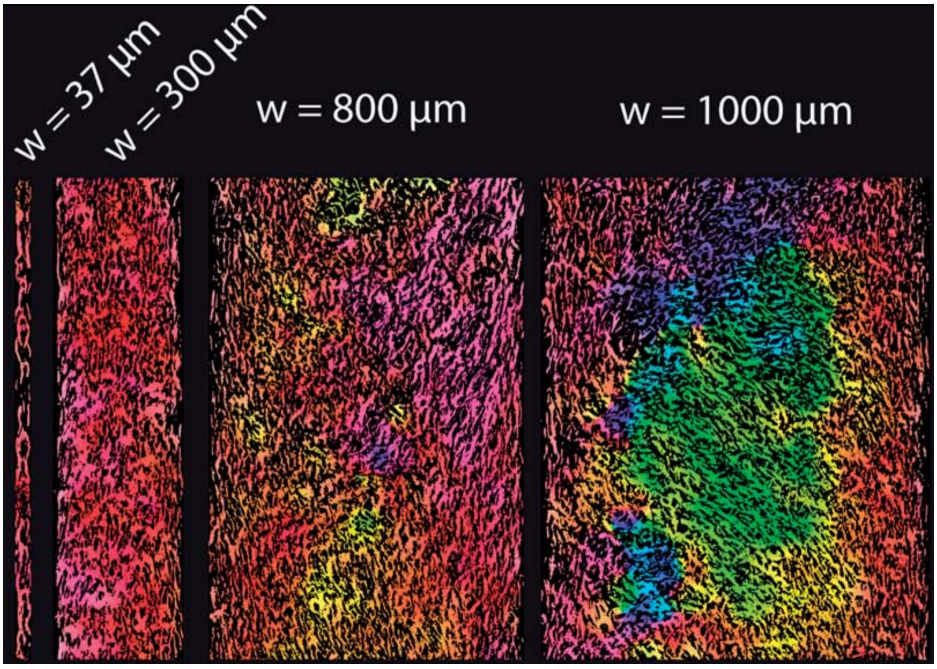

Figure 4.3. Orientation of the cells in stripes of different width at long times. Cells are color coded by their orientation as indicated by the legend on the right hand side. Note the homogeneous orientation at small widths and the patchy aspect at large widths that indicate the presence of well-oriented clusters with a different orientation. Adapted from [104].

the channel height L_y is smaller than this "penetration depth" (Fig. 4.3) [104]. For high channels, wall alignment can be expected within the penetration depth, but the rest of system is globally disordered (Fig. 4.3) [104]. In our case of growing bacterial colonies, as we discussed in chapter 3, the orientation correlation length is mediated by the competing effects of cell aspect ratio and the growth rate. For $l_d = 2$ μm and $g = 2$ μm/h, this correlation length is about a few cell widths (Figs. 4.2b and 4.2c). Indeed, in Figs. 4.2d–f, we do see the boundary alignment stops at a few cell widths from the walls. Therefore, the boundary anchoring by itself is not sufficient to induce horizontal alignment in the whole colony. To further demonstrate this point, we eliminate the boundary anchoring effect by replacing the rigid walls with periodic boundaries. This setup can represent cell growth on a cylindrical surface, provided the effects from the curvature can be ignored. As expected, even without boundary anchoring, the globally horizontal alignment still appears (Figs. 4.4a–i).

Let us now look at the development of the global alignment. Take the periodic case as an example. Initially, the colony can freely expand and is globally isotropic with no preferred orientation, as shown in Figs. 4.4b-d. When the top and the bottom fronts collide on each other, the confinement starts to take effects. At first, only the cells at the front (i.e. close to the periodic boundaries) reorient along the horizontal direction (Fig. 4.4e). Later, there are some disconnected domains in bulk of the colony aligning in the same direction (Fig. 4.4f). Then, these domains expand (Fig. 4.4g), merge (Fig. 4.4h), and finally, global alignment along the horizontal direction is extended to the whole colony (Figs. 4.4i). Similar process can be found in the case of rigid walls (Figs. 4.2a–i). An exception is that the boundary anchoring effect from the rigid walls can facilitate the global alignment to some extent. For this reason, the global alignment develops more rapidly and the steady states are more ordered in presence of rigid walls. From this perspective, the emergence of global alignment is more like a percolation process emerging from all over the colony than a propagation process initiated at the boundary [105]. These results suggest that the confinement of cell motion must have triggered some mechanical effects that can drive cells to align in the horizontal direction.

A strong candidate among the possible mechanical effects is the flow alignment of the nematic director. As demonstrated by Volfson *et al.*, the combined effects of confinement and cell growth give rise to an expansion flow of cells, which arises simutaneously with the global alignment, and

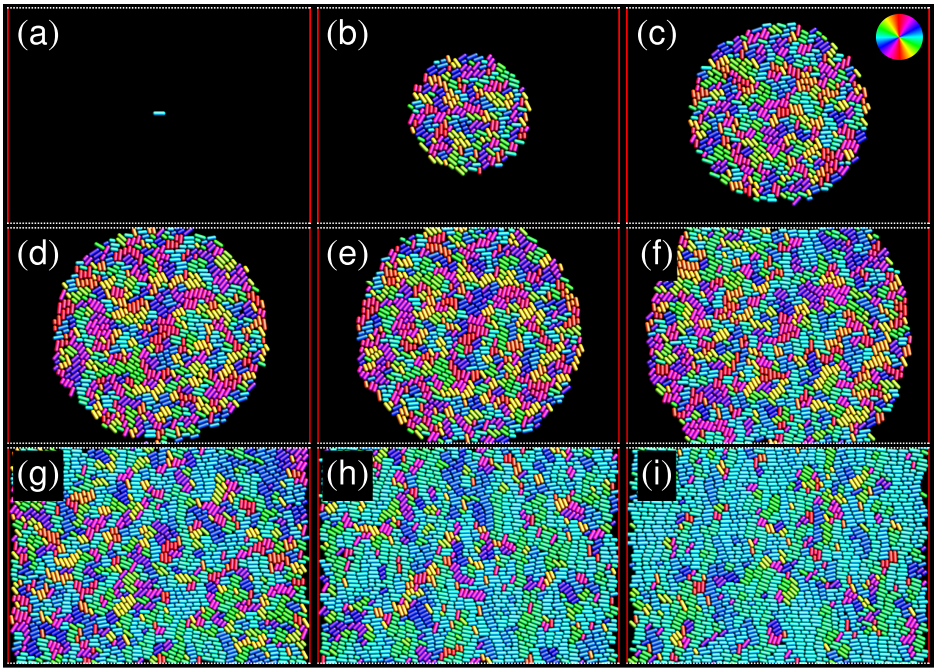

Figure 4.4. Snapshots at different time points of a growing colony subject to periodic confinement in the y direction, represented by the dashed white lines. Cells are color coded by their orientation, as indicated by the color wheel in (c). The simulation parameters are: $L_x = 70$ μm, $L_y = 50$ μm.

whose direction and gradient both coincide with the orientation of cells (Figs. 4.1A, 4.1B, and 4.5a) [38]. Although the specific flow–orientation coupling in their theory is different from the "standard" flow alignment in nematic liquid crystals, it is similar in spirit: flow velocity gradient can drive nematic order. To explain this, imagine a steady laminar flow $\boldsymbol{v} = v_x(x)\hat{\boldsymbol{x}}$ in the channel, with a constant flow gradient in x: $\partial_x v_x = C > 0$. In such case, the vorticity tensor $\boldsymbol{\omega}$ vanishes, and Eq. 2.4c can be simplified as

$$\frac{DQ_{xx}}{Dt} = \lambda SC + \gamma^{-1} H_{xx}, \tag{4.1a}$$

$$\frac{DQ_{xy}}{Dt} = \gamma^{-1} H_{xy}. \tag{4.1b}$$

Equations 4.1 indicate the tendency of nematic director to align with the flow gradient. Specifically, the term λSC provides a positive feed to

$Q_{xx} \equiv S(n_x^2 - 1/2)$ and tends to increases it, while there's no such term for $Q_{xy} \equiv S n_x n_y$. Overall, this can drive Q_{xx} toward the maximum value of $1/2$, corresponding to a perfect nematic order $S = 1$, with a horizontally aligned director $\boldsymbol{n} = \hat{\boldsymbol{x}}$.

To characterize quantitatively the relations between the flow and the cell orientation, we define an *alignment parameter* of cell orientation

$$\Phi = 2\left[\left\langle p_x^2 \right\rangle - \frac{1}{2}\right], \tag{4.2}$$

where $\boldsymbol{p} = [p_x, p_y]$ is the orientation of each cell and $\langle\cdot\rangle$ represents an average over all cells in the region concerned. Defined in this way, Φ quantifies the degree of alignment of cells with the x-axis: $\Phi = 1$ when all cells are parallel to $\hat{\boldsymbol{x}}$; $\Phi = 0$ when they are randomly oriented; $\Phi = -1$ if they all parallel to $\hat{\boldsymbol{y}}$. Similarly, the alignment parameter of flow can be defined as

$$\Phi_v = 2\left[\left\langle (v_x/|\boldsymbol{v}|)^2 \right\rangle - \frac{1}{2}\right], \tag{4.3}$$

which again, quantifies the alignment of flow with the x-axis in the same way. Figures 4.5c–e show the time evolution of Φ, Φ_v, and the flow gradient $\partial_x v_x$, in a periodically confined colony as well as a freely expanding one. We focus on different regions in the two colonies. In the confined colony, we are interested in the region where the confinement takes effects. We call it region I, and define it as $|x| < D_x/2 - 15$ μm, where D_x is the horizontal extension of the colony and 15 μm the approximate width of the two "unconfined" caps on both sides of the colony (Fig. 4.5a). We denote t_c as the time at which the confinement starts to take effects. Before the colony is confined, i.e., $t < t_c$, cells in region I have no preferential orientation (Fig. 4.5c), and the flow mostly aligns with the y-axis (Fig. 4.5d). After t_c, a rapid reorientation of the flow toward x can be found, accompanied with an amplification of the flow gradient along x (Fig. 4.5e). At the same time, we can see a gradual increase of alignment parameter Φ. These results suggest that the flow alignment might be the dominant mechanism of the global cell alignment. However, comparison with the freely expanding colony demonstrates that it's just a fortuitous coincidence. In a freely expanding colony, because of the rotational symmetry, both flow and its gradient are radial (Fig. 4.5b). This means that if we consider only a narrow sector of the colony, region II for example (defined as $|y| < 5$ μm), the flow field will be similar to that of region I

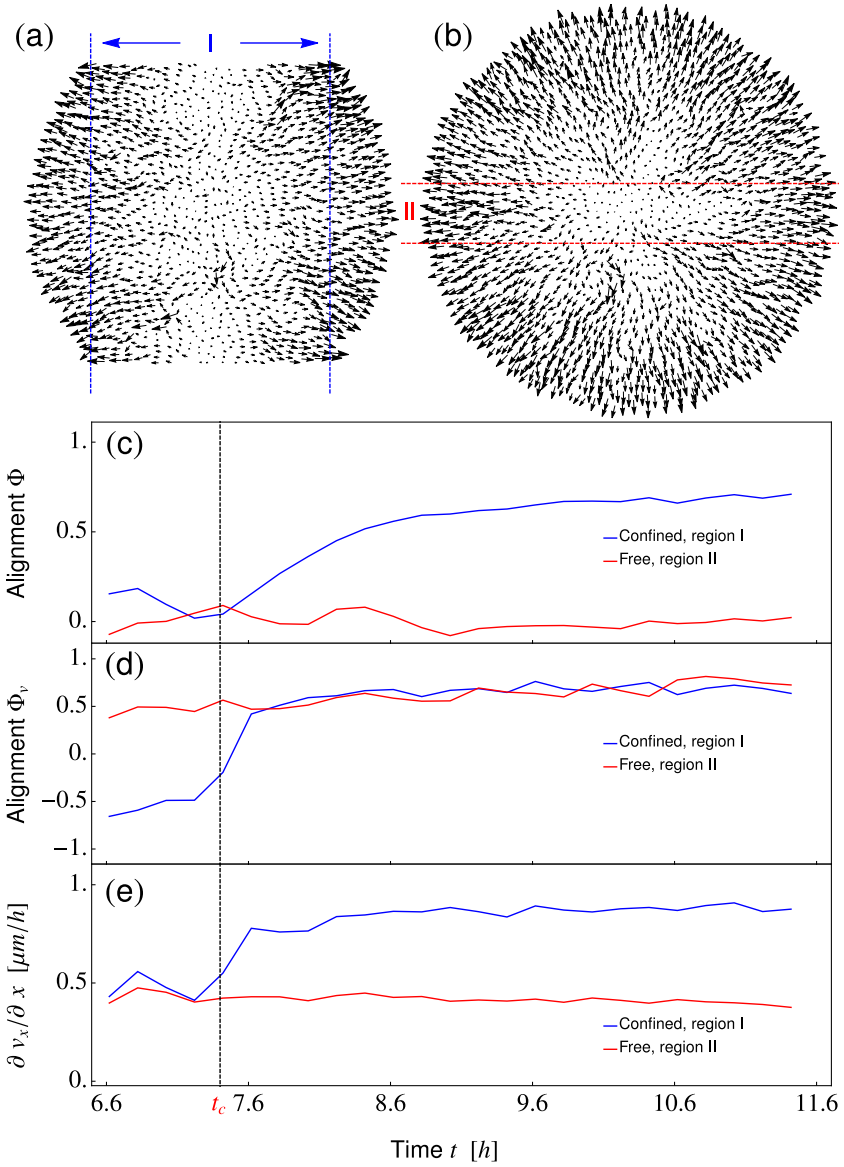

Figure 4.5. (a–b) Flow fields of (a) a periodically confined colony (i.e. the colony shown in Figs. 4.4) and (b) a free colony. Each arrow represents the velocity of the corresponding cell, with an arrow length proportional to the cell speed. (c–e) (c) The orientation alignment parameters, (d) velocity alignment parameters, and (e) the flow gradient, in confined (blue lines) and free (red) colonies. The dashed indicates the time t_c, at which the confinement starts to take effects.

in a confined colony. Indeed, Fig. 4.5d shows the same degree of horizontal alignment of flows in the two regions for $t > t_c$, except that the flow gradient is smaller in the free colony (Fig. 4.5e). If the flow alignment indeed dominates, we would expect cells in region II of the free colony to align horizontally as well, which however, is never found, hence disproves the flow alignment mechanism.

4.2 Stress anisotropy drives cell alignment

In this section, we propose a new mechanism for this global alignment– stress anisotropy drives cell reorientation. As shown in chapter 3, cell growth can increase the local packing fraction, and subsequently the local mechanical stress. In a freely expanding colony, the internal stress is released isotropically by the radial expansion flow (see e.g. Fig. 4.5b) and, consequently, can be decomposed into an isotropic pressure and an extensile active stress, both increasing linearly with the local packing fraction ϕ. We shall see now that the presence of confinement completely changes the growth-induced stress and endows a new role to it.

To reveal the mechanical effects of confinement, we first study the time evolution of internal stress in a confined colony. The stress is measured in the same way as we did in chapter 3, but is expressed in the basis of $\hat{\boldsymbol{x}}$

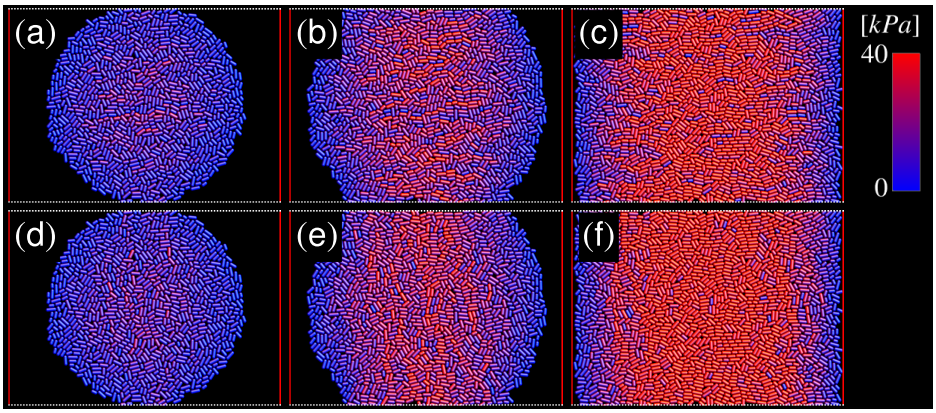

Figure 4.6. Snapshots of the periodically confined colony (i.e. colony shown in Figs. 4.4) at different time points. Cells are color coded by the mechanical stresses they experience: (a-c) $|\sigma_{xx}|$ and (d-f) $|\sigma_{yy}|$. The color map is shown in the legend on the right hand side.

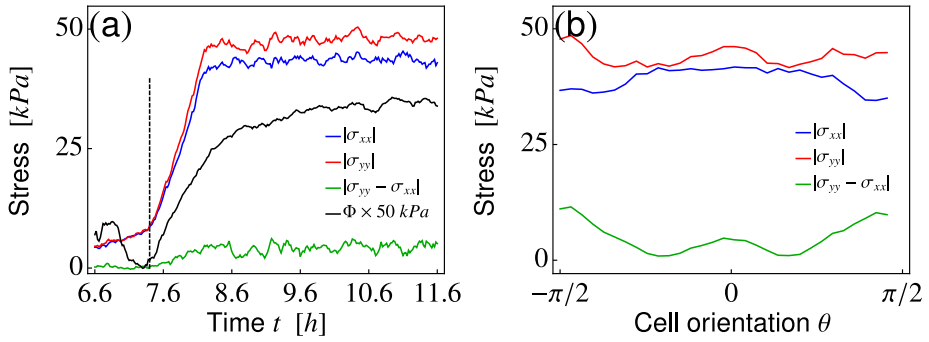

Figure 4.7. (a) Development of the average stresses and the alignment parameter in region I of the periodically confined colony. The black dashed line indicates t_c, the time at which the confinement starts to take effects. Here, we times Φ by 50 kPa in order to directly compare its trend with those of the stresses. (b) Dependence of stress components in region I on the cell orientation θ.

and $\hat{\boldsymbol{y}}$:

$$\boldsymbol{\sigma} = \sigma_{xx}\hat{\boldsymbol{x}}\hat{\boldsymbol{x}} + \sigma_{yy}\hat{\boldsymbol{y}}\hat{\boldsymbol{y}} + \sigma_{xy}(\hat{\boldsymbol{x}}\hat{\boldsymbol{y}} + \hat{\boldsymbol{y}}\hat{\boldsymbol{x}}). \tag{4.4}$$

Similar to the previous chapter, we ignore the shear component σ_{xy} and focus only on the normal components σ_{xx} and σ_{yy}. Figures 4.6a–f show the two normal stresses that each cell experiences at different time points. Upon confinement, both stresses increase dramatically.

To quantify the effects of confinement on the stress, we focus on the average stress of cells in the "confined region", i.e. region I in Fig. 4.5a. As shown in Fig. 4.7a, for $t > t_c$, both stress components increase, but $|\sigma_{yy}|$ on average is larger than $|\sigma_{xx}|$, indicating that the stress is globally anisotropic. This stress anisotropy originates from the combined effects of cell growth and boundary confinement. On the one hand, cell growth provides a persistent feed to the internal stresses. On the other hand, the absence of cell motion in the confined direction prevents the normal stress in y, σ_{yy}, to be released, while the normal stress in x, σ_{xx}, can still be released efficiently. Consequently, $|\sigma_{yy}| > |\sigma_{xx}|$ in the confined region. In addition, the normal stress difference $|\sigma_{yy} - \sigma_{xx}|$ also depends on the cell orientation: $|\sigma_{yy}| > |\sigma_{xx}|$ is valid for all cell orientations, and is maximized at $|\theta| \approx \pi/2$, i.e. for vertically aligned cells (Fig. 4.7b). The orientational dependence of stress components can also be observed in Figs. 4.6b and 4.6e, where larger σ_{xx} and σ_{yy} appear more frequently to horizontal and vertical cells, respectively. This is because the anisotropic cell growth

gives a stress feed of the extensile form $\alpha(\boldsymbol{nn} - 1/2)$, contributing more to the stress components parallel to the cell axis than those in the orthogonal direction. Especially, the growth of vertical cells in the confined region can rapidly increase σ_{yy}, as well as the normal stress difference.

The globally anisotropic stress can be rearranged into an isotropic pressure and a net compression in the y direction:

$$\begin{aligned} \boldsymbol{\sigma} =& \sigma_{xx}\hat{\boldsymbol{x}}\hat{\boldsymbol{x}} + \sigma_{yy}\hat{\boldsymbol{y}}\hat{\boldsymbol{y}} \\ =& \sigma_{xx}\boldsymbol{I} + \beta\hat{\boldsymbol{y}}\hat{\boldsymbol{y}}, \end{aligned} \tag{4.5}$$

where $\beta = (\sigma_{yy} - \sigma_{xx})$ is the magnitude of the net compression. Cell orientation is not directly influenced by the isotropic pressure, but can be regulated by the net compression $\beta\hat{\boldsymbol{y}}\hat{\boldsymbol{y}}$. For vertically aligned cells, the net compression is parallel to the nematic director and, as demonstrated in chapter 3, can bend the director and create a distortion, therefore destabilize the vertical alignment. This effect is further amplified by the fact that vertical cells experience the strongest net compression. On the contrary, the net compression can make the horizontal alignment more stable, because any deviation can induce a large restoring torque to bring the system back to balance. Furthermore, as cells grow and duplicate, the horizontally aligned domains, being more stable, can rapidly expand and cover larger portions of the colony area, which is consistent with what we've found before (Figs. 4.4e–g). Altogether, this specially structured anisotropic stress can drive cells to align horizontally, and we conjecture that it is the dominant mechanism for the global alignment of cells.

To demonstrate that the stress anisotropy is sufficient to drive the global alignment, and gain further insight into the interplay between stress and cell orientation, we perform a simulation of shrinking box. Specifically, we manually arrange a collection of non-growing cells of identical length $l = 2\mu$m in a box that is periodic in both x and y, so no boundary anchoring in such setup. Initially, each cell has a random position and a random orientation. Then we gradually shrink the box in the y direction in order to create a stress anisotropy (Figs. 4.8a–c). This is done by rescaling the y-coordinates of all cells as well as those of the horizontal boundaries by $y(t + \Delta t) = k'y(t)$, where $k' = (L_y - V_y\Delta t)/L_y$ is the rescaling factor and V_y the relative speed of the two horizontal boundaries. Since all y-coordinates are rescaled by the same factor at each time step, the vertical shrinking is homogeneous over the whole system. Note that p_y, the y-th component of the cell orientation, is not rescaled during this process.

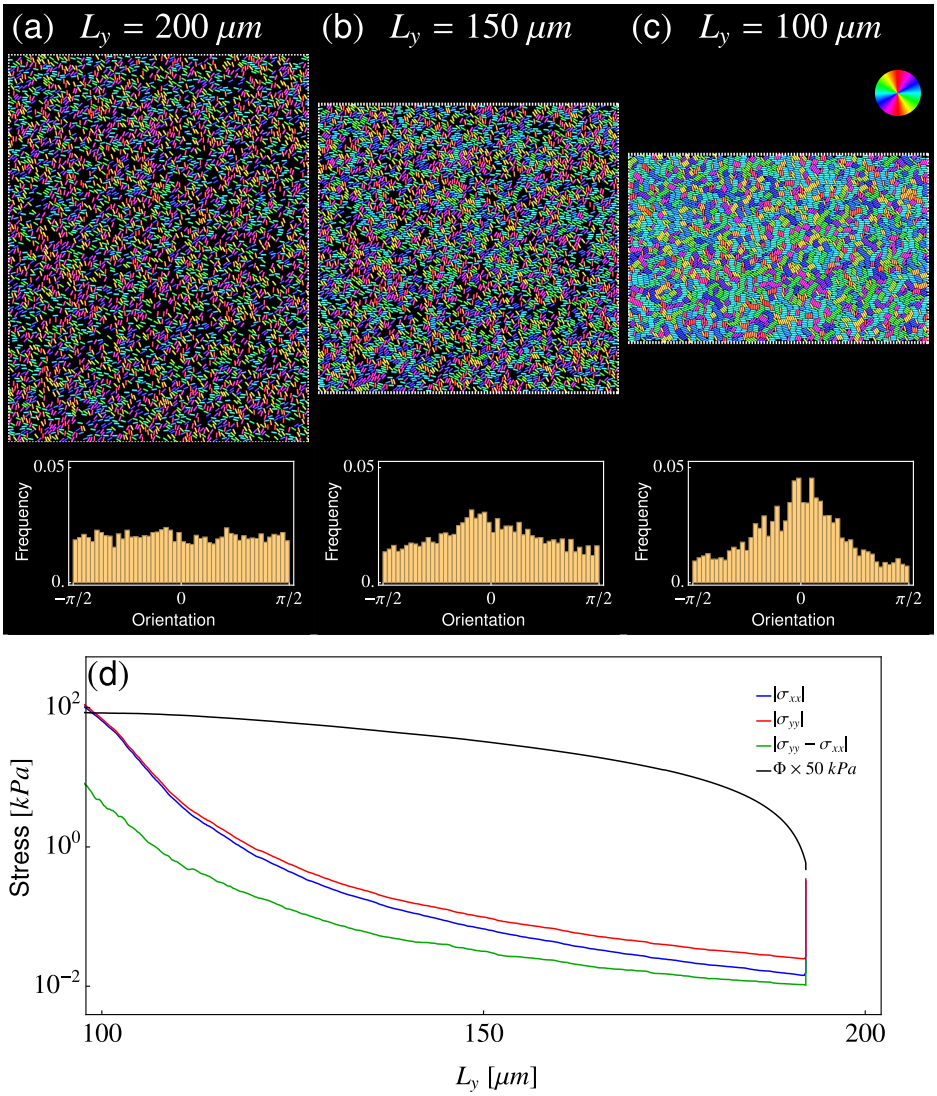

Figure 4.8. Dynamics of the shrinking colony. (a–c) Snapshots at different time points. Cells are color coded by their orientations according to the color wheel in panel (c). The insets show the histograms of the cell orientation at the corresponding time points. The system is periodic in both x and y. The system contains 5000 cells in total, with a width $L_x = 150$ μm and an initial height $L_y = 200$ μm. The shrinking speed, i.e. the relative speed between the top and the bottom boundaries, is $V_y = 10$ μm/h. (d) The average stresses and the global alignment parameter Φ as functions of the box height L_y. Again, we times Φ by 50 kPa in order to directly compare the trends of Φ and the stress components.

Figures 4.8a–d summarize the dynamics of the shrinking colony. The system is initially isotropic, orientationally (Fig. 4.8a) and mechanically (right side of Fig. 4.8d), represented by the uniformly distributed cell orientation and the small alignment parameter Φ. Once the shrinking is applied, σ_{yy} increases and, quite surprisingly, same as σ_{xx}, but the former increases faster. There are two reason to account for the increase of σ_{xx}. First, increasing the cell-cell overlap distance in y (when shrinking) may also increase the x component of the repulsive forces between neighboring cells. Second, the emerging anisotropic stress, as a consequence of anisotropic shrinking, can drive cells to reorient toward the horizontal direction (Fig. 4.8b and its inset) which, in turn redistributes the stress by decreasing σ_{yy} and increasing σ_{xx}, therefore diminishes the stress anisotropy. From this perspective, the reorientation of cells toward the direction of minimal stress is a strategy for the system to minimize the total elastic energy by redistributing the two normal components. For this reason, σ_{yy} does not deviate significantly from σ_{xx} (Fig. 4.8d), because further deviation can cause an additional reorientation of cells, which in turn reduces the stress anisotropy. In growing bacterial colonies, this negative feedback on stress anisotropy from cell reorientation is even more profound because the reorientation of cells not only directly redistributes the normal stresses, but also changes the growth-induced stress feed $\alpha(\boldsymbol{nn} - 1/2)$, which can further reduce the normal stress difference. Consequently, the normal stress difference is always much smaller than the two normal stresses (Figs. 4.7a and 4.7b). As the system shrinks further, both normal stresses as well as their difference increase, driving more and more cells to align in x and, finally, a highly aligned state is reached, where cell orientation is peaked at $\theta = 0$ (Fig. 4.8c and its inset). These results not only confirm that the stress anisotropy can indeed drive horizontal alignment, but also demonstrate a mutual regulation between cell orientation and the mechanical stresses.

We will now go back to the growing colony, and find the relation between cell orientation and the stress anisotropy to support our theory. The simplest evidence is to compare the time evolution of the two quantities. As shown in Fig. 4.7a, the alignment parameter Φ indeed increases simutaneously with the normal stress difference $|\sigma_{yy} - \sigma_{xx}|$. However, these quantities are averaged over the whole region I and, therefore, do not contain any information about the spatial variations of the stresses. Furthermore, in colonies subject to periodic or rigid wall confinements, during

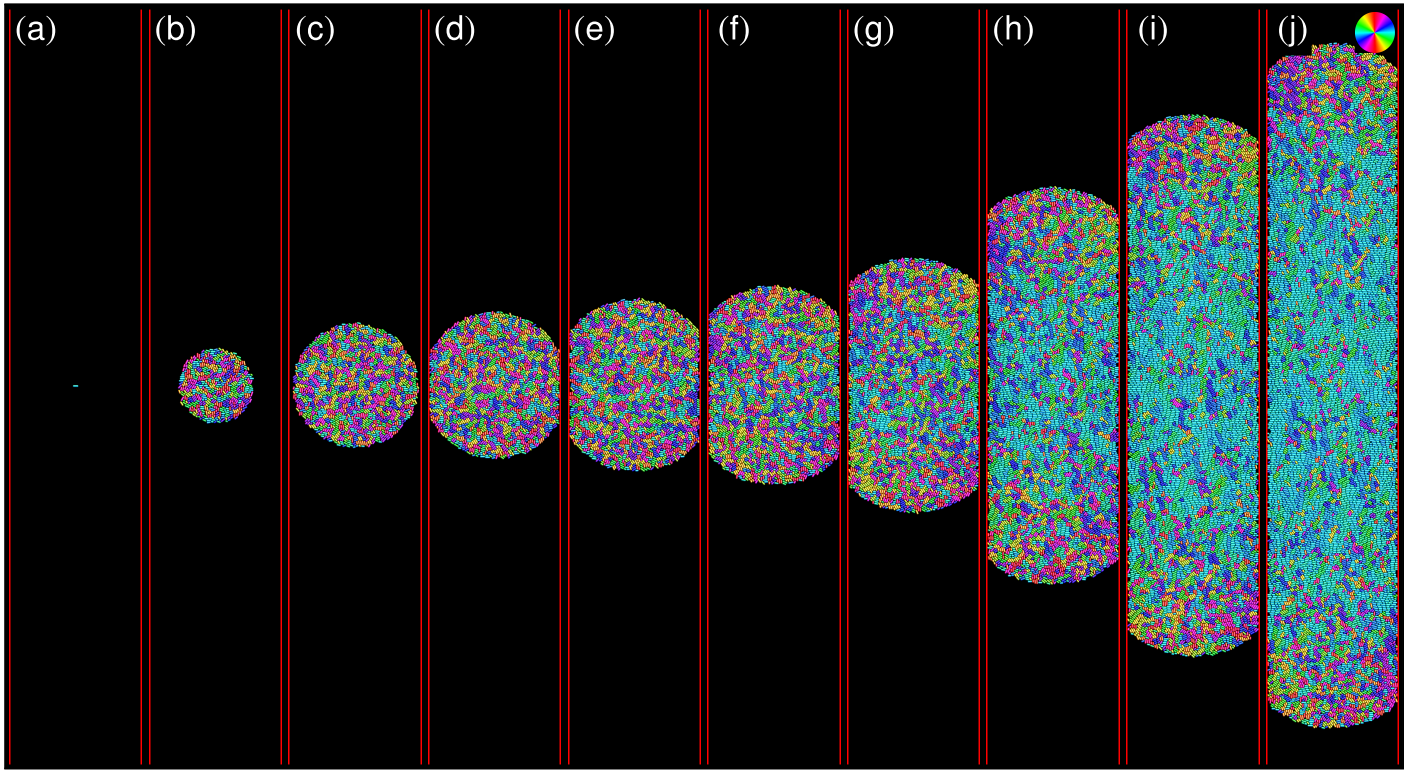

Figure 4.9. Snapshots of the growing colony that can freely expand in the vertical direction, at different time points. Cells are color coded by their orientation, as indicated by the color wheel in panel (j). The channel width is $L_x = 70$ μm, and the heights of all panels are 300 μm.

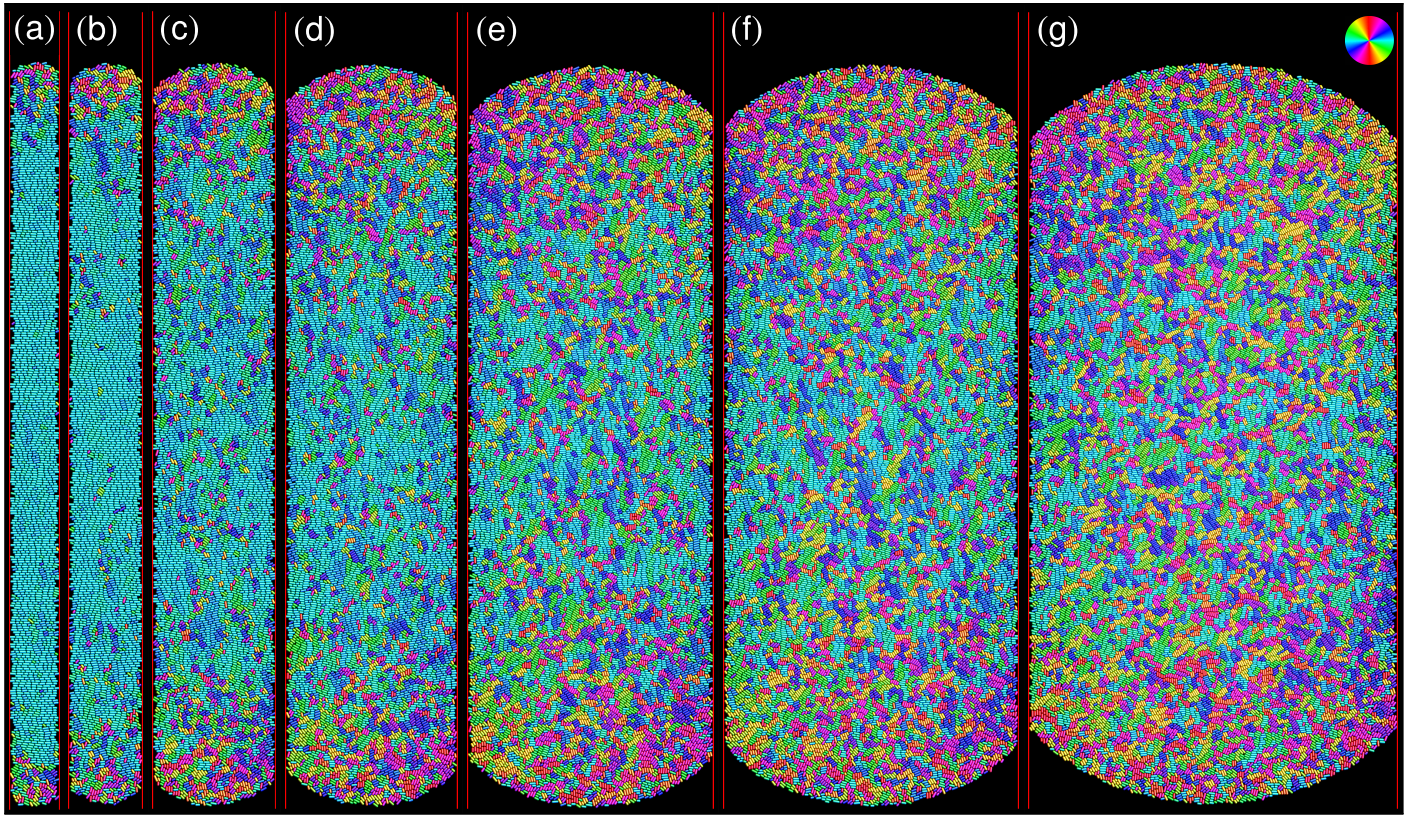

Figure 4.10. Snapshots of the unconfined colony with different L_x values: (a) 20 μm, (b) 40 μm, (c) 50 μm, (d) 70 μm, (e) 100 μm, (f) 120 μm, (g) 150 μm. The heights of all panels are 300μm. Cells are colored coded by their orientations, as indicated by the color wheel in panel (g).

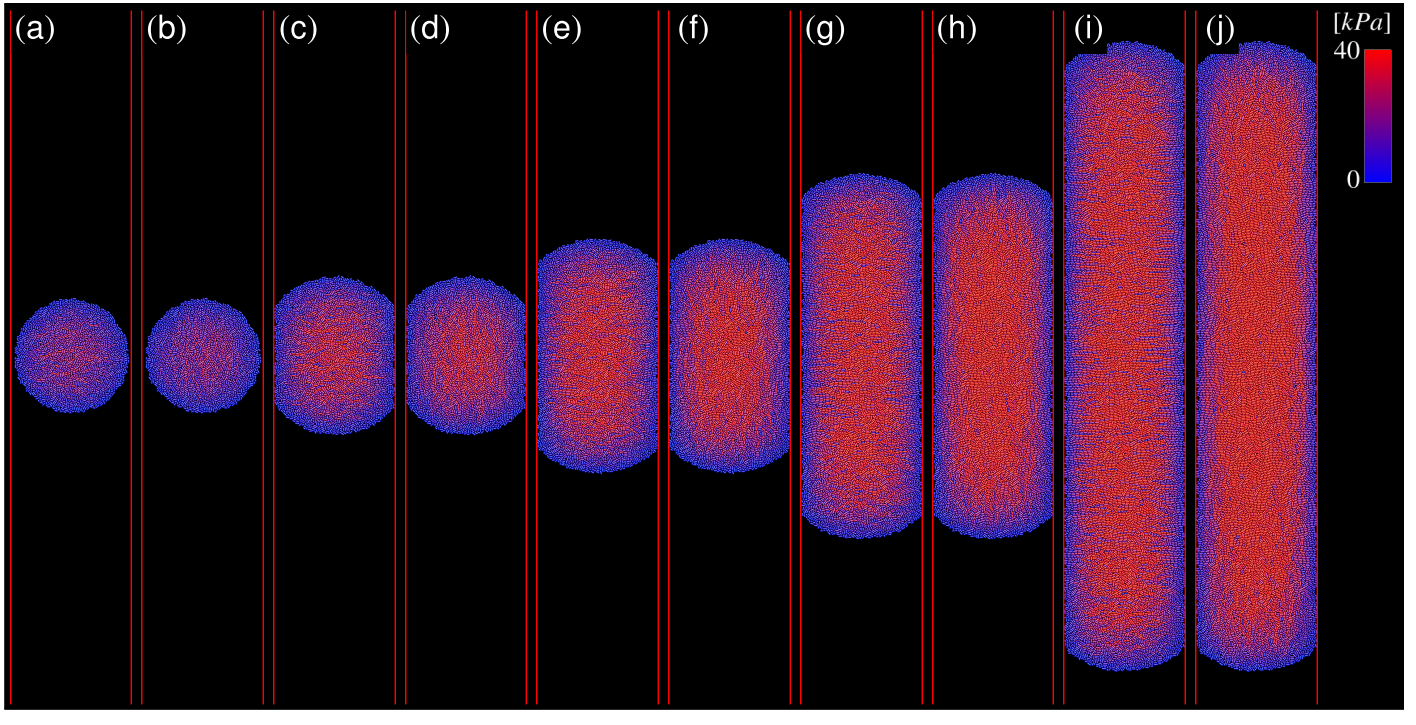

Figure 4.11. Stress distributions of the colony shown in Figs. 4.9 at different time points. Cells are color coded by the mechanical stresses they experience: (a, c, e, g, i) $|\sigma_{xx}|$ and (b, d, f, h, j) $|\sigma_{yy}|$. The color map is shown in the legend on the right hand side.

the development of global alignment, the system shows strong spatial and temporal inhomogeneities. Specifically, the stress has a large spatial variation, which is also rapidly evolving in time. It is very difficult to collect adequate samples to faifthfully capture the subtle interplay between stress and cell orientation. For this reason, we change the simulation setup by removing the vertical confinement and allow the colony to freely expand in the vertical direction. Surprisingly, even without an explicit confinement, the global alignment still appears, but at a much slower pace. Specifically, after an initial isotropic stage (Figs. 4.9a–e), a horizontal alignment gradually emerges from the horizontal axis of the colony, i.e. at $y = 0$ μm (Fig. 4.9f), when the colony's extension in y, denoted by R_y for convenience, becomes reasonably larger than that in x. As the colony explores further in y, the horizontally aligned region expands at a constant speed, leaving two disordered caps, of constant heights, symmetrically placed on the two ends of the elongated colony (Figs. 4.9g–j). More interestingly, increasing the channel width L_x makes it more difficult to develop the horizontal alignment and results in larger disordered caps (Figs. 4.10a–g).

These phenomena, again, can be ascribed to the anisotropic stress arising during the colony expansion. Figures 4.11a–j show the normal stresses that each cell experiences at different time points in the unconfined colony. Both $|\sigma_{xx}|$ and $|\sigma_{yy}|$ increase with time and decrease from the colony center to the vertical or horizontal boundaries as expected. For simplicity, we focus on the region $|x| < 10$ μm, and call it region III for convenience. The spatial distributions of stresses and alignment parameter Φ in region III are shown in Figs. 4.12a–e. Due to the elongated shape of the colony, in order to grow, cells in the bulk need to push more cells away in the vertical direction than in the horizontal direction. An anisotropic stress hence arises where $|\sigma_{yy}| > |\sigma_{xx}|$, and this stress anisotropy decreases monotonically with $|y|$, the vertical distance from the colony center (Figs. 4.12b–c). As the colony morphology becomes more anisotropic, the region with anisotropic stress expands, and the normal stress difference at a given location also increases with time (Fig. 4.12d). This explains why the horizontal alignment appears first at $y = 0$ μm, and then gradually expands in the vertical direction. Finally, most cells in the colony bulk align well in the horizontal direction (Fig. 4.9j). Without stress feed in y, and with a steady release of σ_{xx} by the expansion flow, both normal stresses as well as their difference saturate at certain values, and the colony bulk reaches a steady state (Fig. 4.12e). In wider channels, σ_{xx} at given

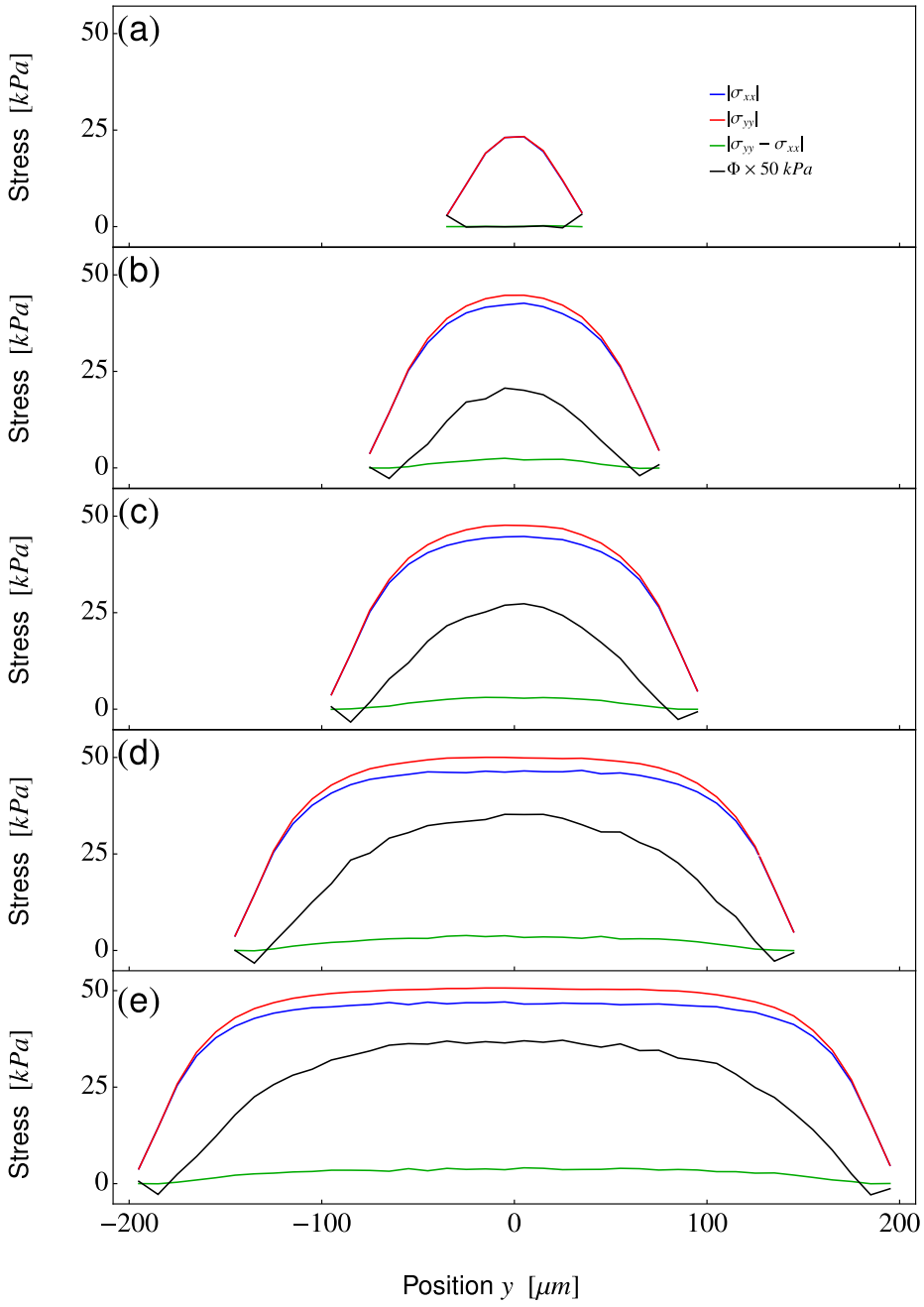

Figure 4.12. Spatial distributions of stresses and Φ in region III of an unconfined colony at different time points. The colony extensions in y, R_y's, are: (a) 70 μm, (b) 150 μm, (c) 190 μm, (d) 290 μm, and (e) 390 μm.

position, on average, is larger, hence requires larger R_y in order to create a stress anisotropy. Nevertheless, the horizontal alignment always emerges once the normal stress difference becomes nonzero.

These results suggest that the spatial-temporal variations of stresses and cell orientation are smoother in the unconfined colonies than the explicitly confined colonies, e.g. those shown in Figs. 4.2 and 4.4. In addition, one can easily control σ_{xx} and σ_{yy} in the unconfined colony by looking at different positions and different times, or changing the channel width L_x. Therefore, it is a perfect platform for us to study the relations between the horizontal alignment and the stress anisotropy. We notice that the expansion flow in bulk of the colony is mostly horizontal, and from $x = 0$ μm toward the outlets (i.e. $x = \pm L_x/2$). Hence, the local mechanical and orientational states of cells at the same height are correlated by the flow, while those at different heights are independent of each other. For this reason, we focus only on region III (i.e. $|x| < 10$ μm), the source of the expansion flow, and study the stresses and cell orientation at different heights and different time points of this region. To get as much data sample as possible, we grow the colony from a single cell until $R_y = 400$ μm, during which we take a sample snapshot whenever R_y increases by 10 μm. In each sample snapshot, we divide region III into small boxes, of dimension 20 μm$\times$10 μm, and then measure the average σ_{xx} and σ_{yy} over all cells in each box, as well as their alignment parameter Φ. We assume snapshots at different time points to be independent of each other. To explore further the parameter space, we change the channel width L_x from 50 μm to 150 μm with a step of 10 μm, and for each L_x we run 100 parallel simulations. These will give us a huge collection of sample boxes, each gives a specific combination of σ_{xx}, σ_{yy}, and alignment parameter Φ.

Figure 4.13a shows the phase diagram of the unconfined colony, spanned by the two normal stresses and the color indicates the average alignment parameter. The first thing to notice is that the system only occupies a very small region in the phase space: both normal stresses distribute closely to the line $|\sigma_{xx}| = |\sigma_{yy}|$ (white dashed line) in the phase space, due to the stress regulation by cell reorientation. In addition, there are more regions in the colony where $|\sigma_{yy}| > |\sigma_{xx}|$ because of the anisotropic colony morphology. Most importantly, horizontal alignment with large Φ (indicated as red), is more likely to be found in regions of large stress anisotropy. This is even more obvious in Fig. 4.13b, where the alignment parameter Φ increases monotonically with the stress anisotropy, defined

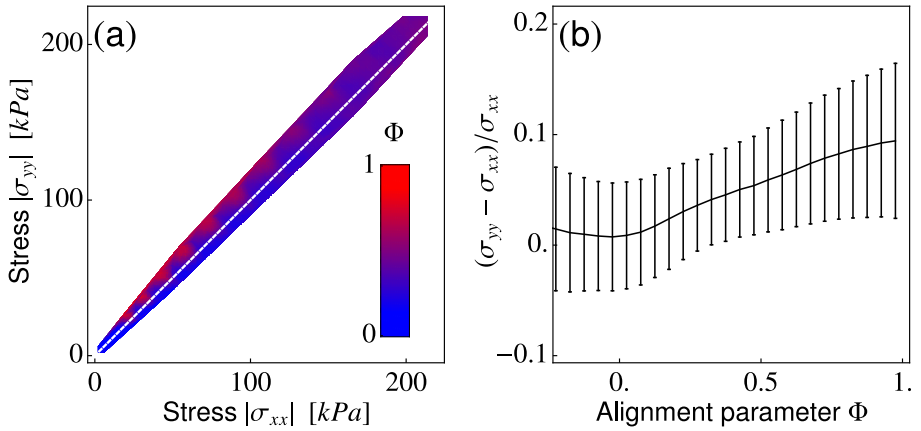

Figure 4.13. Statistical relations between the stress components and the alignment parameter in unconfined colonies. (a) Phase diagram of the unconfined colony, spanned by the two normal stresses and the color indicates the average alignment parameter. The color map is shown in the legend. The white dashed line indicates $|\sigma_{xx}| = |\sigma_{yy}|$. (b) Stress anisotropy, defined by $(\sigma_{yy} - \sigma_{xx})/\sigma_{xx}$, versus the alignment parameter. The error bars show the standard deviations of data samples about the average values.

by $(\sigma_{yy} - \sigma_{xx})/\sigma_{xx}$. At fixed Φ, though, the fluctuation of the stress anisotropy is quite large. This is because the two normal components have very similar values, so any small fluctuation of them can cause a dramatic change of the stress anisotropy. These results not only confirm our conjecture on the mechanism of horizontal alignment, but also validate our theory on the interplay between mechanical stresses and cell orientation.

4.3 Discussion and conclusion

In this chapter, we have explored the fascinating interplay among cell orientation, cell growth, and the mechanical stresses that cells experience. Cell orientation determines the direction of cell growth, and subsequently the growth-induced stress feed. The internal stress, if anisotropic, can drive cells to align with the direction of minimal stress. The reorientation of cells, in turn, not only redistributes the stress components, but also changes the direction of cell growth and accordingly the growth-induced stress feed. Both effects can reduce the normal stress difference and pro-

vide a negative feedback to the stress anisotropy. This three-way regulation loop not only dominates the dynamics of growing bacterial colonies, but also shapes them as smart materials that can actively regulate the internal stresses and navigate cell growth to maximize their fitness. An excellent example is, as shown in this chapter, the ability to deal with confinements during the colony expansion. The presence of confinement gives rise to a globally anisotropic stress, driving the cells to align in the unconfined direction and, guides the colony to expand in the easy direction.

In addition to the understanding of global alignment this theory provides, it also has some broader applications. In natural or artificial environments, bacterial colonies are frequently subject to different kinds of physical or geometrical confinements. This theory can predict cell orientation in such situations. For example, a phenomenon frequently observed in experiments is the merging of multiple colonies (Figs. 4.14a–d). In the merging region (highlighted by the colored boxes), cells collectively align with the common tangent of the two merging colonies. This is because the bulks of the two colonies act as confinements to cells at the merging fronts. Hence, cells reorient towards the common tangent and the merged colony expands much faster in the unconfined direction (Fig. 4.14c). Another example is cell growth on an elongated cylinder surface. Since cell motion is confined in the transverse direction, we can expect cells to align with the long axis of the cylinder. In addition, this theory also provides a potential way to control growing bacterial colonies with specifically engineered anisotropic stress. This can be done by applying confinements to the colony or, depleting cells at specific locations to drain the growth-induced stress. Also, as mentioned before, the internal stresses in the unconfined colony (see e.g. Fig. 4.9) follow very nice spatial patterns, which can be controlled by the channel width L_x or the colony extension R_y. This provides a nice setup to study the responses of cells to mechanical stresses.

Moreover, this theory also provides new insights into the physics of passive and active nematic liquid crystals. Increasing the packing fraction of lyotropic nematics, according to the classical Onsager theory, can cause a spontaneous symmetric breaking and drive the isotropic–nematic transition [76]. The resulting nematic phase, however, has no preferred orientation. Our theory, on the other hands, shows that the resulting global orientation can be decided beforehand, if the packing fraction is

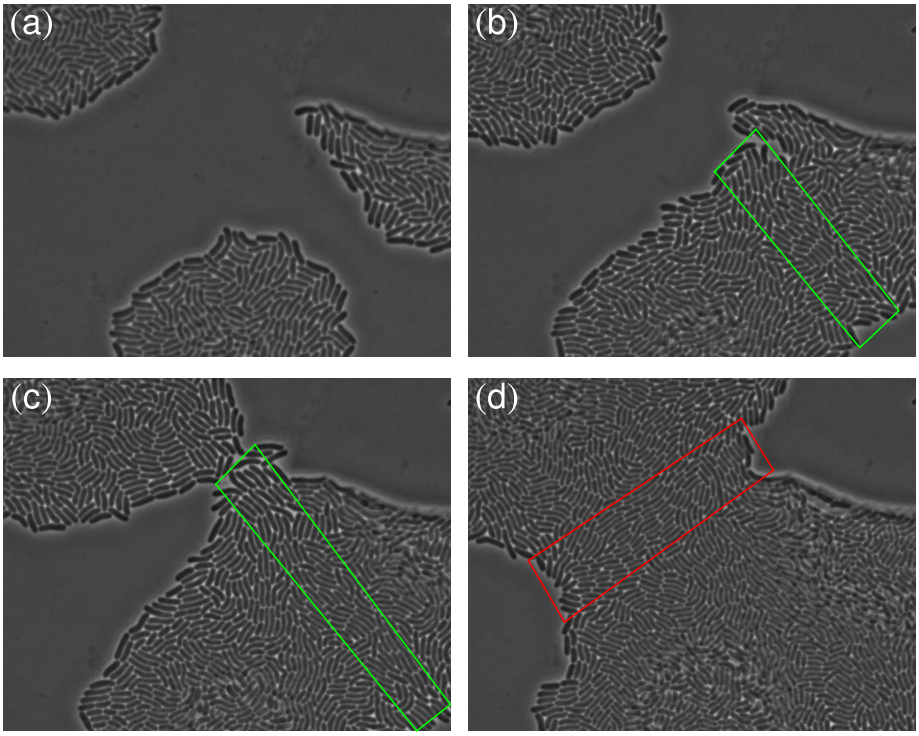

Figure 4.14. Experimental snapshots of the merging of three bacterial colonies at different time points. In the merging regions, i.e. those marked with colored boxes, cells collectively align with the common tangents of the two merging colonies. Images provided by Anupam Sengupta.

increased by applying anisotropic compression to the system. This is also in stark contrast with a recent study, which concluded that for moderately elongated spherocylinders, there was no orientational ordering upon athermal compression [106]. In addition, it has been extensively shown, experimentally and theoretically, that active matter systems, upon confinement, display a transition from chaotic dynamics to an ordered state [64, 86, 104, 107–109]. However, these results require the confinement to reduce the system size such that it's comparable to the system coherent length. Otherwise, the system will still be chaotic. Here, we show that in growing bacterial colonies, no such strong confinement is needed. The system can develop global order as long as the confinement leads to a global anisotropic stress. This introduces new roles of confinement to the

dynamics of active matter.

To look into the future, there are still unresolved problems along this line. For example, it is interesting to test our theory at different geometries, such as the microfluidic channels used in Ref. [51]. More quantitative characterization of the interplay between stress and cell orientation can definitely deepen our understanding on the mechanics of nematic liquid crystals. Finally, a continuum theory incorporating the coupling among mechanical stresses, cell orientation, and the cell growth, would be very useful for practical applications and theoretical studies.

Chapter 5

Mono-to-multilayer transition

Previous chapters have shown various examples of emergent phenomena induced by cell growth in expanding monolayers, free or confined. In this chapter, we will demonstrate that in-plane cell growth can also drive an escape to the third dimension, and trigger a transition from mono- to multilayer structure, i.e. the next step toward biofilm formation. Such a mono-to-multilayer transition has recently drawn significant attention in the biophysical literature, being a universal step in biofilm formation, as well as a process where mechanical forces are likely to play a leading role. Grant *et al.* explored the effects of various mechanical forces on the mono-to-multilayer transition in *E. coli* colonies confined between a glass slide and an agarose gel [56]. They measured the transition position and the size of the colony at the onset, from both experiments and simulations, and studied how these quantities were mediated by different mechanical interactions. More recently, Beroz *et al.* [66] demonstrated that, in *V. cholerae* biofilms, the transition is triggered by the mechanical instability of individual cell. Using a mean-field calculation, they find that the critical pressure decreases with the cell length and, consequently, the transition is more likely to be triggered by a cell division. Similar mechanisms are also found in confluent monolayers of eukaryotic cells [110–117, 13, 118] and are believed to regulate cell extrusion and apoptosis. These works have greatly contributed to shed light on the problem, however, a general understanding of the physical mechanisms underpinning the mono-to-multilayer transition is still lacking, with questions far outnumbering the answers so far: *1)* Is there a well-defined critical state? *2)* If so, what determines the critical state? *3)* Can we predict when and where the transition will happen?

In this chapter we address these questions theoretically, using a combination of numerical and analytical methods. We demonstrate that the

mono-to-multilayer transition in a system of growing rod-like cells results from a competition between the in-plane active stresses, that compress the cells laterally, and the vertical restoring forces, owing to the cell-substrate interactions (e.g. compression from the agarose on top or adhesion from the substrate beneath). As the colony expands, the internal stress increases until it is sufficiently large to cause extrusion of the first cell. In the ideal case of a chain-like colony of laterally-confined non-growing cells, being compressed from the two ends, the transition is entirely deterministic and the critical stress that triggers the extrusion can be calculated analytically. Asynchronous cell division, however, renders the transition stochastic. In this case, the critical stress is a continuously distributed random variable and the first extrusion does not necessarily occur at the colony center, despite this being the region of maximal stress. Upon modeling the transition as a Poisson process, we can approximately calculate the probability distribution function (PDF) of the position and time associated with the first extrusion. Finally, we show that rate of the Poisson process, is analogous to an order parameter and that, in this respect, the mono-to-multilayer instability is likened to a continuous phase transition.

5.1 Simplified hard-rod model

We still use the hard-rod model introduced in section 2.1, with suitable simplification of mechanical interactions. Whereas cells in bacterial colonies are potentially subject to a large variety of mechanical and biochemical stimuli, here we focus on three types of forces that are important to the transition: the repulsive forces associated with cell-cell and cell-substrate steric interactions and a vertical restoring force, representing either the mechanical compression from the agarose gel on top [56, 65], or the attractive force due to adhesion of the cells with the glass slide or the ECM [66]. Neighboring cells interact with the same way as shown in section 2.1, with an exception that the forces are now Hookean instead of Hertzian. This can greatly simplify the analysis of mechanical interactions and make analytical treatments possible, while preserving the same physical picture. The force from the jth cell to the ith is then $\boldsymbol{F}_{ij}^{c} = k_c h_{ij} \boldsymbol{N}_{ij}$, with k_c the elastic constant of cells. Similarly, the force from the substrate is $\boldsymbol{F}_{i\alpha}^{s} = k_s(d_0/2 - z_{i\alpha})\hat{\boldsymbol{z}}$, where $z_{i\alpha}$ is the $z-$coordinate of the caps, if $z_{i\alpha} < d_0/2$, or $\boldsymbol{F}_{i\alpha}^{s} = k_a l_i (d_0/2 - z_{i\alpha})\hat{\boldsymbol{z}}$, if $d_0/2 < z_{i\alpha} < d_0/2 + r_a$. Here, k_s and k_a represent respectively the elasticity of the substrate and

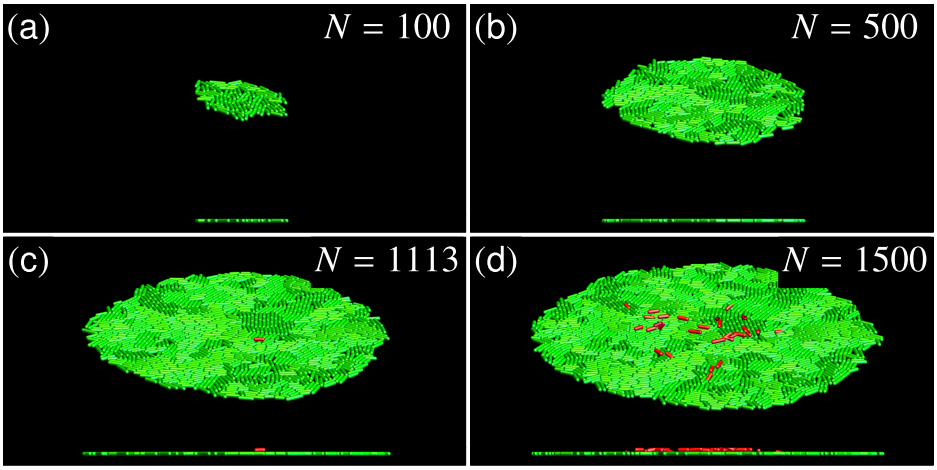

Figure 5.1. Snapshots of a simulated growing colony at different ages to show the mono-to-multilayer transition. The lower image in each panel shows the side view. In panels (c) and (d), the extruded cells are highlighted as red.

the strength of the vertical restoring force, and r_a is the range of the restoring force, beyond which the restoring force vanishes. The vertical restoring force in general can depend on cell length in a very complicated manner. Here, we simply set the vertical restoring force to be proportional to the cell length, which is true in case of cell-substrate adhesion where the number of adhesion molecules is proportional to the area of the cells [66]. We stress that our model does not aim to accurately reproduce the traits of a specific bacterial family, but rather to abstract the essential features that all bacteria undergoing the mono-to-multilayer transition have in common.

We integrate Eqs. 2.2 numerically using the following set of parameter values: $d_0 = 1\,\mu$m, $k_c = k_s = 10$ MPa μm, $\zeta = 100$ Pa h and $r_a = 0.01$ μm[62]. The division length l_d varies from $3\,\mu$m to $4\,\mu$m and the growth rate varies from $1\,\mu$m/h to $2\,\mu$m/h. The integration is performed with a time step $\Delta t = 10^{-6}$ h.

Figure 5.1 shows typical configurations of our *in silico* colonies at different time points. Consistent with the experimental evidence [61, 56], the colony initially expands as a perfect monolayer (Figs. 5.1a,b) and, once it is sufficiently large, some cells are extruded and initiate a second layer (Figs. 5.1c,d).

5.2 Mechanics of mono-to-multilayer transition

The mechanical interactions in the full 3D model is very complicated, for the repulsion between neighboring cells depends on their relative position and the relative orientation. For simplicity, we look at a simplified chain-like colony, consisting of a row of cells confined in a channel (Fig. 5.2a). This, in the simulation, is done by manually setting the y components of $\boldsymbol{r}_i$ and $\boldsymbol{p}_i$ to be zero for all cells and at all times. The cells have identical length l and do not grow, but are compressed by a pair of forces f applied at the two ends of the channel. By doing so, we can manually control the internal stress in the colony, hence can accurately determine the critical state at which the transition happens. At the beginning of the simulation, all cells are right on top of the substrate, i.e., $z_i = d_0/2$ and $q_{xi} = 1$. Then the compression force is increased very slowly from $0N$, such that the colony is at mechanical equilibrium for all times. In other words, all cells are experiencing the same internal stress imposed by the compression on the two ends.

As in the case of disk-like colonies (Fig. 5.1), cells remain perfectly attached to the substrate for small compression forces. Once the compression force exceeds a certain value, one of the cells is extruded to the second layer. The existence of a well-defined critical force, f^*, at which the monolayer becomes unstable, indicates that the transition is entirely deterministic in this case. The critical force f^* can be calcu-

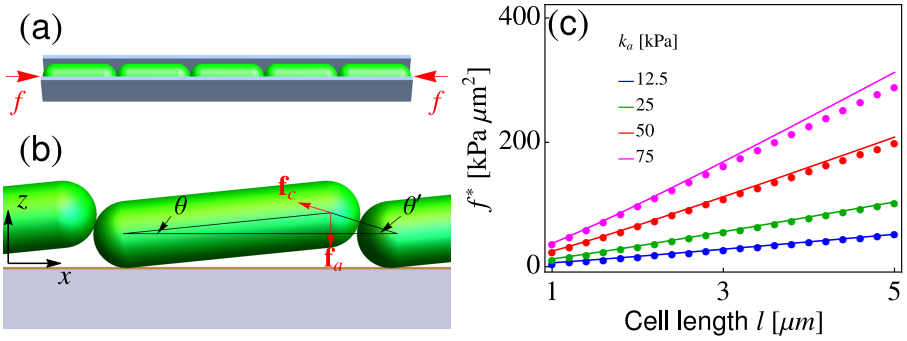

Figure 5.2. (a) Schematic diagram of the chain-like colony. (b) Schematics of torque balance about the lower end of the cell. (c) Critical force f^* as a function of the cell length l, at various k_a values. The dots and lines represent respectively the simulation and analytical results as in Eq. 5.2.

lated analytically upon balancing the torques associated with cell-cell and cell-substrate interactions, about the lower end of the cell axis. Calling $\boldsymbol{p} = (\cos\theta, 0, \sin\theta)$ the orientation of the first extruded cell and $\boldsymbol{f}_c = f_c(-\cos\theta', 0, \sin\theta')$, with $f_c = f/\cos\theta'$, the contact force exerted by the nearby cell (Fig. 5.2b), the lifting torque can be calculated in the form: $\tau_c = l(p_x f_z - p_z f_x) = lf\cos\theta(\tan\theta + \tan\theta')$. Analogously, the restoring torque resulting from the adhesive force is $\tau_a = k_a l^3 \sin\theta\cos\theta$. In a perfectly horizontal monolayer, $\theta = \theta_0 = 0$ and both torques vanish. Any deviation from the equilibrium configuration will induce increases of both torques with respect to θ, at rates

$$\begin{aligned} \frac{d\tau_c}{d\theta} &\approx fl\,(1 + l/d_0) \\ \frac{d\tau_a}{d\theta} &\approx k_a l^3, \end{aligned} \tag{5.1}$$

respectively. Note that $d\tau_c/d\theta$ increases linearly with the compression force f. For a sufficiently small f vale, τ_a outgrows τ_c, hence any deviation from the equilibrium configuration, however small it is, will be brought back to balance. This is why the cells are perfectly attached to the substrate when $f < f^*$. In order for such a configuration to be unstable against slight orientational fluctuations, one should have $d\tau_c/d\theta \geq d\tau_a/d\theta$. The equality then sets the critical force as:

$$f^* = k_a l^2 \left(1 + \frac{l}{d_0}\right)^{-1}, \tag{5.2}$$

in excellent agreement with the result of our numerical simulations (Fig. 5.2c). The existence of a well defined critical force resulting from the competition between compression and rotation is vaguely reminiscent of Euler's buckling in elastic rods. However, while buckling is a system-wide instability, the mono-to-multilayer transition is determined by torque balance at the length scale of a single cell.

5.3 Stochastic theory

Next we study the mono-to-multilayer transition in a growing colony. Cells are again confined in the channel for simplicity and, unlike the previous case, they are not subject to lateral compression, but elongate and divide. To investigate the effect of the key parameters, k_a, l_d, and g, we perform

four sets of 10^5 simulations, starting from a single cell at the equilibrium configuration. In the "control" set, we fix $k_a = 25$ kPa, $l_d = 4$ μm, and $g = 2$ μm/h. In each of the remaining three sets we change one of the parameters.

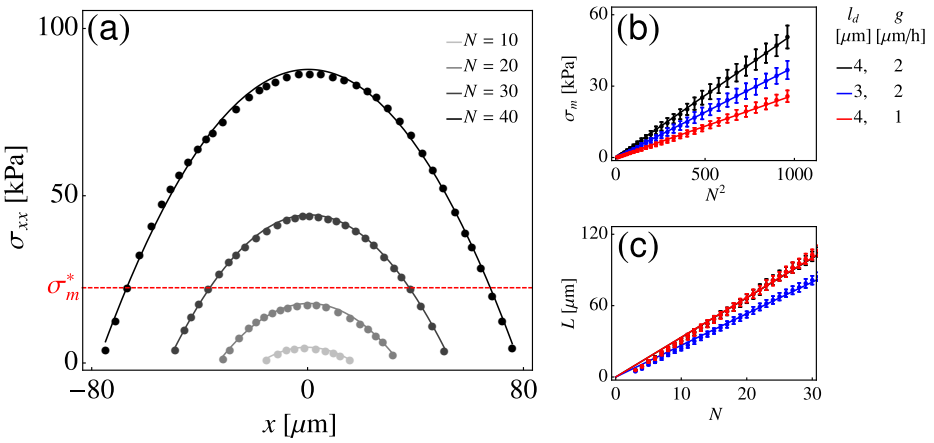

Figure 5.3. (a) The spatial distributions of stress in growing chain-like colonies at different ages, at the "control" parameters. (b) The maximum stress σ_m is proportional to N^2, while (c) the colony length L increases linearly with cell number N. The error bars show the standard deviations of results from 10000 runs about the average values. Solid lines indicate the best fit, linear or parabolic, to the data points.

As the colony expands, the internal stress progressively builds up. To have a quantitative understanding of the spatial-temporal evolution of internal stress, we measure the internal stress experienced by each cell via the virial construction as we did in the previous chapters (see e.g. Refs. [38, 60]). We focus on the in-plane stresses that trigger the mono-to-multilayer transition, namely:

$$\boldsymbol{\sigma}_i = \frac{1}{a_i} \sum_{j=1}^{N_i^c} (\boldsymbol{\Pi} \cdot \boldsymbol{r}_{ij})(\boldsymbol{\Pi} \cdot \boldsymbol{F}_{ij}^c) \,, \tag{5.3}$$

where $a_i \approx d_0(l_i + d_0)$ is the area of the i-th cell and $\boldsymbol{\Pi} = \boldsymbol{I} - \hat{\boldsymbol{z}}\hat{\boldsymbol{z}}$, with $\boldsymbol{I}$ the identity, is a projection operator on the $xy-$plane. In the case of a chain-like colony, such as that depicted in Fig. 5.2a, the $y-$components of both $\boldsymbol{r}_{ij}$ and $\boldsymbol{F}_{ij}^c$ vanish and σ_{xx} is the only nonzero component of the in-plane stress. Because of the extensile nature of growth-induced stress, σ_{xx}

has negative values. Nevertheless, for convenience, we neglect the sign of σ_{xx}, and use it to indicate the magnitude of the in-plane stress, i.e. $|\sigma_{xx}|$. While the local stress experienced by each cell is increasing with time, at the colony scale it follows a simple parabolic profile of the form:

$$\sigma_{xx}(x) = \sigma_m \left[1 - \left(\frac{2x}{L}\right)^2\right] , \tag{5.4}$$

where σ_m and L represent respectively the maximum stress and the colony length (Fig. 5.3a). Numerically, we find that $\sigma_m = aN^2$ and $L = bN$ (Figs. 5.3b and 5.3c), where N is the total number of cells and a and b are constants depending only on the division length l_d and the growth rate g.

The stress profile shown in Eq. 5.4 can be derived analytically by assuming an over-damped dynamics and the incompressibility of cells. Consider a cell of length l and position x, subject to a stress difference

$$\Delta\sigma_{xx} = \sigma_{xx}(x + l/2 + d_0/2) - \sigma_{xx}(x - l/2 - d_0/2) \tag{5.5}$$

on the two ends. From Eq. 5.3, the resultant force on the cell is $\Delta F_x = -d_0\Delta\sigma_{xx}$, and the velocity

$$\begin{aligned} v_x &= -\frac{d_0}{\zeta l}\Delta\sigma_{xx} \\ &= -\frac{d_0(l+d_0)}{\zeta l}\frac{\Delta\sigma_{xx}}{l+d_0} \\ &\approx -\frac{d_0(l+d_0)}{\zeta l}\frac{\partial\sigma_{xx}}{\partial x}, \end{aligned} \tag{5.6}$$

or equivalently

$$\begin{aligned} \frac{\partial\sigma_{xx}}{\partial x} &= -\frac{\zeta l}{d_0(l+d_0)}v_x \\ &\approx -\frac{\zeta l_a}{d_0(l_a+d_0)}v_x, \end{aligned} \tag{5.7}$$

where $l_a = (l_d + l_m)/2$ and $l_m = (l_d - d_0)/2$ are respectively the average and minimal lengths of cells.

Now we will get the velocity profile. Assume the cell chain is symmetric about the point $x = 0$. If the amount of overlap between neighboring cells

is reasonably small compared to the cell length, the velocity of a cell at position $x > 0$ is

$$v_x = \sum_{0<x_i\leq x} g_i \approx \frac{xg}{l_a + d_0}. \tag{5.8}$$

The last approximation is based on the *Law of Large Number*, where $x/(l_a + d_0)$ is the average number of cells in region $(0, x]$. Especially, the total number of cells, on average, is $N = L/(l_a + d_0)$. Hence, parameter b can be approximated as $b \approx (l_a + d_0)$. Substitute Eq. 5.8 in Eq. 5.7, and integrate both sides of the equation from x to $L/2$, we have

$$\int_x^{L/2} \frac{\partial \sigma_{xx}}{\partial x'} dx' = -\int_x^{L/2} dx' \frac{\zeta g l_a}{d_0 (l_a + d_0)^2} x'. \tag{5.9}$$

By applying the boundary condition $\sigma_{xx}(L/2) = 0$, one arrives at

$$\sigma_{xx}(x) = \frac{\zeta g l_a L^2}{8 d_0 (l_a + d_0)^2} \left[1 - \left(\frac{2x}{L}\right)^2\right]. \tag{5.10}$$

It can be demonstrated that Eq. 5.10 also applies to cells at $x < 0$. Since $L = (l_a + d_0)N$, $\sigma_m = \zeta g l_a N^2/(8 d_0)$ and $a = \zeta g l_a/(8 d_0)$. Comparison between the simulated and analytical values of a and b can be found in Tab. 5.1.

Parameters	b [μm]		a [kPa]	
[μm],[μm/h]	Simulation	Analytics	Simulation	Analytics
$l_d = 3$, $g = 2$	2.8	3.0	0.038	0.050
$l_d = 4$, $g = 2$	3.5	3.7	0.052	0.068
$l_d = 4$, $g = 1$	3.5	3.7	0.026	0.034

Table 5.1. Comparison between the simulated and analytical values of a and b.

Because the stress is maximal at the center of the colony, one would expect the first extrusion to occur here. Our simulations, however, show a dramatically different behavior. Specifically, the position of the first extruded cell x^* has a random value and it follows a broad distribution, whose spread is comparable to the size of the colony itself (Fig. 5.4a). Analogously the transition time t^* (Fig. 5.4b) and the critical stress σ^* experienced by cells at the verge of extrusion (Fig. 5.4c), are continuously distributed random variables.

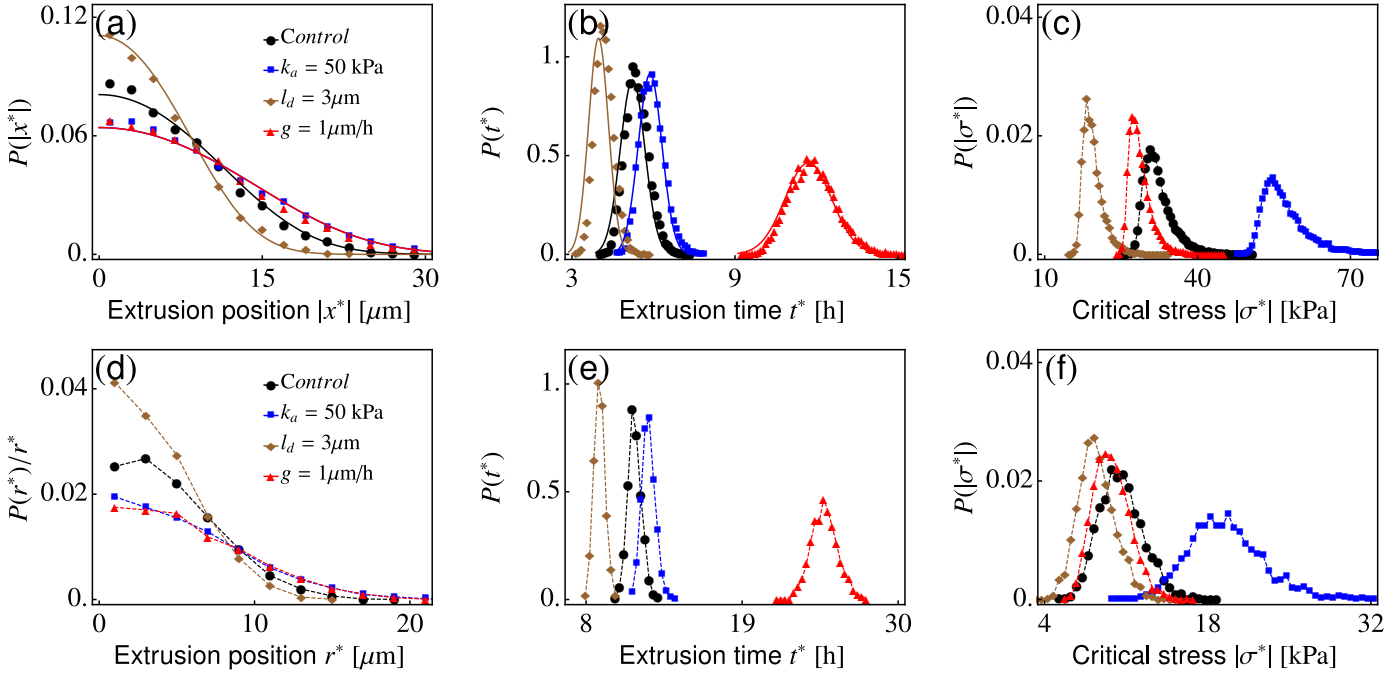

Figure 5.4. (a-c) Probability densities of (a) the extrusion positions $|x^*|$, (b) the extrusion time t^*, and (c) the critical stress σ^*, for chain-like colonies of asynchronously dividing cells. (d) Probability density of the extrusion position r^* in disk-like colonies, normalized by r^*, the distance from the point of extrusion to the centroid of the colony. (e-f) Same as panels (b-c), but for disk-like colonies. In all panels, dots and dashed lines correspond to the simulation results and the solid lines to the analytical predictions. In each set of simulations, one parameter is changed compared to the "control" set, whose parameter values are indicated in the legends. The statistical results for each set of parameters are collected from 10000 runs for chain-like colonies, and 2000 runs for disk-like colonies.

The lack of well defined critical stress is in stark contrast with the classical buckling scenario, but shares some similarity with the onset of fracture in heterogeneous media [119], i.e., the weakest point dominates. In the following, we demonstrate that, in growing bacterial colonies, this behavior results from the combined inherent randomness of cell length and the dependence of critical force on the cell length. According to Eq. 5.2, a cell is unstable to extrusion if subject to a critical stress, whose magnitude increases with the cell length. In a growing colony of desynchronized division, however, cells have different lengths, hence require different critical stresses. In addition, each cell is also experiencing different local stress. This means that the transition can happen to any cell as long as the local stress exceeds the critical stress demanded by the local cell length. As a consequence, there is no unique critical state in a growing colony, but rather an ensemble of them, each corresponding to a specific combination of cell length and the corresponding critical stress. Furthermore, the desynchronization of cell division makes it impossible to predict which critical state to appear first. This is the origin of stochasticity of the mono-to-multilayer transition in a growing bacterial colony.

The stochasticity of the transition demands that the problem can only be tackled with statistical methods. In principle, one can work out the time evolution of the statistical distribution of the critical states, from which the probability distributions of the transition position and time can then be obtained. In practice, we find that the transition is mostly triggered by cell division. This is understandable: a division event introduces a sudden drop in the cell length and this can, in turn, trigger an extrusion instability, as long as the cell is subject to a stress larger than that required to extrude a cell of minimal length $l_m = (l_d - d_0)/2$. A similar phenomenon was found in [66]. We denote such a minimal critical stress σ_m^*. As the stress is spatially inhomogeneous and increasing in time, there will be a whole region, symmetric with respect to the center of the colony and whose length increases in time, where the local stress exceeds σ_m^* and cell division can trigger the first extrusion. We call this region the P-zone. The probability associated with the first extrusion is then equal to the probability of having a division within the P-zone. This can be calculated as follows.

Let us consider a colony of n cells with growth rate g and assume that, at an arbitrary time, their lengths are independent and uniformly distributed in the interval $l_m \leq l \leq l_d$. After a time t, the probability that

no division has yet occurred equates the probability that none of the cells is initially longer than $l_d - gt$:

$$P(t) = \left(\frac{l_d - gt - l_m}{l_d - l_m}\right)^n \approx e^{-\lambda(n)t} \,, \tag{5.11}$$

where $\lambda(n) = ng/(l_d - l_m)$ and the approximation holds for large n values ($n \gtrsim 5$). Equation 5.11 defines a Poisson process of rate $\lambda(n)$ [120]. In the case where the cell growth rate is also a random variable uniformly distributed in the interval $g/2 \leq g_i \leq 3g/2$, as we have in our hard-rod model, one can prove the rate to become

$$\lambda(n) = \frac{1}{l_d - l_m} \sum_{i=1}^{n} g_i \,. \tag{5.12}$$

For sufficiently large n values, by the *law of large number*, we have $\sum_{i=1}^{n} g_i \approx ng$ so that:

$$\lambda(n) \approx \frac{ng}{l_d - l_m} \,. \tag{5.13}$$

Furthermore, if n is time-dependent, the process becomes inhomogeneous, but the probability preserves the same structure, with $\lambda(t) \equiv \lambda[n(t)]$ and $P(t) = e^{-\int_0^t \mathrm{d}t\, \lambda(t)}$ [120]. The PDF associated with observing the first division at time t is then:

$$f(t) = \frac{\mathrm{d}}{\mathrm{d}t}[1 - P(t)] = \lambda(t) e^{-\int_0^t \mathrm{d}t'\, \lambda(t')} \,. \tag{5.14}$$

In our case, n represents the number of cells within the P-zone. Given the length of the P-zone L^*, the total number of cells in it is a random variable because of the random growth rate. Approximating $\sum_{i=1}^{n} l_i \approx n l_a$ (again, *law of large number*), with $l_a = (l_d + l_m)/2$ the average cell length, we have $n = L^*/(l_a + d_0)$. L^* can be calculated by solving $\sigma_{xx}(L^*/2) = \sigma_m^*$ (red dashed line in Fig. 5.3a). This yields:

$$L^* = b\sqrt{N^2(t) - N_0^2}, \tag{5.15}$$

where $N_0 = \sqrt{\sigma_m^*/a}$ is the minimal number of cells required for the P-zone to exist. From this and Eq. 5.13, we can calculate the rate $\lambda(t)$ as:

$$\lambda(t) = \frac{gb}{(l_d - l_m)(l_a + d_0)} \sqrt{N^2(t) - N_0^2} \sim [N(t) - N_0]^{1/2} \,. \tag{5.16}$$

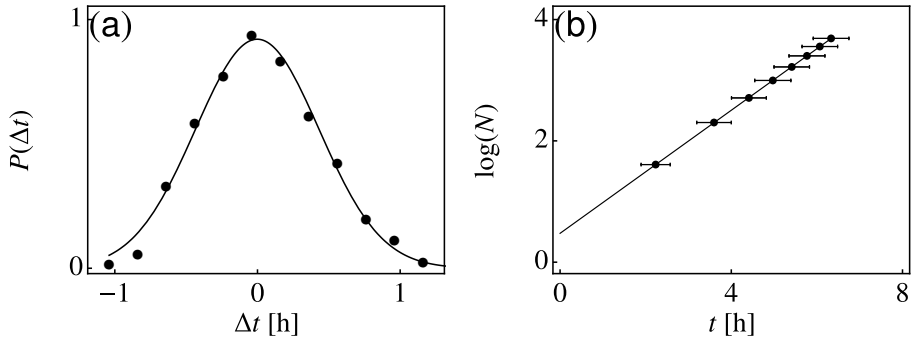

Figure 5.5. Relation between cell number N and time t, at $l_d = 4\mu$m and $g = 2\mu$m/h. (a) The time t taken by the colony to attain a given population N is a random variable of the form $t = \bar{t} + \Delta t$, with Δt Gaussianly distributed (the solid line shows the best Gaussian fit). (b) N increases exponentially with the average time $\bar{t}$. The black dots represent the average $\bar{t}$ and the horizontal error bars show the standard deviation of 10^4 data samples about the average value $\bar{t}$.

Equation 5.16 highlights the role of λ as an order parameter for the mono-to-multilayer transition. For $N(t) < N_0$, λ is imaginary and the probability of observing an extrusion vanishes identically. On the other hand, for $N(t) > N_0$, λ is real and the probability of observing an extrusion increases in time. The transition is continuous in this case, but other scenarios are likely possible.

To make the time-dependence explicit in Eq. 5.16, we need to calculate $N(t)$. Evidently, the average number of cells in the colony grows exponentially in time. Because of the random growth rate, the time t taken for the colony to attain a given population N is a random variable of the form $t = \bar{t} + \Delta t$. Numerically, we find that Δt follows a Gaussian distribution $\mathcal{N}(0, \delta^2_{\Delta t})$ with a zero mean and a variance $\delta^2_{\Delta t}$ (Fig. 5.5a). In addition, $N(\bar{t}) \sim \exp(\omega \bar{t})$ (Fig. 5.5b), as a consequence of the exponential growth, or equivalently $\bar{t} = \omega^{-1} \log(N)$. We can then express $t = \omega^{-1} \log(N) + \Delta t$ and $N(t) = \exp[\omega(t - \Delta t)]$. Replacing this in Eq. 5.16 yields:

$$\lambda(t, \Delta t) = \frac{gb}{(l_d - l_m)(l_a + d_0)} \sqrt{e^{2\omega(t-\Delta t)} - N_0^2} \, . \tag{5.17}$$

As shown in Fig. 5.6, at fixed $\Delta t = 0$, $\lambda(t, 0) \sim \sqrt{t - t_0}$ for $t \gtrsim t_0$, where $t_0 = \omega^{-1} \log(N_0)$ is the average time at which the P-zone first appears. Because of the exponential decreasing of $f(t)$ with increasing λ,

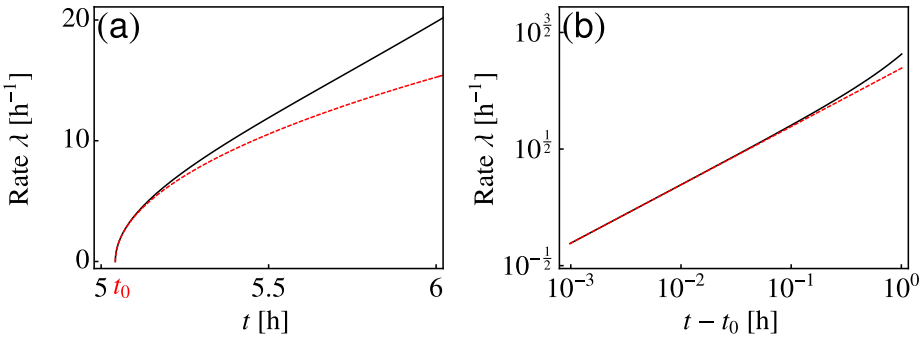

Figure 5.6. (a) Rate $\lambda(t, 0)$ (i.e. Eq. 5.17) of the Poisson process at the "control" parameters. (b) Same as panel (a), but in a Log-Log scale. The red dashed lines in both panels show the plots of $\lambda(t, 0) = k_\lambda\sqrt{t - t_0}$.

most extrusions happen in this time region. This yields, for nonzero Δt and $t > t_0 + \Delta t$,

$$\lambda(t, \Delta t) \approx k_\lambda\sqrt{t - t_0 - \Delta t}, \tag{5.18}$$

where

$$k_\lambda = \frac{gbN_0\sqrt{2\omega}}{(l_d - l_m)(l_a + d_0)}, \tag{5.19}$$

which can be obtained by Taylor-expanding $\lambda(t, \Delta t)$ about $t_0 + \Delta t$.

The probability distribution function (PDF) associated with observing the first extrusion at time t, given its offset Δt from the average $\bar{t}$, can then be expressed as a conditional PDF of the form:

$$\begin{aligned} f(t|\Delta t) =& \lambda(t, \Delta t)e^{-\int_0^t \lambda(t', \Delta t)\mathrm{d}t'} \\ =& k_\lambda(t - t_0 - \Delta t)^{1/2}e^{-\frac{2}{3}k_\lambda(t - t_0 - \Delta t)^{3/2}}, \end{aligned} \tag{5.20}$$

which is a Weibull distribution and can be approximated as a Gaussian distribution of the same mean and variance [121]:

$$f(t|\Delta t) \approx \mathcal{N}\left[t_0 + \Delta t + \Gamma\left(\frac{5}{3}\right)\left(\frac{3}{2k_\lambda}\right)^{\frac{2}{3}}, \left(\frac{3}{2k_\lambda}\right)^{\frac{4}{3}}\left[\Gamma\left(\frac{7}{3}\right) - \Gamma^2\left(\frac{5}{3}\right)\right]\right]. \tag{5.21}$$

The PDF of the extrusion time t^* can be found, therefore, upon integrating

over Δt:

$$\begin{aligned} p(t^*) =& \int_{-\infty}^{\infty} \mathrm{d}\Delta t \, f(t^*|\Delta t)\mathcal{N}(0, \delta_{\Delta t}^2) \\ =& \mathcal{N}\left[t_0 + \Gamma\left(\frac{5}{3}\right)\left(\frac{3}{2k_\lambda}\right)^{\frac{2}{3}}, \left(\frac{3}{2k_\lambda}\right)^{\frac{4}{3}}\left[\Gamma\left(\frac{7}{3}\right) - \Gamma^2\left(\frac{5}{3}\right)\right] + \delta_{\Delta t}^2 \right]. \end{aligned} \tag{5.22}$$

As demonstrated by Fig. 5.4b, the analytical results are in good agreement with those obtained from the numerical simulations.

Since cell division occurs uniformly in the P-zone, the PDF associated with observing an extrusion at time t and position x is given by:

$$\begin{aligned} f(x, t|\Delta t) =& \frac{f(t|\Delta t)}{L^*} \\ =& \frac{\lambda(t, \Delta t)}{L^*} e^{-\int_0^t \lambda(t', \Delta t)\mathrm{d}t'}, \end{aligned} \tag{5.23}$$

for $-L^*/2 < x < L^*/2$. From Eqs. 5.15 and 5.16, $\lambda/L^* = g/[(l_d - l_m)(l_a + d_0)]$. Substituting this in Eq. 5.23 gives

$$\begin{aligned} f(x, t|\Delta t) =& \frac{g}{(l_d - l_m)(l_a + d_0)} e^{-\int_0^t \lambda(t', \Delta t)\mathrm{d}t'} \\ =& \frac{g}{(l_d - l_m)(l_a + d_0)} e^{-\frac{2}{3}k_\lambda (t - t_0 - \Delta t)^{3/2}} \end{aligned} \tag{5.24}$$

Thus, the conditional PDF associated with observing an extrusion at position x, given the offset Δt, is:

$$\begin{aligned} f(x|\Delta t) =& \int_{t_p(x)+\Delta t}^{\infty} \mathrm{d}t \, f(x, t|\Delta t) \\ =& \int_{t_p(x)}^{\infty} \mathrm{d}t' \, f(x, t'|0) \\ =& f(x|0), \end{aligned} \tag{5.25}$$

where we have used the transformation $t' = t - \Delta t$ and by virtue of Eq. 5.17, $f(t, |\Delta t)$ depends on t and Δt only via the combination $t - \Delta t$. Here, $t_p(x)$ is the average time at which position x first enters the P-zone. From Eq. 5.25, $f(x|\Delta t)$ is independent of Δt. The PDF associated with observ-

ing the first extrusion at position $|x^*|$ is then:

$$\begin{aligned} p(|x^*|) &= 2\int_{t_p(x^*)}^{\infty} \mathrm{d}t\, f(x,t|0) \\ &= \frac{2g}{(l_d-l_m)(l_a+d_0)} \int_{t_p(x^*)}^{\infty} \mathrm{d}t\, e^{-\frac{2}{3}k_\lambda (t-t_0)^{3/2}} \\ &= \frac{2g}{(l_d-l_m)(l_a+d_0)} \left(\frac{2}{3}\right)^{\frac{1}{3}} k_\lambda^{-\frac{2}{3}} \Gamma\left[\frac{2}{3}, \frac{2}{3}k_\lambda \left(t_p(x^*)-t_0\right)^{\frac{3}{2}}\right], \end{aligned} \tag{5.26}$$

where $\Gamma[s,x]$ is the incomplete Gamma function. It can be demonstrated that $[t_p(x)-t_0]^{1/2} = k_x x$, where $k_x = 2/(bN_0\sqrt{2\omega})$. Substitute this in Eq. 5.26, we have

$$\begin{aligned} p(|x^*|) &= \frac{2g}{(l_d-l_m)(l_a+d_0)} \left(\frac{2}{3}\right)^{\frac{1}{3}} k_\lambda^{-\frac{2}{3}} \Gamma\left[\frac{2}{3}, \frac{2}{3}k_\lambda k_x^3 x^{*3}\right] \\ &= \left(\frac{2}{3}k_\lambda k_x^3\right)^{\frac{1}{3}} \Gamma\left[\frac{2}{3}, \frac{2}{3}k_\lambda k_x^3 x^{*3}\right], \end{aligned} \tag{5.27}$$

which again agrees well with the simulations (Fig. 5.4a).

Finally, let us go back to the original disk-like colonies. In a disk-like colony, the emergence of nematic domains makes the stress anisotropic,

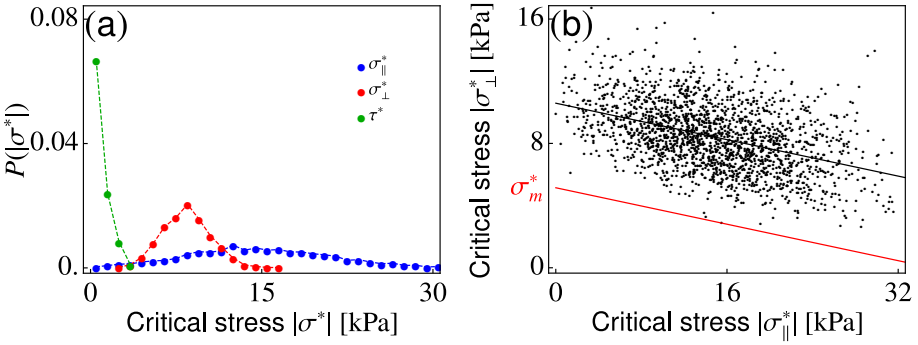

Figure 5.7. Critical stress in a disk-like colony at the "control" parameters. (a) The probability distributions of different components of the critical stress. (b) The two normal components of the critical stress $\sigma_\parallel^*$ and $\sigma_\perp^*$ are anti-correlated (i.e. $\sigma_\perp^* \sim -\sigma_\parallel^*$) and fall above a line of minimal critical stress σ_m^* (in red). The black line shows a linear fit to the data points: $|\sigma_\perp^*| \sim -c|\sigma_\parallel^*|$.

as discussed in chapter 3. The in-plane stress tensor can, nevertheless, be decomposed into longitudinal and transverse components, namely:

$$\boldsymbol{\sigma}_i = \sigma_{i\parallel}\boldsymbol{p}_i^{\parallel}\boldsymbol{p}_i^{\parallel} + \sigma_{i\perp}\boldsymbol{p}_i^{\perp}\boldsymbol{p}_i^{\perp} + \tau_i(\boldsymbol{p}_i^{\parallel}\boldsymbol{p}_i^{\perp} + \boldsymbol{p}_i^{\perp}\boldsymbol{p}_i^{\parallel}) \ , \tag{5.28}$$

where $\boldsymbol{p}_i^{\parallel} = [p_{ix}, p_{iy}]$ and $\boldsymbol{p}_i^{\perp} = [-p_{iy}, p_{ix}]$. To encode the anisotropy of the stress tensor in the transition, we measure the critical stresses of the extruded cells, and extract the three components, whose probability densities are shown in Fig. 5.7a. The shear component τ^* is always negligible, whereas both normal stresses affect the stability of the planar configuration. Specifically, plotting $\sigma_{\parallel}^*$ against $\sigma_{\perp}^*$, we find that the two critical normal stresses are linearly related to each other (Fig. 5.7b), namely: $\sigma_{\perp}^* \sim -c\sigma_{\parallel}^*$, with c a positive constant. In addition, all data points fall above a line with the same slope (red line in Fig. 5.7b). These results indicate that in a planar colony the two normal stresses are working together to extrude cells. In addition, a $\sigma_{\perp}$ can trigger the transition as easily as a $\sigma_{\parallel} = \sigma_{\perp}/c$, and the fact that $c < 1$ means that the amount of contributions from the two normal stresses to the instability of cells are different. The cause for this correlation is still unknown, and requires further investigations of mechanical interactions in the full 3D scenario, which is beyond the scope of this thesis. Nevertheless, based on the results shown in Fig. 5.7, we can define an effective stress $\sigma = \sigma_{\perp} + c\sigma_{\parallel}$ for each cell, as well as a minimal effective critical stress σ_m^* as indicated in Fig. 5.7b. Whenever $\sigma > \sigma_m^*$, a cell division can always trigger a mono-to-multilayer transition. Figures 5.4d-e show the probability distributions of the extrusion position, the extrusion time, and the effective critical stress $\sigma^* \equiv \sigma_{\perp}^* + c\sigma_{\parallel}^*$ for the original disk-like colonies (e.g. Fig. 5.1). Despite the mechanical interactions being more complex in disk-like colonies, the physical picture emerging from the simulations is nearly identical to that discussed for chain-like colonies.

5.4 Discussion and conclusion

The enormous variety of physical and biochemical mechanisms observed in cellular systems defeats the notion of universality, despite this, biofilms and tissues feature traits that are consistently found across several morphotypes and species, such as the capability of transitioning from simple monolayers to more complex multilayered structures [56, 65, 66, 110, 111,

116, 13]. Whereas this transition manifests itself in a multitude of possible variants, depending upon the nature of the environmental and intercellular forces, it robustly relies on a limited number of fundamental principles, which most cellular systems have in common. First, the interplay between steric interactions and active motion or growth, drives the formation of coherent structures on the plane, such as nematic domains [122], topological defects [13] or large groups of collectively moving cells [30]. Second, the extensile stresses arising from the in-plane spatial organization and the lack of vertical confinement, drives the cellular layer to be unstable to extrusion. Because intercellular forces are mainly repulsive, this process occurs at the scale of individual cells, in spite of the collective origin of the in-plane stresses driving the instability. Third, the transition is both deterministic and stochastic. For a given configuration of the colony, there is well defined critical stress, related with the cells *local* arrangment (e.g. cell length and nematic order). But, as this is inherently random, so is the critical stress and, consequently, the extrusion time and position. Therefore, there is no uniquely defined critical state, but rather an ensemble of them. Upon modeling cell division as a Poisson process, and under the assumption that newly divided cells are the first to be extruded, we were able to reconstruct the probability distribution of the extrusion time and position for a simple laterally-confined chain-like colony, finding excellent agreement with our numerical data. The rate λ of the Poisson process is analogous to the order parameter in phase transitions and, as the transition depends on the details of the system uniquely via λ, we expect our result to be generic and carry over to other systems, as long as λ can be derived or approximated.

Chapter 6

Conclusion and outlook

Bacteria, being one of the most common organisms on earth, were first observed by the Dutch microscopist Antonie van Leeuwenhoek in 1676. Since then, they have been intensively studied from perspectives of biochemistry, biology, and ecology. It is only until recent years, that the role of physics, and especially mechanics, has started to draw attention. The work presented in this thesis is an attempt to describe bacterial organization from physical principles and highlight the mechanical and geometrical aspects of colonization.

We use a minimal model system, in which non-motile, rod-shaped bacteria, sandwiched between a glass slide and an agarose gel, push each other away as they grow in length. It is astonishing that such a simple system can exhibit a myriad of complex emergent behaviors, including the chaotic dynamics of nematic micro-domains in a freely expanding colony, the global alignment of cells upon confinement, and the stochastic transition from a monolayer to a multilayered structure in large colonies. These emerging phenomena can ultimately be ascribed to the complex interplay among cell orientation, cell growth, and mechanical stresses. First of all, cell growth provides a continuous feed of stress along the cell axis. Second, steric repulsion between elongated cells drives them to align with each other, and any distortion from the aligned configurations will cause elastic torques which tend to restore perfect alignment. Third, anisotropic stresses can directly reorient cells and force them to align along the direction of minimal stress. In addition, the gradient of stresses can also drive motion of cells, which, in turn, alter the cells orientation. Such a reorientation changes not only the direction of cell growth, hence the stress feed into the rest of the colony, but also redistributes the local stress among the longitudinal and transverse components, with respect to the average orientation of a cell cluster. This intricate interplay between orientational dynamics and stress relaxation can, ultimately, give rise to a plethora of complex mechanical behaviors.

In a freely expanding colony, the growth-induced stress is released

isotropically by the radially expanding flow, resulting in an extensile active stress. That is, the stress is extensile along the local nematic director and contractile in the orthogonal direction. Such an active stress bends the nematic director at the expenses of the orientational elastic energy. This competition between active disordering and passive restoring stresses, results into the formation of nematic domains which, as the colony evolves, merge, buckle and break apart in a complex sequence of morphological and topological transformation. In a confined colony, however, the stress is released anisotropically, hence is globally anisotropic: the stress components in the confined direction are on average larger than their orthogonal counterparts. The globally anisotropic stress can drive cells to align with its minimal principal axis (i.e. the unconfined direction) and, consequently, the colony shows a global alignment.

For large enough colony, the accumulated lateral stress is large enough to compete with the vertical restoring forces from the agarose on top, and can trigger a transition from a monolayer to a multilayered structure. Although the general picture of this transition is similar to the buckling transition of a flat plate, the underlying physical nature is by no means the same. Specifically, the critical state of the transition is locally defined, and depends on the local cell length. Accordingly, there is no unique critical state, but an ensemble of critical states, depending upon the distribution of cell length across the colony. Therefore, despite the internal stress following a rather predictable parabolic profile, the position and time at which the transition happens are both random, and can only be predicted statistically.

It cannot be stressed enough that a simple system of growing bacteria can exhibit so many interesting properties: *anisotropy* (i.e. cell orientation and mechanical stress), *inhomogeneity* (spatial-temporal variation of stress), *heterogeneity* (i.e. differential cell length), *stochasticity* (i.e. cell division and mono-to-multilayer transition), and *activity* (i.e. cell growth and division). These properties, commonly shared by living systems, altogether, define the complexity displayed in growing bacterial colonies, and make it extremely difficult to put forward a universal theory that captures all aspects of the bacterial organization. Yet, upon narrowing down the search to specific questions (e.g. how is the area of bacterial domains distributed? What drives the transition form mono- to multi-layered colonies? etc.) and addressing them within the powerful frameworks of continuum and statistical mechanics, it is possible not only

to shed light of the physical mechanisms underpinning these phenomena, but also formulate predictions that are amenable for exprimental scrutiny. What's more, the distinctive properties of living systems, particularly the cell activity such as growth, motility and cell-cell communications, can potentially promote new physics that are not as perceptible in nonliving systems. The challenge remains to make quantitative comparison between the theory and the experiment.

Bibliography

[1] E. Schrödinger, *What is Life? the Physical Aspect of the Living Cell & Mind and Matter* (University P., 1967).

[2] E. Shakhnovich, "Protein folding thermodynamics and dynamics: Where physics, chemistry, and biology meet," Chemical Reviews **106**, 1559–1588 (2006).

[3] R. Phillips, J. Kondev, and J. Theriot, *Physical Biology of the Cell*, 2nd ed. (Garland Science, 2009).

[4] Y.-C. Fung, *Biomechanics: Mechanical Properties of Living Tissues*, 2nd ed., [] (Springer New York, 1993) p. nil.

[5] D. Boal, *Mechanics of the cell*, 2nd ed. (Cambridge University Press, 2012).

[6] T. Vicsek and A. Zafeiris, "Collective motion," Physics Reports **517**, 71–140 (2012).

[7] M. C. Marchetti, J. F. Joanny, S. Ramaswamy, T. B. Liverpool, J. Prost, M. Rao, and R. A. Simha, "Hydrodynamics of soft active matter," Reviews of Modern Physics **85**, 1143–1189 (2013).

[8] J. Toner and Y. Tu, "Long-range order in a two-dimensional dynamicalxymodel: How birds fly together," Physical Review Letters **75**, 4326–4329 (1995).

[9] T. Vicsek, A. Czirók, E. Ben-Jacob, I. Cohen, and O. Shochet, "Novel type of phase transition in a system of self-driven particles," Physical Review Letters **75**, 1226–1229 (1995).

[10] J. D. WATSON and F. H. C. CRICK, "Molecular structure of nucleic acids: A structure for deoxyribose nucleic acid," Nature **171**, 737–738 (1953).

[11] Y. Cheng, N. Grigorieff, P. A. Penczek, and T. Walz, "A primer to single-particle cryo-electron microscopy," Cell **161**, 438–449 (2015).

[12] H. H. Wensink, J. Dunkel, S. Heidenreich, K. Drescher, R. E. Goldstein, H. Lowen, and J. M. Yeomans, "Meso-scale turbulence in living fluids," Proceedings of the National Academy of Sciences **109**, 14308–14313 (2012).

[13] T. B. Saw, A. Doostmohammadi, V. Nier, L. Kocgozlu, S. Thampi, Y. Toyama, P. Marcq, C. T. Lim, J. M. Yeomans, and B. Ladoux, "Topological defects in epithelia govern cell death and extrusion," Nature **544**, 212–216 (2017).

[14] P. Lecca, ed., *Biomechanics of Cells and Tissues*, Lecture Notes in Computational Vision and Biomechanics (Springer Netherlands, 2013) p. nil.

[15] E. Moeendarbary and A. R. Harris, "Cell mechanics: Principles, practices, and prospects," Wiley Interdisciplinary Reviews: Systems Biology and Medicine **6**, 371–388 (2014).

[16] J. DUMAIS, "Can mechanics control pattern formation in plants?" Current Opinion in Plant Biology **10**, 58–62 (2007).

[17] C. J. Miller and L. A. Davidson, "The interplay between cell signalling and mechanics in developmental processes," Nature Reviews Genetics **14**, 733–744 (2013).

[18] C.-P. Heisenberg and Y. Bellaïche, "Forces in tissue morphogenesis and patterning," Cell **153**, 948–962 (2013).

[19] S. Ramaswamy, "The mechanics and statistics of active matter," Annual Review of Condensed Matter Physics **1**, 323–345 (2010).

[20] M. Amar, A. Goriely, M. Müller, and L. Cugliandolo, *New Trends in the Physics and Mechanics of Biological Systems: Lecture Notes of the Les Houches Summer School: Volume 92, July 2009*, Lecture Notes of the Les Houches Summer School (OUP Oxford, 2011).

[21] W. W. Ahmed, É. Fodor, and T. Betz, "Active cell mechanics: Measurement and theory," Biochimica et Biophysica Acta (BBA) - Molecular Cell Research **1853**, 3083–3094 (2015).

[22] D. Needleman and Z. Dogic, "Active matter at the interface between materials science and cell biology," Nature Reviews Materials **2**, 17048 (2017).

[23] T. B. Saw, W. Xi, B. Ladoux, and C. T. Lim, "Biological tissues as active nematic liquid crystals," Advanced Materials **30**, 1802579 (2018).

[24] A. J. Engler, S. Sen, H. L. Sweeney, and D. E. Discher, "Matrix elasticity directs stem cell lineage specification," Cell **126**, 677–689 (2006).

[25] M. Chiquet, "Regulation of extracellular matrix gene expression by mechanical stress," Matrix Biology **18**, 417–426 (1999).

[26] H. M. López, J. Gachelin, C. Douarche, H. Auradou, and E. Clément, "Turning bacteria suspensions into superfluids," Physical Review Letters **115**, 028301 (2015).

[27] J. Dunkel, S. Heidenreich, K. Drescher, H. H. Wensink, M. Bär, and R. E. Goldstein, "Fluid dynamics of bacterial turbulence," Physical Review Letters **110**, 228102 (2013).

[28] A. Kaiser, A. Peshkov, A. Sokolov, B. ten Hagen, H. Löwen, and I. S. Aranson, "Transport powered by bacterial turbulence," Physical Review Letters **112**, 158101 (2014).

[29] L. Giomi, "Geometry and topology of turbulence in active nematics," Physical Review X **5**, 031003 (2015).

[30] C. Blanch-Mercader, V. Yashunsky, S. Garcia, G. Duclos, L. Giomi, and P. Silberzan, "Turbulent dynamics of epithelial cell cultures," Physical Review Letters **120**, 208101 (2018).

[31] D. Bi, X. Yang, M. C. Marchetti, and M. L. Manning, "Motility-driven glass and jamming transitions in biological tissues," Physical Review X **6**, 021011 (2016).

[32] A. Mongera, P. Rowghanian, H. J. Gustafson, E. Shelton, D. A. Kealhofer, E. K. Carn, F. Serwane, A. A. Lucio, J. Giammona, and O. Campàs, "A fluid-to-solid jamming transition underlies vertebrate body axis elongation," Nature **561**, 401–405 (2018).

[33] J. Ranft, M. Basan, J. Elgeti, J.-F. Joanny, J. Prost, and F. Julicher, "Fluidization of tissues by cell division and apoptosis," Proceedings of the National Academy of Sciences **107**, 20863–20868 (2010).

[34] T. Speck, "Collective behavior of active brownian particles: From microscopic clustering to macroscopic phase separation," The European Physical Journal Special Topics **225**, 2287–2299 (2016).

[35] M. E. Cates and J. Tailleur, "Motility-induced phase separation," Annual Review of Condensed Matter Physics **6**, 219–244 (2015).

[36] J. Stenhammar, A. Tiribocchi, R. J. Allen, D. Marenduzzo, and M. E. Cates, "Continuum theory of phase separation kinetics for active brownian particles," Physical Review Letters **111**, 145702 (2013).

[37] C. M. Waters and B. L. Bassler, "Quorum sensing: Cell-to-cell communication in bacteria," Annual Review of Cell and Developmental Biology **21**, 319–346 (2005).

[38] D. Volfson, S. Cookson, J. Hasty, and L. S. Tsimring, "Biomechanical ordering of dense cell populations," Proceedings of the National Academy of Sciences **105**, 15346–15351 (2008).

[39] Y. Hatwalne, S. Ramaswamy, M. Rao, and R. A. Simha, "Rheology of active-particle suspensions," Physical Review Letters **92**, 118101 (2004).

[40] T. B. Liverpool and M. C. Marchetti, "Hydrodynamics and rheology of active polar filaments," in *Cell Motility* (Springer New York, New York, NY, 2008) pp. 177–206.

[41] A. W. C. Lau and T. C. Lubensky, "Fluctuating hydrodynamics and microrheology of a dilute suspension of swimming bacteria," Physical Review E **80**, 011917 (2009).

[42] R. Blackwell, O. Sweezy-Schindler, C. Baldwin, L. E. Hough, M. A. Glaser, and M. D. Betterton, "Microscopic origins of anisotropic active stress in motor-driven nematic liquid crystals," Soft Matter **12**, 2676–2687 (2016).

[43] H. Vlamakis, Y. Chai, P. Beauregard, R. Losick, and R. Kolter, "Sticking together: Building a biofilm the bacillus subtilis way," Nature Reviews Microbiology **11**, 157–168 (2013).

[44] P. Watnick and R. Kolter, "Biofilm, city of microbes," Journal of Bacteriology **182**, 2675–2679 (2000).

[45] G. O'Toole, H. B. Kaplan, and R. Kolter, "Biofilm formation as microbial development," Annual Review of Microbiology **54**, 49–79 (2000).

[46] T.-F. C. Mah and G. A. O'Toole, "Mechanisms of biofilm resistance to antimicrobial agents," Trends in Microbiology **9**, 34–39 (2001).

[47] D. McDougald, S. A. Rice, N. Barraud, P. D. Steinberg, and S. Kjelleberg, "Should we stay or should we go: Mechanisms and ecological consequences for biofilm dispersal," Nature Reviews Microbiology **10**, 39–50 (2011).

[48] B. Rosan and R. J. Lamont, "Dental plaque formation," Microbes and Infection **2**, 1599–1607 (2000).

[49] J. Kaplan, "Biofilm dispersal: Mechanisms, clinical implications, and potential therapeutic uses," Journal of Dental Research **89**, 205–218 (2010).

[50] J. W. Costerton, "Bacterial biofilms: A common cause of persistent infections," Science **284**, 1318–1322 (1999).

[51] H. Cho, H. Jönsson, K. Campbell, P. Melke, J. W. Williams, B. Jedynak, A. M. Stevens, A. Groisman, and A. Levchenko, "Self-organization in high-density bacterial colonies: Efficient crowd control," PLoS Biology **5**, e302 (2007).

[52] D. M. Morris and G. J. Jensen, "Toward a biomechanical understanding of whole bacterial cells," Annual Review of Biochemistry **77**, 583–613 (2008).

[53] T. J. Rudge, F. Federici, P. J. Steiner, A. Kan, and J. Haseloff, "Cell polarity-driven instability generates self-organized, fractal patterning of cell layers," ACS Synthetic Biology **2**, 705–714 (2013).

[54] A. Persat, C. D. Nadell, M. K. Kim, F. Ingremeau, A. Siryaporn, K. Drescher, N. S. Wingreen, B. L. Bassler, Z. Gitai, and H. A. Stone, "The mechanical world of bacteria," Cell **161**, 988–997 (2015).

[55] J. Sheats, B. Sclavi, M. C. Lagomarsino, P. Cicuta, and K. D. Dorfman, "Role of growth rate on the orientational alignment of

escherichia coli in a slit," Royal Society Open Science **4**, 170463 (2017).

[56] M. A. A. Grant, B. W. aw, R. J. Allen, and P. Cicuta, "The role of mechanical forces in the planar-to-bulk transition in growing escherichia coli microcolonies," Journal of The Royal Society Interface **11**, 20140400–20140400 (2014).

[57] J. W. Costerton, Z. Lewandowski, D. E. Caldwell, D. R. Korber, and H. M. Lappin-Scott, "Microbial biofilms," Annual Review of Microbiology **49**, 711–745 (1995).

[58] B. D. Hoffman, C. Grashoff, and M. A. Schwartz, "Dynamic molecular processes mediate cellular mechanotransduction," Nature **475**, 316–323 (2011).

[59] D. Boyer, W. Mather, O. Mondragón-Palomino, S. Orozco-Fuentes, T. Danino, J. Hasty, and L. S. Tsimring, "Buckling instability in ordered bacterial colonies," Physical Biology **8**, 026008 (2011).

[60] S. Orozco-Fuentes and D. Boyer, "Order, intermittency, and pressure fluctuations in a system of proliferating rods," Physical Review E **88**, 012715 (2013).

[61] P.-T. Su, C.-T. Liao, J.-R. Roan, S.-H. Wang, A. Chiou, and W.-J. Syu, "Bacterial colony from two-dimensional division to three-dimensional development," PLoS ONE **7**, e48098 (2012).

[62] F. D. C. Farrell, O. Hallatschek, D. Marenduzzo, and B. Waclaw, "Mechanically driven growth of quasi-two-dimensional microbial colonies," Physical Review Letters **111**, 168101 (2013).

[63] A. Doostmohammadi, S. P. Thampi, and J. M. Yeomans, "Defect-mediated morphologies in growing cell colonies," Physical Review Letters **117**, 048102 (2016).

[64] H. Wioland, E. Lushi, and R. E. Goldstein, "Directed collective motion of bacteria under channel confinement," New Journal of Physics **18**, 075002 (2016).

[65] M.-C. Duvernoy, T. Mora, M. Ardré, V. Croquette, D. Bensimon, C. Quilliet, J.-M. Ghigo, M. Balland, C. Beloin, S. Lecuyer,

and N. Desprat, "Asymmetric adhesion of rod-shaped bacteria controls microcolony morphogenesis," Nature Communications **9**, 1120 (2018).

[66] F. Beroz, J. Yan, Y. Meir, B. Sabass, H. A. Stone, B. L. Bassler, and N. S. Wingreen, "Verticalization of bacterial biofilms," Nature Physics **14**, 954–960 (2018).

[67] J. Yan, A. G. Sharo, H. A. Stone, N. S. Wingreen, and B. L. Bassler, "Vibrio choleraebiofilm growth program and architecture revealed by single-cell live imaging," Proceedings of the National Academy of Sciences **113**, E5337–E5343 (2016).

[68] R. Hartmann, P. K. Singh, P. Pearce, R. Mok, B. Song, F. Díaz-Pascual, J. Dunkel, and K. Drescher, "Emergence of three-dimensional order and structure in growing biofilms," Nature Physics **nil**, nil (2018).

[69] F. D. Farrell, M. Gralka, O. Hallatschek, and B. Waclaw, "Mechanical interactions in bacterial colonies and the surfing probability of beneficial mutations," Journal of The Royal Society Interface **14**, 20170073 (2017).

[70] E. J. Stewart, R. Madden, G. Paul, and F. Taddei, "Aging and death in an organism that reproduces by morphologically symmetric division," PLoS Biology **3**, e45 (2005).

[71] B. I. Shraiman, "Mechanical feedback as a possible regulator of tissue growth," Proceedings of the National Academy of Sciences **102**, 3318–3323 (2005).

[72] F. Montel, M. Delarue, J. Elgeti, L. Malaquin, M. Basan, T. Risler, B. Cabane, D. Vignjevic, J. Prost, G. Cappello, and J.-F. Joanny, "Stress clamp experiments on multicellular tumor spheroids," Physical Review Letters **107**, 188102 (2011).

[73] P. Kumar and A. Libchaber, "Pressure and temperature dependence of growth and morphology of escherichia coli: Experiments and stochastic model," Biophysical Journal **105**, 783–793 (2013).

[74] L. Giomi, N. Hawley-Weld, and L. Mahadevan, "Swarming, swirling and stasis in sequestered bristle-bots," Proceedings of the Royal

Society A: Mathematical, Physical and Engineering Sciences **469**, 20120637–20120637 (2013).

[75] A. Doostmohammadi, J. Ignés-Mullol, J. M. Yeomans, and F. Sagués, "Active nematics," Nature Communications **9**, 3246 (2018).

[76] P. G. D. Gennes and J. Prost, *The physics of liquid crystal*, 2nd ed. (Clarendon Press, Oxford, 1993).

[77] L. D. Landau and E. M. Lifshitz, *Theory of elasticity*, 2nd ed. (Pergamon Press, Oxford, 1969).

[78] L. Giomi, L. Mahadevan, B. Chakraborty, and M. F. Hagan, "Banding, excitability and chaos in active nematic suspensions," Nonlinearity **25**, 2245–2269 (2012).

[79] L. A. Archer and R. G. Larson, "A molecular theory of flow alignment and tumbling in sheared nematic liquid crystals," The Journal of Chemical Physics **103**, 3108–3111 (1995).

[80] A. Ahmadi, T. B. Liverpool, and M. C. Marchetti, "Nematic and polar order in active filament solutions," Physical Review E **72**, 060901 (2005).

[81] A. Ahmadi, M. C. Marchetti, and T. B. Liverpool, "Hydrodynamics of isotropic and liquid crystalline active polymer solutions," Physical Review E **74**, 061913 (2006).

[82] L. Giomi, M. J. Bowick, X. Ma, and M. C. Marchetti, "Defect annihilation and proliferation in active nematics," Physical Review Letters **110**, 228101 (2013).

[83] L. Giomi, M. J. Bowick, P. Mishra, R. Sknepnek, and M. C. Marchetti, "Defect dynamics in active nematics," Philosophical Transactions of the Royal Society A: Mathematical, Physical and Engineering Sciences **372**, 20130365–20130365 (2014).

[84] S. P. Thampi, R. Golestanian, and J. M. Yeomans, "Velocity correlations in an active nematic," Physical Review Letters **111**, 118101 (2013).

[85] A. Doostmohammadi, M. F. Adamer, S. P. Thampi, and J. M. Yeomans, "Stabilization of active matter by flow-vortex lattices and defect ordering," Nature Communications **7**, 10557 (2016).

[86] A. Doostmohammadi, T. N. Shendruk, K. Thijssen, and J. M. Yeomans, "Onset of meso-scale turbulence in active nematics," Nature Communications **8**, 15326 (2017).

[87] A. Doostmohammadi, S. P. Thampi, T. B. Saw, C. T. Lim, B. Ladoux, and J. M. Yeomans, "Celebrating soft matter's 10th anniversary: Cell division: a source of active stress in cellular monolayers," Soft Matter **11**, 7328–7336 (2015).

[88] Y. Sumino, K. H. Nagai, Y. Shitaka, D. Tanaka, K. Yoshikawa, H. Chaté, and K. Oiwa, "Large-scale vortex lattice emerging from collectively moving microtubules," Nature **483**, 448–452 (2012).

[89] T. Sanchez, D. T. N. Chen, S. J. DeCamp, M. Heymann, and Z. Dogic, "Spontaneous motion in hierarchically assembled active matter," Nature **491**, 431–434 (2012).

[90] S. J. DeCamp, G. S. Redner, A. Baskaran, M. F. Hagan, and Z. Dogic, "Orientational order of motile defects in active nematics," Nature Materials **14**, 1110–1115 (2015).

[91] P. Guillamat, J. Ignés-Mullol, and F. Sagués, "Control of active liquid crystals with a magnetic field," Proceedings of the National Academy of Sciences **113**, 5498–5502 (2016).

[92] P. M. Chaikin and T. C. Lubensky, *Principles of condensed matter physics*, 1st ed. (Cambridge University Press, New York, 1995).

[93] M. J. Bowick, L. Giomi, H. Shin, and C. K. Thomas, "Bubble-raft model for a paraboloidal crystal," Physical Review E **77**, 021602 (2008).

[94] T. J. Pedley and J. O. Kessler, "Hydrodynamic phenomena in suspensions of swimming microorganisms," Annual Review of Fluid Mechanics **24**, 313–358 (1992).

[95] R. Voituriez, J. F. Joanny, and J. Prost, "Spontaneous flow transition in active polar gels," Europhysics Letters (EPL) **70**, 404–410 (2005).

[96] D. Marenduzzo, E. Orlandini, M. E. Cates, and J. M. Yeomans, "Steady-state hydrodynamic instabilities of active liquid crystals: Hybrid lattice boltzmann simulations," Physical Review E **76**, 031921 (2007).

[97] S. A. Edwards and J. M. Yeomans, "Spontaneous flow states in active nematics: A unified picture," EPL (Europhysics Letters) **85**, 18008 (2009).

[98] L. Giomi, L. Mahadevan, B. Chakraborty, and M. F. Hagan, "Excitable patterns in active nematics," Physical Review Letters **106**, 218101 (2011).

[99] J. Ockendon, S. Howison, A. Lacey, and A. Movchan, *Applied Partial Differential Equations*, Oxford Applied and Engineering Mathematics Series (Oxford University Press, 1999).

[100] K. P. Koutsoumanis and A. Lianou, "Stochasticity in colonial growth dynamics of individual bacterial cells," Applied and Environmental Microbiology **79**, 2294–2301 (2013).

[101] W. P. J. Smith, Y. Davit, J. M. Osborne, W. Kim, K. R. Foster, and J. M. Pitt-Francis, "Cell morphology drives spatial patterning in microbial communities," Proceedings of the National Academy of Sciences **114**, E280–E286 (2016).

[102] G. Duclos, C. Erlenkämper, J.-F. Joanny, and P. Silberzan, "Topological defects in confined populations of spindle-shaped cells," Nature Physics **13**, 58–62 (2016).

[103] B. Karamched, W. Ott, I. Timofeyev, R. Alnahhas, M. Bennett, and K. Josić, "Moran model of spatial alignment in microbial colonies," Physica D: Nonlinear Phenomena **395**, 1–6 (2019).

[104] G. Duclos, S. Garcia, H. G. Yevick, and P. Silberzan, "Perfect nematic order in confined monolayers of spindle-shaped cells," Soft Matter **10**, 2346–2353 (2014).

[105] S. R. Broadbent and J. M. Hammersley, "Percolation processes," Mathematical Proceedings of the Cambridge Philosophical Society **53**, 629 (1957).

[106] T. Marschall and S. Teitel, "Compression-driven jamming of athermal frictionless spherocylinders in two dimensions," Physical Review E **97**, 012905 (2018).

[107] S. Chen, P. Gao, and T. Gao, "Dynamics and structure of an apolar active suspension in an annulus," Journal of Fluid Mechanics **835**, 393–405 (2017).

[108] G. Duclos, C. Blanch-Mercader, V. Yashunsky, G. Salbreux, J.-F. Joanny, J. Prost, and P. Silberzan, "Spontaneous shear flow in confined cellular nematics," Nature Physics **14**, 728–732 (2018).

[109] A. Opathalage, M. M. Norton, M. P. N. Juniper, B. Langeslay, S. A. Aghvami, S. Fraden, and Z. Dogic, "Self-organized dynamics and the transition to turbulence of confined active nematics," Proceedings of the National Academy of Sciences **116**, 4788–4797 (2019).

[110] E. Marinari, A. Mehonic, S. Curran, J. Gale, T. Duke, and B. Baum, "Live-cell delamination counterbalances epithelial growth to limit tissue overcrowding," Nature **484**, 542–545 (2012).

[111] R. Fernandez-Gonzalez and J. A. Zallen, "Feeling the squeeze: Live-cell extrusion limits cell density in epithelia," Cell **149**, 965–967 (2012).

[112] G. T. Eisenhoffer, P. D. Loftus, M. Yoshigi, H. Otsuna, C.-B. Chien, P. A. Morcos, and J. Rosenblatt, "Crowding induces live cell extrusion to maintain homeostatic cell numbers in epithelia," Nature **484**, 546–549 (2012).

[113] G. T. Eisenhoffer and J. Rosenblatt, "Bringing balance by force: Live cell extrusion controls epithelial cell numbers," Trends in Cell Biology **23**, 185–192 (2013).

[114] C. Guillot and T. Lecuit, "Mechanics of epithelial tissue homeostasis and morphogenesis," Science **340**, 1185–1189 (2013).

[115] G. M. Slattum and J. Rosenblatt, "Tumour cell invasion: an emerging role for basal epithelial cell extrusion," Nature Reviews Cancer **14**, 495–501 (2014).

[116] L. Kocgozlu, T. B. Saw, A. P. Le, I. Yow, M. Shagirov, E. Wong, R.-M. Mège, C. T. Lim, Y. Toyama, and B. Ladoux, "Epithelial cell packing induces distinct modes of cell extrusions," Current Biology **26**, 2942–2950 (2016).

[117] A. Ambrosini, M. Gracia, A. Proag, M. Rayer, B. Monier, and M. Suzanne, "Apoptotic forces in tissue morphogenesis," Mechanisms of Development **144**, 33–42 (2017).

[118] S. Ohsawa, J. Vaughen, and T. Igaki, "Cell extrusion: A stress-responsive force for good or evil in epithelial homeostasis," Developmental Cell **44**, 284–296 (2018).

[119] M. J. Alava, P. K. V. V. Nukala, and S. Zapperi, "Statistical models of fracture," Advances in Physics **55**, 349–476 (2006).

[120] J. Kingman, *Poisson Processes*, Oxford Studies in Probability (Clarendon Press, 1992).

[121] A. Papoulis, *Probability, random variables, and stochastic processes*, 4th ed., McGraw-Hill series in systems science (McGraw-Hill, 2002).

[122] Z. You, D. J. G. Pearce, A. Sengupta, and L. Giomi, "Geometry and mechanics of microdomains in growing bacterial colonies," Physical Review X **8**, 031065 (2018).

Samenvatting

Bacteriën, één van de meest voorkomende organismen op aarde, zijn in 1676 voor het eerst waargenomen door de Nederlandse wetenschapper Antonie van Leeuwenhoek. Ze zijn sindsdien intensief bestudeerd vanuit biochemisch, biologisch en ecologisch perspectief. Pas sinds enkele jaren bekijken wetenschappers bacteriën ook vanuit een natuurkundig, en dan vooral mechanisch, perspectief. In dit proefschrift zetten we een eerste stap naar het begrijpen van de zelforganisatie van groeiende bacteriën, waarbij we laten zien welke biofysische mechanismen de vorming van koloniën aandrijven.

We gebruiken een simpel model van niet-bewegende, staafvormige bacteriën, ingeklemd tussen een glasplaat en een agarose-gel, die elkaar wegduwen wanneer ze in de lengte groeien. Dit simpele systeem toont, afhankelijk van de omstandigheden, verschillende manieren van zelforganisatie: chaotische dynamica van nematische microdomeinen in een onbegrensd groeiende kolonie, of een globale ordening van cellen in een begrensde ruimte, of een stochastische transitie van een enkele laag bacteriën tot een meerlagige structuur in grote koloniën. Deze emergente verschijnselen zijn het gevolg van de complexe wisselwerking tussen cel-oriëntatie, celgroei en mechanische spanning. Ten eerste zorgt celgroei voor een voortdurende opbouw van spanning langs de as van de cel. Ten tweede gaan langwerpige cellen parallel aan elkaar liggen onder invloed van sterische interacties. Afwijkingen van deze parallelle configuratie worden gecorrigeerd door een oriëntationele elastische spanning. Ten derde, mechanische spanning kan cellen direct draaien richting hun minimale as en celbewegingen veroorzaken, die op hun beurt ook tot celdraaiing leiden. Omgekeerd zorgt de draaiing van cellen voor veranderingen in de richting van celgroei en daardoor in de richting van spanningsopbouw. Al deze mechanismen kunnen, individueel of samen, leiden tot verschillende vormen van koloniegroei.

In een onbegrensd groeiende kolonie relaxeert de mechanische spanning isotroop door de naar buiten gerichte stroming, resulterend in een oprekbare vervorming-genererende spanning: de spanning is extensief langs de lokale nematische director en contractief in de richting loodrecht daarop, zoals de extensieve, actieve spanning in actieve nematische materialen. Deze extensieve, actieve spanning buigt de nematische director. De com-

petitie tussen de oriëntationele elastische spanning en de vervormingsgenererende spanning zorgt dan voor de vorming van nematische domeinen en chaotische dynamica in het systeem. In een begrensde kolonie relaxeert de spanning echter anisotroop en is daardoor globaal anisotroop: de componenten van de spanning in de begrensde richting zijn gemiddeld groter dan de componenten loodrecht daarop. De globale anisotrope spanning zorgt ervoor dat cellen parallel aan de onbegrensde richting gaan liggen en heeft als gevolg dat de kolonie globaal geordend is.

Voor koloniën die groot genoeg zijn, is de opgebouwde laterale spanning voldoende sterk om de competitie aan te gaan met de verticale krachten van de bovenliggende agarose-gel; dit leidt tot een transitie van een enkele laag bacteriën tot een meerlagige structuur. Hoewel deze transitie lijkt op de kniktransitie van een vlakke plaat, is het onderliggende fysische mechanisme absoluut niet hetzelfde. Om precies te zijn is de kritische toestand van de transitie lokaal gedefinieerd en afhankelijk van de lokale cellengte. Daarnaast is er geen unieke kritische toestand maar een hele verzameling kritische toestanden, met een specifieke combinatie van cellengte en kritische spanning. Bovendien maakt de willekeurige celgroei het onmogelijk om de cellengte op een specifieke plaats te bepalen. Daardoor zijn zowel de locatie als het moment waarop de transitie gebeurt willekeurig, en kunnen ze alleen statistisch voorspeld worden, ondanks het feit dat de interne spanning een duidelijk parabolisch profiel heeft.

Het is opvallend dat dit eenvoudige model van groeiende bacteriën zoveel interessante eigenschappen heeft: *anisotropie* (van celorientatie en mechanische spanning), *inhomogeniteit* (van spanning in zowel ruimte als tijd), *heterogeniteit* (van differentiële cellengte), *stochasticiteit* (van celdeling en transitie van één tot meerdere lagen), en *activiteit* (van celgroei en celdeling). Deze eigenschappen definiëren de complexiteit van groeiende bacteriekoloniën en maken het zeer moeilijk om met een universele theorie te komen die alle aspecten van de koloniën beschrijft. De natuurkunde is daarom, door de voorkeur voor simpliciteit en sterke connectie met de wiskunde, uitermate geschikt om zelforganisatie in groeiende bacteriekoloniën te bestuderen. Onder andere continuümmechanica en statistische mechanica zijn handig voor het beschrijven van de dynamica van cellulaire systemen, omdat ze niet alleen intuïtie over de dynamica verschaffen maar ook kwantitatieve voorspellingen kunnen doen. In dit proefschrift hebben we de continuümtheorie van actieve nematische materialen gebruikt om de geometrie en mechanica van microdomeinen te begrijpen, en statisti-

sche theorie om de plaats en tijd van de transitie van één naar meerdere lagen te voorspellen. Bovendien kunnen de bijzondere eigenschappen van levende systemen, zoals celgroei, celbeweging en cel-celcommunicatie, leiden tot nieuwe natuurkunde die niet voorkomt in niet-levende systemen. Het blijft hierbij een uitdaging om de theorie kwantitatief met experimenten te vergelijken.

Curriculum Vitæ

I was born in 1989 in Fujian, a province in Southeast China. It was in this beautiful province that I received my early education, including primary, middle, and high schools. After that, I went to Beijing for my undergraduate studies, at Beijing University of Posts and Telecommunications, where I was trained, for the first time, as a physicist. My academic life continued at Beijing Normal University as a Master student in theoretical physics. In 2015, I was enrolled as a PhD candidate at the Lorentz Institute, Leiden University. Under the supervision of Dr. Luca Giomi, I studied theoretically the growth of bacterial colonies, endeavouring to understand the self-organization from the perspective of a physicist. In the nearest future, I will continue my exploration in soft&bio-mechanics as a postdoc at the University of California at Santa Barbara, USA.

List of Publications

1. *Characteristics and applications of two-dimensional light scattering by cylindrical tubes based on ray tracing*, Z. You, D. Jiang, Z. Hou, and J. Xiao, Am. J. Phys. 80(8), 688-693 (2012).

2. *Analysis of light scattered by a capillary to measure a liquid's index of refraction*, Z. You, D. Jiang, J. Stamnes, J. Chen, and J. Xiao, Appl. Opt. 51(35), 8341-8349 (2012).

3. *Multiple beam interference model for measuring parameters of a capillary*, Q. Xu, W. Tian, Z. You, and J. Xiao, Appl. Opt. 54(22) 6948-6954 (2015).

4. *Geometry and mechanics of microdomains in growing bacterial colonies*, Z. You, D.J.G. Pearce, A. Sengupta, and L. Giomi, Phys. Rev. X 8(3), 031065 (2018).
   Chapters 2&3

5. *Statistical properties of autonomous flows in 2D active nematics*, L.M. Lemma, S.J. Decamp, Z. You, L. Giomi, and Z. Dogic, Soft Matter 15, 3264-3272 (2019).

6. *Mono-to-multilayer transition in growing bacterial colonies*, Z. You, D.J.G. Pearce, A. Sengupta, and L. Giomi, arXiv:1811.08875, submitted to Phys. Rev. Lett.
   Chapter 5

7. *Confinement-induced self-organization in growing bacterial colonies*, Z. You *et al.* in preparation.
   Chapter 4

Acknowledgments

I would like to express my sincere gratitude to my supervisor Luca Giomi. Not only has he shaped me as a physicist through his guidance, motivation, and training, but he sets a great role model for me with his in-depth perception and immense knowledge. In addition, the patience and care he showed to my life and my career have made everything much easier during these years. I can not imagine having a better advisor and mentor for my PhD study. I would also like to thank Prof. H. Schiessel for being my PhD promotor, and kindly helping me go through all the necessary administrative procedures. Special thanks goes to Greg Stephens at the Vrije Universiteit Amsterdam. Although he might not know me in person, his talk on the 'Eigen-worms' was truly inspiring and has greatly boosted my research in physics.

I would like to thank my collaborator Daniel Pearce, who helped me start up the research at the beginning of my PhD and continuously contributed his wisdom to our research projects. Many thanks to my experimental collaborator Anupam Sengupta, for his knowledge and vision from the experimental perspective. My officemate and groupmate–Koen Schakenraad, definitely deserves a grateful acknowledgment. He has been a great and helpful friend. Aside from his assistance with Dutch documentations, including translating the Dutch summary of this thesis (with Christa Broekhuizen), his explanations of Dutch culture and the Dutch way of thinking have been of great value to me. It's always fun and informative to discuss or, more precisely, chat with him, about science, culture, history, politics, etc.

I would also like to thank the other members of the Giomi group: Ireth, Jeremy, Leo, Linda, Ludwig, Melissa, Niladri, Piermarco, Richard, and Steven. I felt so lucky to be part of this wonderful team. I really enjoyed all the discussions, conferences, and of course meals, we had together. I would like to thank the Doctorate Committee for their comments and feedback to my thesis. I am indebted to the secretaries at the institute–Fran, Manon, and Marianne, as well as to Leonardo for the IT support. Their assistance has made my work much easier. In addition, I would like to thank my friends: Huibin, Qiang, Ke, Yujie, Weichun, Qi, Donggang, Xuxing, Zujia, Jiangnan, Benny, Debu, Hamed, Rongfang, Yuan, and

many others whose names are not listed here.

Finally, there is my family, who are of great support in my work and my life. I am infinitely grateful for the endless caring from my grandmother and the unconditional support from my parents and parents-in-law. Words cannot describe my gratitude to my wife Ruxue for always being there for me, and my daughter Ziyi, for being so precious.